Nina Edvardsdal

Comparisons of Image Quality and Aperture Blockage Caused by the Ribs for Male and Female Patients in Echocardiography

Master's thesis

NTNU
Norwegian University of Science and Technology
Faculty of Information Technology and Electrical Engineering
Department of Circulation and Medical Imaging

NTNU
Norwegian University of
Science and Technology

Nina Edvardsdal

Comparisons of Image Quality and Aperture Blockage Caused by the Ribs for Male and Female Patients in Echocardiography

NTNU

Norwegian University of
Science and Technology

Preface

This paper is the results of a master thesis completed at the Faculty of Information Technology and Electrical Engineering at NTNU during the spring of 2022. The thesis is written at the Department of Circulation and Medical Imaging at NTNU, and it is an extension of the project thesis written in the autumn of 2021 [1]. I would like to thank the department for providing access to ultrasound equipment and patient data, which were central in writing this master thesis. I would also like to thank Jørgen Avdal, Thomas Grønli and Stefano Fiorentini for teaching the ultrasound classes at the department. These classes have helped me understand the ultrasound field on a deeper level.

I would like to especially thank my supervisor Svein-Erik Måsøy for great explanations and discussions throughout the duration of this thesis. I would also like to thank Ole Marius Hoel Rindal for providing useful code, as well as helping me understand the USTB.

Norwegian University of Science and Technology

Trondheim, June 2022

Nina Edvardsdal

Abstract

In echocardiograms, the ribs can degrade the image quality by blocking parts of the aperture. Patients with narrower intercostal spaces are therefore more difficult to image [2]. A sonographic analysis of the intercostal spaces revealed that women have significantly narrower intercostal spaces than men [3]. It has, however, not been tested if women have more aperture blockage and poorer image quality than men because of the probe size and the differences in rib cage dimensions. There is also currently no standard quantitative measure for image quality in echocardiograms. The metrics already used, like contrast measures and coherence methods, have weaknesses that limit their use for in-vivo image quality.

This paper aims to compare different levels of ultrasound energy for men and women for the purposes of finding out if the cardiac probes are too large for women's intercostal spaces due to aperture blockage by the ribs. A method for visualizing the blockage will be introduced as a tool for cardiologist, and the resulting plots will be compared to echocardiograms of real patients. This method will also be used to demonstrate a new type of aperture blockage. In addition to this, a new image quality metric called the Global Image Coherence (GIC) will be tested. This metric does not have the drawback that it requires identification of one or more ROI, meaning that it can be optimal for measuring in-vivo image quality.

The method for visualizing the blockage is based on using MATLAB to construct amplitude plots of the reflected energy to the probe for three different energy levels. These levels were set to range from 0 to -9 dB. The data set under scrutiny contained 291 recordings of five image views from 37 men and 19 women. The GIC and the percentage of the energy levels were calculated for each of the 64 frames for all the recordings. In addition, the data set was also divided into taller patients ($\geq$ 170-178 cm) and patients with a BMI above and below 25 to see if there were any significant differences.

The results revealed that the male patients and the taller patients had significantly higher GIC values. This means that patients with wider intercostal spaces had better image quality as the GIC metric proved to be suitable for measuring in-vivo image quality. It was also revealed that the apical views had significantly higher GIC than the parasternal view, most likely due to interference with the lungs. A weakness with how the method calculated and visualized the energy levels was that it only detected loss of signal energy, and not the cases where the ribs are interfering with the ultrasonic signal before it gets reflected to the probe.

As a conclusion, patients with wider intercostal spaces had better image quality. This indicates that the probes used today might be too large for women and shorter people. It was, however, not possible to conclude that this was because of aperture blockage by the ribs as the amplitude plots only detected blockage that caused signal loss. The results therefore argue the need to conduct a larger study where other cases of rib interference are considered.

Table of Contents

List of Figures

List of Tables

1 Introduction

Cardiovascular diseases (CVDs), which are a class of diseases involving the heart and the blood vessels, are currently the leading cause of death on a global basis [4]. The World Health Organization (WHO) estimates that about 17.9 million people died from CVDs in 2019, representing 32% off all global deaths. The increase in obesity, which is one of the main risk factors associated with CVDs, will most likely cause the prevalence of CVDs to grow in the coming years [5]. WHO estimates that the amount of deaths caused by CVDs can be as high as 24.4 million by 2030. It is therefore important to have accurate and effective diagnostic tools to identify these diseases in order to prevent premature deaths. One of the most important non-invasive diagnostic tools is cardiac ultrasound, also known as echocardiography. If the image resolution is adequate, echocardiography can provide helpful information about the heart, like pumping capacity, valve problems and muscle damage [6]. A reduced image quality in echocardiography is therefore problematic as it provides low or non-existing diagnostic value.

There is currently no standard quantitative measure of the image quality in ultrasound cardiac imaging. Assessment of the image quality is generally performed subjectively, by for example visual grading [7]. A major limitation with subjective assessment is that it is based on an impression of quality, meaning that it can vary a lot from cardiologist to cardiologist. An objective measure of quality could remove these subjective variations, leading to more stable results. Image quality measurements will also make the scanner more user-friendly if it gives feedback on the quality to the user. This is a major advantage as smaller and more complex ultrasound systems will be used in more places. In addition, a quantitative measure could also possibly maximize the diagnostic value by allowing an automatic selection of the recording with the highest image quality. Based on this, it is evident that there is a need in the ultrasound field for a metric that objectively measure the quality of the ultrasound images.

In addition to subjective assessments, the image quality has conventionally been evaluated by measuring the contrast ratio (CR), contrast-to-noise ratio (CNR), and the generalized contrast-to-noise ratio (gCNR) [8]. Contrast and CNR compare speckle statistics between a hyperechoic target and surrounding tissue to distinguish differences between neighbouring tissue regions [9]. Even though both contrast and CNR have shown to strongly correlate with qualitative assessments by human observers, they suffer from some major drawbacks. One limitation, which the gCNR is immune to, is that the metrics can be manipulated by alterations to the dynamic range [8]. All three metrics are, however, limited for the in-vivo usability because they require identification of two regions of differing. These regions are especially challenging to identify in-vivo, and also means that the metric provide relative, rather than absolute, measure of image quality.

Another way to measure the image quality is to measure the spatial coherence, or similarity, of the received signals in the ultrasound system. A metric called the Coherence Factor (CF) was

first introduced by Mallart and Fink in 1992 [10]. This metric evaluates the focusing quality by estimating the ratio of the coherent and incoherent signals across the aperture. Li and Li expanded this in 2003 by generalizing the CF to cover objects with diffuse scatterers [11]. Similarly, Camacho et. al. developed a function called Phase Coherence Factor (PCF) in 2009 which exploits the phase instead of the amplitude [12]. In 2018, a metric called the Lag-One Coherence (LOC) was suggested as an in-vivo measure of image quality by Long et. al. as it only requires one region-of-interest [9]. However, the LOC still requires one region-of-interest to be identified, which means that it is not an optimal solution for in-vivo measurements. This paper will further elaborate on these results by demonstrating a new metric called the Global Image Coherence (GIC). This metric can be calculated from any of the previously coherence measures introduced, and it has the advantage that it does not require any identified region-of-interest. The GIC calculates an average over the coherence values over a defined range gate, which results in a single coherence value per image frame.

There are several things that can affect the image quality in medical ultrasound imaging. It is generally desirable to have a large aperture as it improves the lateral resolution in the images. In echocardiography, however, this is not as simple as large apertures are more susceptible to partial blockage by the ribs [2]. A common problem in echocardiography is therefore having an aperture that is large, but also fits in the patient's intercostal spaces. An article published in Ultrasound in Medicine and Biology introduces five scenarios that lead to different types of degradation of image quality in echocardiograms [2]. Two of these scenarios illustrate how the ribs are blocking the ultrasound beams due to specular reflections for two different beam-to-rib angles. In the first scenario the ultrasound beams are reflected outside the rib cage where they get reverberated by the fat and skin layers. In the second scenario the beams are reflected inside the rib cage where they can be reverberated by the out-of-scan-plane heart tissue or left lung. In both of these scenarios it is assumed that the ultrasound beams are reflected back to the probe. However, it is possible that the beams hitting the ribs are not reflected back to the probe, but rather scattered or reflected in another direction. This can result in a reduction of the signal energy at the transducer, which can cause a degradation in the image quality. Based on these three scenarios, it is safe to conclude that patients with shorter intercostal spaces are more difficult to image as the ultrasound beams do not intersect the heart in the desired view without interfering with the ribs.

Patients scheduled to do an echocardiography have very different bodies, where the amount of fat and muscle, the height and the rib cage dimension are examples that can differ a lot from patient to patient. All of these factors can affect the image quality in different ways. Thick layers of skin, subcutaneous fat and intercostal muscle can cause the energy to be reflected between these interfaces, resulting in reverberation noise [2]. Measurement have also shown that both fat and muscle layers can cause wave shape distortion that cannot completely be corrected by time-shift compensation [13]. Wave shape distortion caused by the ribs and cartilage structures was, however, revealed in an article published by the Acoustical Society of America to be more severe than those

caused by soft tissue [14]. The distortion was most severe for transducers with diameters larger than the intercostal spaces. It is therefore interesting that in today's echocardiograms approximately the same size of the probe is being used on all adult patients [1]. An article published in the American Journal of Roentgenology measured the widths of the intercostal spaces of the right inferior human rib cage, and concluded that the overall variations from person to person were substantial [3]. The measurements revealed that the height had a significant positive correlation with the widths of the intercostal spaces, meaning that these are wider for taller people. It was also concluded that women had significantly narrower intercostal spaces than men at all areas. This would mean that the patients who are more difficult to image are more likely to be women than men. A hypothesis is therefore that the image quality in echocardiograms for women are poorer than for men because of the probe size.

The medical field has discriminated against women multiple times in the past. An article published in The Economist last year put this topic on the agenda by discussing multiple examples where the medical field have discriminated against non-white people and women [15]. A recent example is from a study published in 2019 which found that women were twice as likely to experience complications from implantable cardiac devices within 90 days of implantation [16]. It was also revealed in a study from 2013 that women in the four regions the authors looked at had 29% higher risk of their hip implants failing within the first three years of a hip-replacement [17]. The main problem in both of these cases was that the people making the devices failed to recognize the physical size difference between the male and the female body. It was revealed in an analysis in 2018 that the study population in 15% of NIH studies conducted in 2015 consisted of less than 30% women, where only 26% of the studies conducted subgroup analysis by gender [18]. It is therefore not unimaginable that the cardiac probes were mainly tested on men during the design stage, which could potentially have resulted in a standard cardiac probe that is too large to fit in an average woman's intercostal spaces.

This thesis aims to test the hypothesis that women have poorer image quality and more aperture blockage than men because of the probe size. This will be done by comparing different levels of ultrasonic energy reduction caused by the ribs for a data set consisting of recordings from both male and female patients. The method used to test this hypothesis is based on calculating the reflected energy from a specific range depth to the transducer in MATLAB. The blockage will be visualized by constructing amplitude plots of this energy for three different energy levels. These amplitude plots will be introduced as a tool for the cardiologist to get a better overview over the blocked parts of the aperture. In relation to this, a new case of aperture blockage where the energy is not reflected back to the transducer will be demonstrated. Lastly, this thesis also aims to conclude whether the GIC can be used as an effective and accurate measure of image quality in echocardiography. This will be done by seeing if there is a connection between the amount of aperture blockage, the image quality of the echocardiograms and the resulting GIC values.

2 Theoretical Background

The first part of this chapter is intended to give the unfamiliar reader an introduction to the basic principles behind ultrasound technology used in the medical field. The second part focuses on image quality in ultrasound imaging, while the third part is about echocardiography and how the ribs can interfere with the ultrasound beams. Lastly, the differences in the intercostal spaces for men and women, as well as tall and short people, are explained based on measurements from an article. All the theory presented is relevant to understand the results given in this master thesis.

The identification of the majority of the theory presented in the next sections was carried out in the project preceding this master thesis [1]. This means that parts of the theory, as well as some of the structure of this chapter, are taken from the previously written project report. Some parts have, however, been rewritten.

2.1 Principles of Ultrasound Imaging

Ultrasound waves are longitudinal pressure waves with frequencies between 2 - 15 MHz, which is well above the audible range of 20 Hz - 20 kHz for humans [19]. These waves are transmitted into the human body, where they will interact with different tissue characteristics. It is all the different types of interactions between the waves and the tissues that allow visualization of tissue structures in the human body. The most important interactions are reflection, scattering and absorption [20]. This is the fundamental principle behind ultrasound imaging.

The acoustic impedance is an important quantity in ultrasound technology. This quantity describes how much resistance an ultrasound beam encounters as it passes through the tissue [21]. In equation 1, the impedance is denoted as Z, ρ is the density of the medium and c is the speed of sound.

$$Z = \rho c \tag{1}$$

An ultrasound wave transmitted into the human body will encounter different types of biological tissues with different acoustic impedances [21]. If the acoustic mismatch between two types of tissues is large, almost all the energy in the ultrasound waves will get reflected at the boundary. Local differences in the properties of the tissue medium, like density and compressibility, will also cause scattering of the waves [19]. This, as well as absorption of the energy, means that the returning signal is not as strong as the signal transmitted. An illustration of the concept of pulse-echo ultrasound imaging is depicted in figure 1. The transmitted pulse, Tx, encounters three different tissues with impedances denoted as Z_1, Z_2 and Z_3. The received signal at the transducer is denoted as Rx.
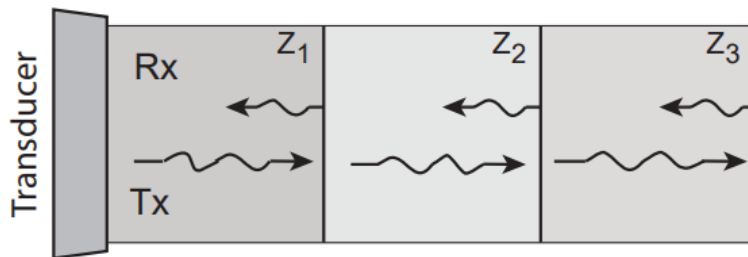
Figure 1: The concept of pulse-echo ultrasound imaging where the transmitted pulse, Tx, encounters different types of tissue with impedances denoted as Z_1, Z_2 and Z_3. The received signal at the transducer is denoted as Rx [19].

2.2   Ultrasound Image Generation

A device known as a transducer is responsible for the transmission and reception of the ultrasound beams [19]. The transducer typically consists of an array of elements made of a piezoelectric crystal. This particular type of crystal has the property that it will expand and contract if a voltage is applied [21]. These movements will result in mechanical vibrations, also known as pressure waves, that will be transmitted into the human body. The returning ultrasound waves will induce electrical signal by deforming the crystals. This means that the elements in a transducer act both as a sensor, receiving mechanical signals, and as an actuator, creating mechanical movement from an electrical signal [22]. There exist different shapes and sizes of transducers designed for specific clinical applications. Transducers also have to be designed to work in specific frequency ranges due to the limited frequency bandwidth of the piezoelectric crystal.

An array of the transducer elements transmits a set of pulses along a specific line known as a scan-line [23]. The returning echoes to the transducer is also received by the same array. An ultrasound image is built by scanning the region of interest in various directions with these scan-lines. Two common scanning modes called the sector scan and the linear scan is illustrated in figure 2. The sector scan uses all the elements for each beam, and transmission delays are used on the array elements so that the beams can be both focused and steered. Because of this, the sector scan is widely used in cardiac applications [19]. The linear scan, however, uses a subset of the aperture for each scan-line, meaning that the active aperture is not constant. This type of scanning produces a rectangular image region, and it is commonly used in vascular and abdominal applications.
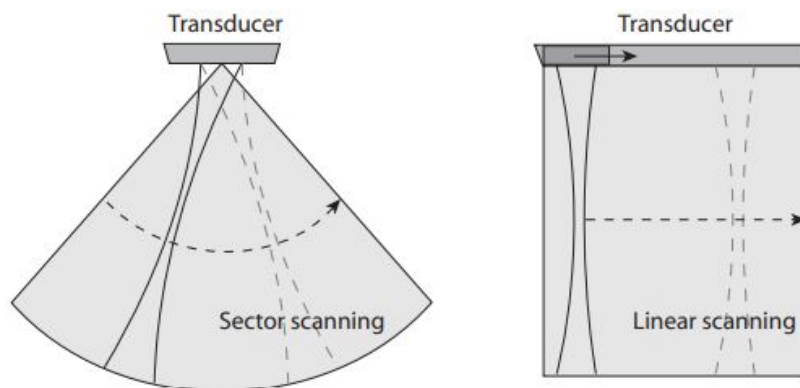
Figure 2: Illustration of the two common ultrasound scanning modes called the sector scan and the linear scan [19].

Focusing is a central beamforming technique used to control the interference pattern from the ultrasound waves [21]. This technique can be applied on both transmit and receive. On transmit, a single focus point can be chosen by applying a set of delays to the pulses emitted from the transducer so that the beam in the region becomes narrower. As a result, constructive interference is obtained as the pulses will arrive at the given point at the same time. One of the main advantages with this is that the reflected signal from this particular area will be very strong, meaning that the resolution is increased. On receive, however, one can apply dynamic receive focusing which is not limited to one fixed focus point per transmission. The delays may be selected individually for each pixel in the image, which allows the focus to be dynamically adjusted to follow the transmitted pulse [24]. This will result in a more uniform focus, and therefore also a more uniform resolution.

The last step conducted when generating an ultrasound image is to visually display the data obtained from the scan-lines [24]. One of the most common and basic display modes today is the B-mode (brightness). A B-mode image is constructed by using several scan-lines to display a two-dimensional cross section of the region of interest. Because the received signal from different tissue structures has a high dynamic range, the signal must be logarithmically compressed in order to display both weak and strong echoes simultaneously [19]. The amplitude of the received signal, also known as the echo strength, is proportional to the brightness of the image points. Figure 3 shows a standard B-mode image of a human heart.

B-mode (brightness mode)

Figure 3: A standard B-mode image of a human heart [19].

2.3   Signal Processing for Ultrasound Images

Signal processing is an essential tool in ultrasound imaging with the main purpose of improving the image quality. This section will introduce and explain some of the most important signal processing techniques used in the medical ultrasound field. The following signal processing techniques were also used in this paper.

2.3.1   Harmonic Filtering

Biological tissue is inhomogenous, meaning that the wave propagation will be nonlinear. Over time, these nonlinearities will cause a distortion of the sinousoidal waveform [21]. The particle velocity, which modulates the acoustic velocity, varies during compression and rarefraction. During the compressional phase, the particle velocity is positive, causing the speed of sound to increase. The opposite happens during the rarefraction phase, meaning that the particle velocity is negative and the speed of sound decreases. As a result, the speed of sound is not constant during the wave cycle. This effect becomes more pronounced with depth, and is illustrated in figure 4. The solid line represents the distorted pulse, while the dotted line is the pulse before distortion.
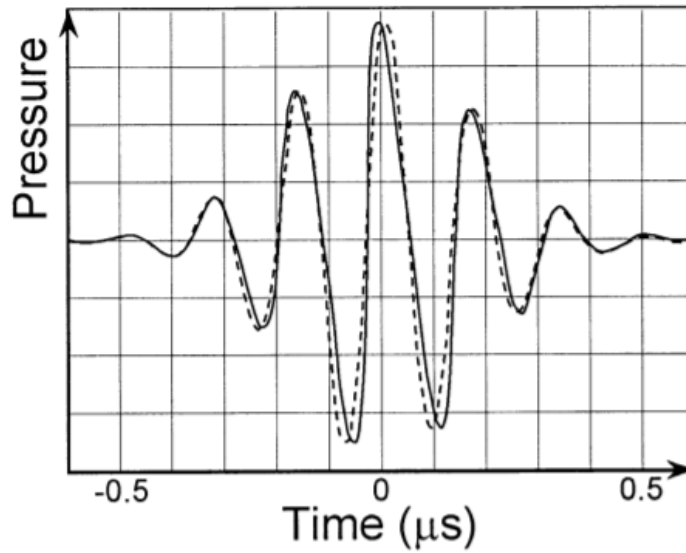
Figure 4: Distortion of the acoustic pulse during propagation within the tissue. The solid line represents the distorted pulse [25].

The change in the waveform will cause a change in the frequency components of the sound wave. If the transducer sends out a band of frequencies centered around the fundamental frequency, f_0, the returned energy will be in two or more frequency bands [25]. These additional frequency bands are called harmonic frequencies, and are multiples of the fundamental frequency. This means that if the fundamental frequency is 2 MHz, the harmonic bands will appear at 4 MHz, 6 MHz, etc. Figure 5 illustrates the harmonic frequencies in the frequency spectrum of the received signal.
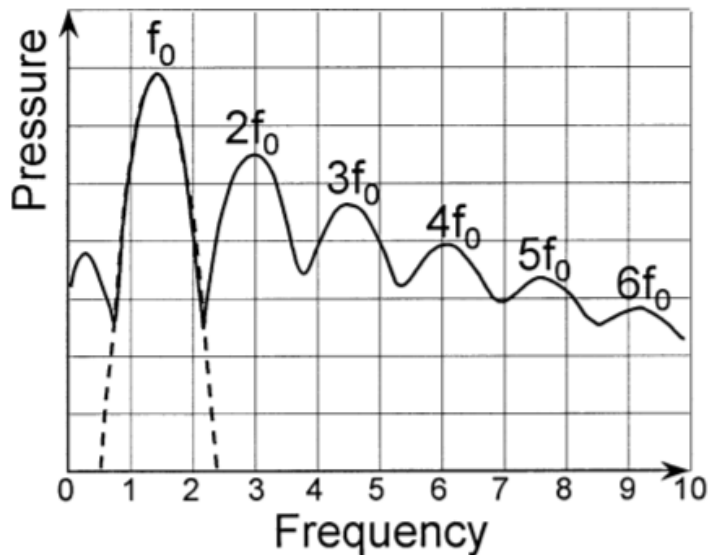
Figure 5: The fundamental frequency band and the harmonic frequency band, where the fundamental frequency is defined as f_0 [25].

A common way to improve the ultrasound image quality is to use harmonic filtering [26]. This is

done by filtering out the fundamental echo signals, and utilizing the harmonics generated by the tissue to form images. The majority of clinical ultrasound system use the second harmonic due to the fact that the returning echoes from higher harmonics are more attenuated. This means that the second harmonic have more signal energy to be used for image formation. The intensity of the second harmonic is, however, 10-20 dB lower than the fundamental, meaning that the filter needs to attenuate an adequate amount of energy in order to obtain a good image quality [21]. Some of the main advantages with harmonic imaging is improved contrast resolution, reduction of reverberation artifacts and improved imaging of deeper tissue. The lateral resolution is also improved because the harmonic waves are predominantly generated at the center of the ultrasound beam, causing the width of the beam to become narrower.

2.3.2   Beamforming

A procedure called beamforming is an essential technique used in ultrasound imaging to produce a focused or steered beam in different depths or directions [24]. This is done by electronically control the array elements in the transducer, and it can be applied on both transmit and receive.

Figure 6 illustrates the delay-and-sum (DAS) beamforming, which is the most common type of receive beamforming. The beams reflected from the red scatterer is arriving at the transducer with a phase shift relative to each other due to the differences in travel distance to the various elements. In order for the beams to arrive in-phase, or coherently, at the elements, time-delays proportional to the distance between the considered region and the elements must be applied. After this is done, an apodization function is usually applied to optimize the image quality [24]. The concept behind apodization is to apply different weights to the signals in order to control the width of the main lobe and reduce the sidelobe levels. Lastly, the signals are summed, resulting in the signal known as the RF-signal [27].
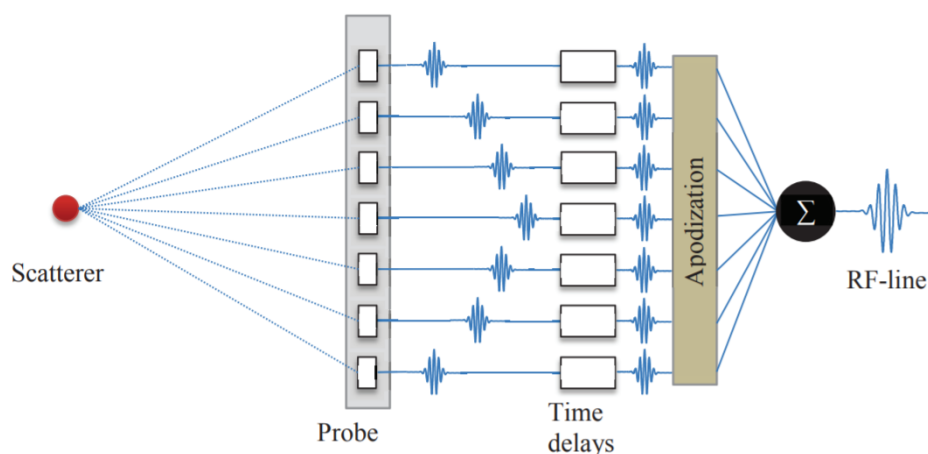
Figure 6: Illustration of the receive beamforming technique called delay-and-sum (DAS) [27].

2.3.3   Scan Conversion

As described in section 2.2, an ultrasound image is built up by scan-lines. The phased array, which is used in cardiac imaging, uses the sector scanning displayed in figure 2. The received data from this scanning is sampled and stored in an array, meaning that the geometric nature of the ultrasound data is lost.

In order to visualize the collected and sampled data in a biological correct way, it is necessary to conduct a coordinate transformation process [28]. This is because the sampling space is in polar coordinates, while the display space is in Cartesian coordinates. The Scan Converter is responsible for this process, and without it, the layout of the imaged object would not make sense.

2.4   Resolution

Resolution is defined as the shortest distance required to discern two closely spaced objects as separate [23]. One of the most important goals in medical ultrasound imaging is to obtain as high resolution as possible, as it makes the diagnostic process more accurate.

The spatial resolution is dependent on the position of the objects of interest relative to the image line. The resolution perpendicular to the beam is called lateral resolution, and the resolution along the image line is called radial resolution. Both the radial and lateral resolution will be explained in detail in this section.

2.4.1   Radial Resolution

The radial resolution is defined as half the spatial pulse length. The pulse length is the product of the number of cycles in the pulse and the wavelength [29]. Since the wavelength is dependent of the frequency, the radial resolution is defined by the transducer. Higher-frequency transducer provides better radial resolution because they provide shorter pulses [23]. A shorter pulse duration means that waves from two closely spaces scatterers are easier to separate. Higher frequencies does, however, limit the penetration of the ultrasound beams. This means that there is a trade-off between the penetration and the radial resolution.

The mathematical expression for the radial resolution is given in equation 2, where $\#N$ is the number of pulse cycles and λ is the wavelength. A small Δz corresponds to a better radial resolution.

$$\Delta z = \frac{1}{2} \cdot \#N \cdot \lambda \tag{2}$$

2.4.2 Lateral Resolution

The lateral resolution is primarily determined by the width of the ultrasound beam [29]. The *-6 dB beam width* is given by equation 3 [23]. A good resolution means that Δx is small.

$$\Delta x = 1.2 \cdot F\# \cdot \lambda \tag{3}$$

In equation 3, $F\#$ is the F-number given by the ratio between the distance to the focus and the dimension of the aperture. To obtain as good lateral resolution as possible, both the F-number and the wavelength should be small [23]. If the F-number is kept constant, then the lateral resolution is constant as well. This means that a bigger part of the aperture should be used when the image depth is increased. The ideal F-number is 1, which means that the width of the aperture is as wide as the focus is deep.

It is also possible to obtain a better lateral resolution by increasing the width of the aperture. This is, however, not straight forward for ultrasound imaging where the acoustic window is limited. An example of this is cardiac imaging where the aperture must fit between the ribs. An aperture blocked, or partially blocked, by the ribs will force the active aperture to become smaller, resulting in poorer lateral resolution. This is one of the main reasons why transducers used in cardiac imaging are smaller than the ones used to image the carotid artery.

2.5 Factors Determining Image Quality in Ultrasound Imaging

There are several factors in medical ultrasound imaging that can limit and degrade the overall image quality. A common problem is the occurrence of artifacts, which are errors that do not represent an actual image of the examined area [30]. Imaging that involves bone tissue are in general more prone to artifacts than imaging involving soft tissue [24]. Artifacts that can occur when bone tissue is imaged are usually due to shadowing, high reverberation levels and specular reflection. Soft tissue, like fat and muscles, limits the image quality through absorption and aberrations, as well as reverberations [31]. The image quality is often degraded due to several of the phenomena previously mentioned because of all the different types of biological tissue the ultrasonic waves propagate through when transmitted into the body.

Both the amplitude and intensity of the ultrasound waves are attenuated as they propagate through tissue [32]. This attenuation is mainly due to adsorptions where ultrasonic energy is converted to heat in the tissue. The attenuation increases with higher frequencies, which means that the frequency limits the penetration depth. Because the transmitted frequency is proportional to the spatial resolution there is a compromise between resolution and penetration [19]. A consequence of this is therefore that imaging of structures deep within the body, like the heart, in general has poorer resolution than structures like the carotid artery. The attenuation in human soft tissue is

approximated to be 0.5 dB/cm MHz one way.

Reverberations are multiple echoes that can lead to different types of acoustic noise in the ultrasound image. A common phenomenon caused by these echoes is a cascade of false surfaces appearing as weakening echoes in the image [33]. Reverberations can occur when the beam encounters two highly reflective interfaces in parallel, and are in this case often caused by reflections between a highly reflective surface in the near-field and the transducer itself. It is also common that reverberations occur due to strong spatial heterogeneity in soft tissue composed of irregular mixtures of muscle, fat and connective tissue [31]. The multiple echoes can also create diffuse echoes, which will appear as a "fog" in the resulting image. These two types of reverberations are one of the most common sources of degradation of image quality, but can be often be avoided by selecting a different imaging plane.

Distortion of an ultrasonic wave, also known as aberration, occurs due to spatial variations in the ultrasound propagation velocity in the different types of tissue in the body [31]. In most ultrasound systems, the time delay applied during beamforming is calculated under the assumption that the sound velocity of the medium is homogeneous [34]. Velocities for tissue in the human body wall is approximately 1448 m/s for fat, 1547 m/s for muscle, and 1613 m/s for skin and connective tissue, which account for the larges sound speed differences in the human body. Aberrations will therefore cause uncertainty in the measured arrival time and decorrelate the waveforms, as well as fluctuations in the energy level [35]. Studies have shown that the wave distortion effects caused by aberrations are dependent on the length and specific morphology of each path [36]. These aberration effects will destroy the focusing of the ultrasound beam and increase the sidelobe levels, which will result in blurring in the obtained image.

Shadowing is an artifact caused by an highly reflective object, such as bone, in the ultrasound beam path [32]. The effect these shadows have on the ultrasound image is dependent on the distance from the probe. A shadow close to the transducer surface will block parts of the transducer, causing the effective aperture to be reduced. A more distant shadow will create a drop out behind the shadowing object. This happens at boundaries where the reflection coefficient is large, which means that transmission is difficult. Almost all the ultrasound pulses will be reflected at the bone, causing fewer pulses to propagate in the area behind the structure.

Specular reflections are a type of reflection that occurs on surfaces that are smooth and large compared to the wavelength [24]. An example of this kind of surface is human bone, like a rib. This phenomenon will cause the ultrasound waves to be reflected in a singular direction. If the transmitted beam is not perpendicular to the specular reflector, the beam will be reflected towards the off-axis direction, resulting in weak echoes. The presence of these strong reflectors can sometimes cause mirroring of objects, meaning that the path of the reflected echoes is longer. The ultrasound system will then place the structure at a deeper location than it actually is located. This can make the physician performing the ultrasound scan to misinterpret the location of an

organ or a structure.

2.6   Echocardiography

Echocardiography is medical ultrasound imaging of the heart [37]. It is an essential, cost-effective and non-invasive diagnostic tool, and has therefore become one of the most widely used diagnostic imaging modalities in cardiology [38]. Echocardiography can provide important information about the size and the shape of the heart, about abnormalities in the heart structures, pumping capacity and overall heart function.

The heart consists of four chambers. These are the upper left and right atrium, and lower left and right ventricle [39]. It is the contraction and relaxation of the different chambers that creates the heartbeat. The right atrium receives blood from the veins and pumps it to the right ventricle, where it gets pumped further to the lungs to get loaded with oxygen. The blood then gets pumped to the left atrium which transports it to the left ventricle. The left ventricle is the strongest chamber in the heart, and is therefore the chamber that pumps the blood to the rest of the body. There are also four valves in the heart that are responsible for the blood flowing the in the correct direction [40]. The mitral valve and the tricuspid valve are located between the atria and the ventricles. The last two valves, the aortic valve and pulmonic vavle, are located between the ventricles and the major blood vessels. Figure 7 shows a simplified illustration of the hearts anatomy.
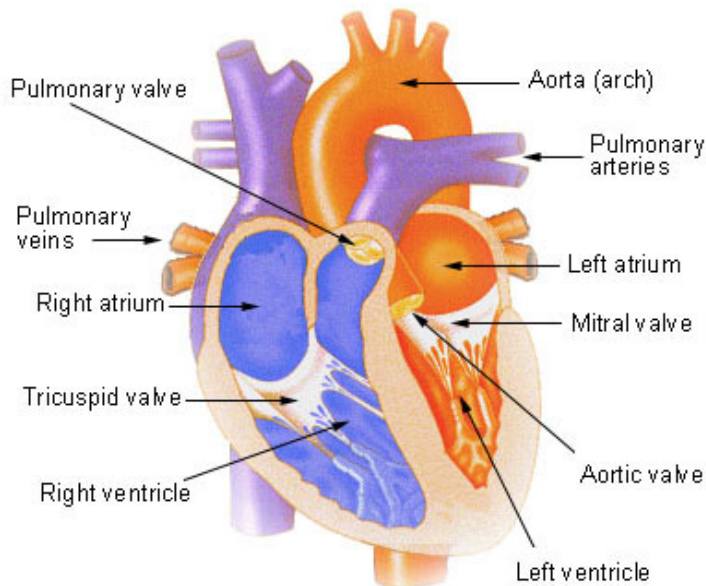
Figure 7: The structure of the hearts anatomy [39].

There are in general two types of echocardiograms called transthoracic echocardiogram (TTE) and transesophageal echocardiography (TEE) [41]. TTE is, unlike TEE, completely non-invasive, and is also by far the most common of the two. All the chambers in the heart, as well as all four vavles,

can be assessed when using TTE [42]. This type of imaging can for example be used to detect heart attacks, weakness of the heart and cardiac tumors. TTE is, however, limited when it comes to assessment of the structures at the back of the heart. TEE can in this case be more accurate than TTE because the ultrasound beams have less tissue to penetrate. The probe is being passed into the patient's esophagus, also know as the "food pipe". TEE is therefore better for patients that are obese, have abnormal chest walls or have thick chests.

The type of echocardiography used in this paper is the TTE. One of the main challenges with this echocardiography is that the heart is partially blocked by the ribs, causing the acoustic window to be limited. Ultrasound beams travelling towards the heart may be reflected out of their intended path if they hit the ribs because of the bones highly reflective surfaces [2]. Whether the energy is reflected inside or outside the rib cage is dependent on the beam-to-rib angle. An article published in Ultrasound in Medicine and Biology specifically illustrates and explains these two cases of reflection at the rib, as well as three other cases that degrade the image quality in TTE [2]. It is assumed in all of these cases that the energy is reflected back to the transducer. The two cases where there is a rib involved in the imaging is illustrated in figure 8. The left, (a), is the case where the energy is reflected outside the rib cage due to specular reflections at the bone. If the energy reach the fat and skin layers it could be reverberated and reflected back to the transducer. This makes the path of the beams longer, causing the ultrasound system to believe that the imaged structure is deeper in the body than it actually is. In addition to this, the reflections will introduce static clutter over the image, causing the overall quality to degrade. This type of reflection is more common for people will a small acoustic window.

The right, (b), shows the second case where the energy is reflected inside the rib cage because of a smaller incident angle [2]. As illustrated in the figure, this energy could reach the tissue that are out of the scan-plane or the lungs. This will result in reverberations that will travel back to the transducer due to specular reflections at the ribs. The effects of this type of reflection will be visible at the top of the ultrasounds image. Reverberations from the lung will be visible with respiration, while the reverberations from the out-of-scan tissue will move with the heart cycle.
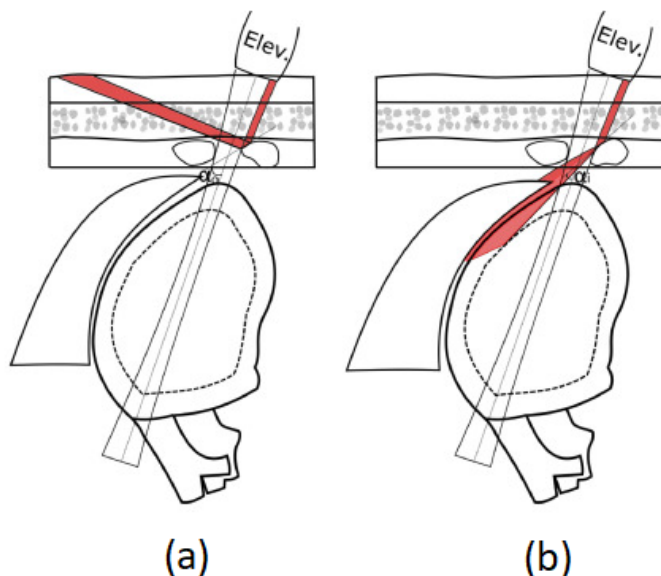
Figure 8: The left figure, (a), show how the beam (red) is partially blocked by the rib causing the energy to be reflected out of the rib cage. The right figure, (b), shows how the beam is reflected out of its intended path inside the rib cage [2].

In addition to the challenges with ribs, there are also some challenges due to the fact that the ultrasound energy has to pass through layers of skin, subcutaneous fat and intercostal muscle before reaching the heart [2]. Three different cases where soft tissue structures interfere with the ultrasound energy are illustrated in figure 9. The left figure, (c), shows possible reflection paths in the soft tissue that can result in reverberations. A thicker the layer of fat and muscles means that more harmonic energy build up, which can make it harder to remove the resulting clutter with harmonic imaging. This means that patients with a higher mass index are more prone to have a higher level of clutter in their cardiac images. The effects of this will can be visible in the whole image, as well as in the near field, where the clutter is relatively static.

The two next cases depicted, (d) and (e), shows how the lung can interfere with the ultrasound energy in both the azimuth and elevation direction, respectively [2]. In case (d), where the heart apex is partially covered by the left lung, the ultrasound energy will encounter air-filled cavities of the lung. These cavities are highly reflective and will therefore result in clutter in one side of the echocardiogram. This kind of clutter will move in and out of the image sector as the patient breathes. For case (e), however, the whole image will be cluttered because the transmit beams partially hit the lung. This clutter will flicker with respiration in the echocardiogram, and is challenging to remove by harmonic imaging.
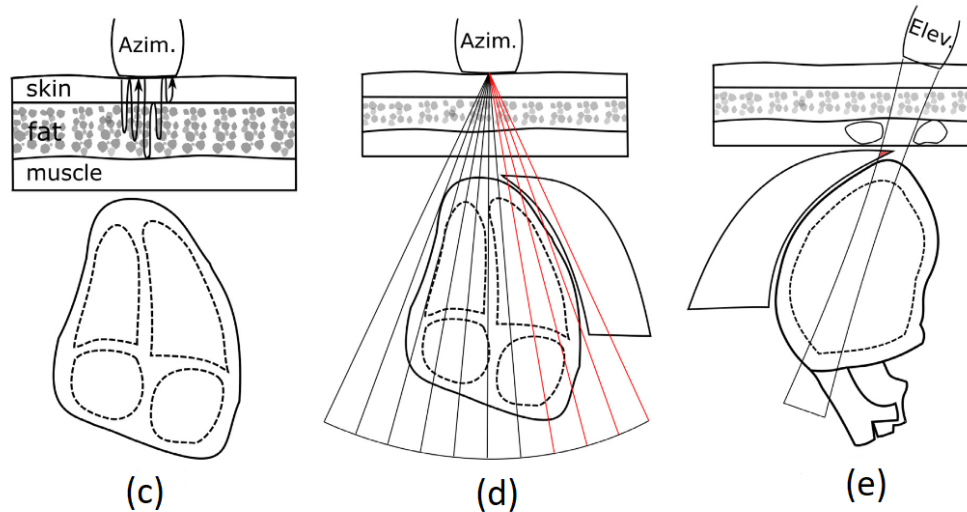
Figure 9: The left figure, (c), shows how the different soft tissue structures can cause the energy to be reverberated. The middle figure, (d), shows how the lung can interfere for patients where the heart apex is partially covered by the left lung. The last figure, (e), shows how the transmit beams can partially hit the lung [2].

The cardiac probe, also called the phased array, is used for cardiac imaging. Because the heart lies deep within the body, and the fact that higher frequencies limits the penetration of the ultrasound beams, the cardiac probes operates on a lower frequency range [23]. This frequency range is usually 2.5-5 MHz in adult echocardiography. The size of these probes are usually small so that they fit in the patient's intercostal spaces and interact with the ribs as little as possible. As mentioned in section 2.4.2, a smaller aperture results in a lower lateral resolution, meaning that some compromises must be made when it comes to the overall image quality. The cardiac probes are, however, able to cover a relatively large region because of the steering of the beams. Figure 10 shows the GE 4Vc-D cardiac probe.

Figure 10: The GE 4Vc-D cardiac probe [43].

During an echocardiography the cardiologist position the probe in different views on the patient's

chest in order to obtain an optimal examination of the heart. These views can be divided into three different planes called long-axis, short-axis and apical [44]. The long-axis plane intersects the major axis of the heart, while the short-axis planes are perpendicular to this axis. An illustration of these scanning planes are shown in figure 11.
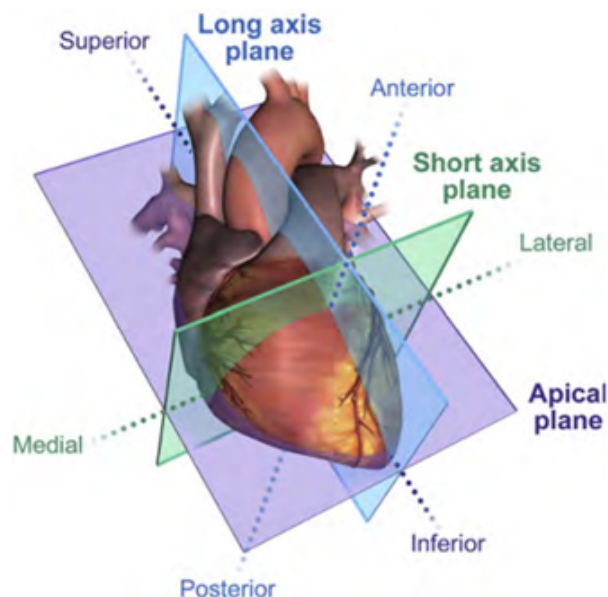
Figure 11: Scanning planes of the heart. The long-axis plane corresponds to images acquired in the PLAX views. The short-axis plane corresponds to images acquired in the PSAX views. The apical plane corresponds to images acquired from the apical window [44].

The different views, also known as windows, are illustrated in figure 12. This paper will focus on the parasternal and some of the apical views.
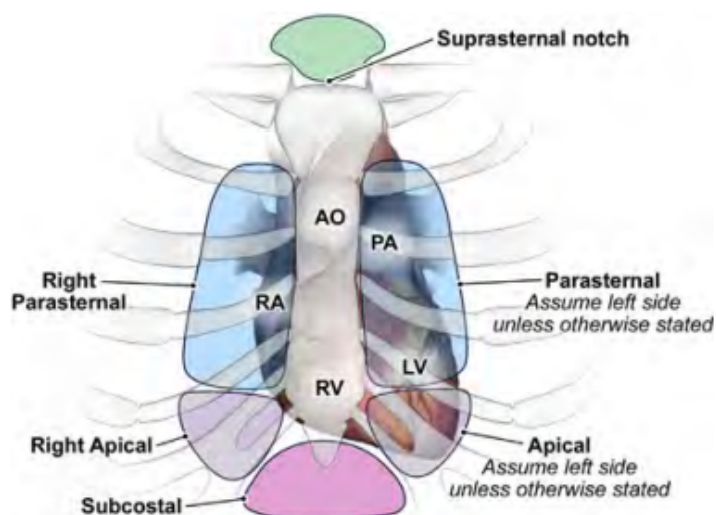
Figure 12: Echocardiographic windows to obtain images [44].

All transducers used in medical ultrasound have an orientation index marker placed on the short

side of the probe [44]. This index marker corresponds to the marker on the side of the ultrasound sector on the monitor. For the parasternal long-axis (PLAX) view this index marker is pointed towards the patient's right shoulder, and the probe is placed in the third and the fourth intercostal space left to the sternum. In this view, it is possible to see the right and left ventricle, the left atrium and the aortic valve. If the probe is rotated clockwise 90 degrees from the PLAX view, the parasternal short-axis (PSAX) view is obtained. The index marker is then pointed towards the patient's left shoulder. Both the right and left ventricle is visible in the PSAX view.

The apical window is located below the left breast tissue, usually in the fifth intercostal space. For the apical four-chamber (A4C) view the index marker is in the 4 to 5 o'clock position. The right and left ventricle, as well as the right and left atrium, is visible in this view. The view of the heart will, however, be upside down and backwards on the ultrasound monitor. If the probe is rotated 60 degrees clockwise from this position, the apical two-chamber (A2C) view is obtained. For the A2C, the left ventricle, the left atrium and the mitral valve is possible to assess. To obtain the apical long-axis (ALAX) view, often referred to as the three-chamber view, the probe must be rotated counterclockwise 60 degrees from the A2C view. This view demonstrates the left atrium, the left ventricle and the mitral and aortic valves.

An article from the American Society of Echocardiography discusses guidelines for performing a transthoracic echocardiography examination [44]. It is here highlighted that the apical views ideally would be available in every patient, but that this is not always the case. The reason for this is due to the fact that ultrasound transmission is limited by the widths of the intercostal spaces. It is also stated that changes in the structure of the thoracic cavity may also limit the access to the apical views. It is therefore safe to conclude that the apical views could be extra challenging to image in some patients.

2.7   Height and Intercostal Space Differences Between Men and Women

Men are psychically bigger and taller than women. According to the latest available data, the global mean height for men and women was 171 cm and 159 cm, respectively [45]. This height disparity between the genders is present everywhere in the world. In Norway the mean height for men was 180 cm and 166 cm for women in 2014 [46]. Figure 13 shows a map where the ratio of male-to-female average heights across the world is illustrated. The map is based on data from 2017. A ratio value above 1 means that the mean height of men is greater than of women. This ratio is 1.07 globally, and has remained almost constant since 1896.

Male-to-female height ratio by year of birth, 1996

Ratio between the mean height of adult men and women, by birth year. Values greater than 1 indicate the mean height of men is greater than that of women.

Our World in Data

| No data | 1.02 | 1.04 | 1.06 | 1.08 | 1.1 | 1.12 | 1.14 |
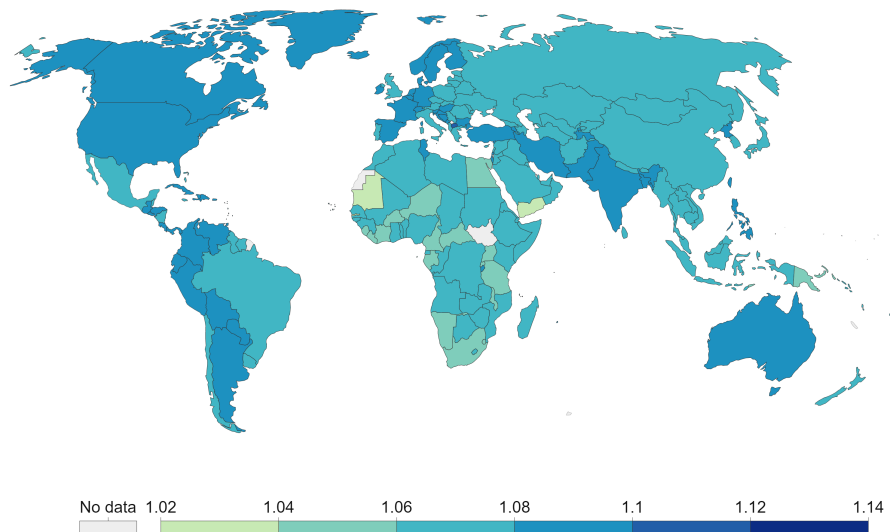
Source: NCD RisC, Human Height (2017)   CC BY

Figure 13: A map showing the ratio of male-to-female average heights across the world, where a ratio greater than 1 indicates that the mean height of men is greater than of women [45].

It has also been confirmed that there is a difference in the rib cage dimensions between the two genders. A study published in the American Journal of Roentgenology measures the widths of the intercostal spaces of the right inferior human rib cage for 214 men and 252 women [3]. It was here concluded that women had significantly narrower intercostal spaces than men. The widths of the individual intercostal spaces had a wide range of 4-33 mm, meaning that there was substantial variations among the patients. It was also revealed that height had a significant positive correlation with the widths of the intercostal spaces ($\rho = 0.126$–0.283), which means that taller people have wider intercostal spaces. Figure 14 shows the mean of the measurements for the different intercostal spaces for both men and women.
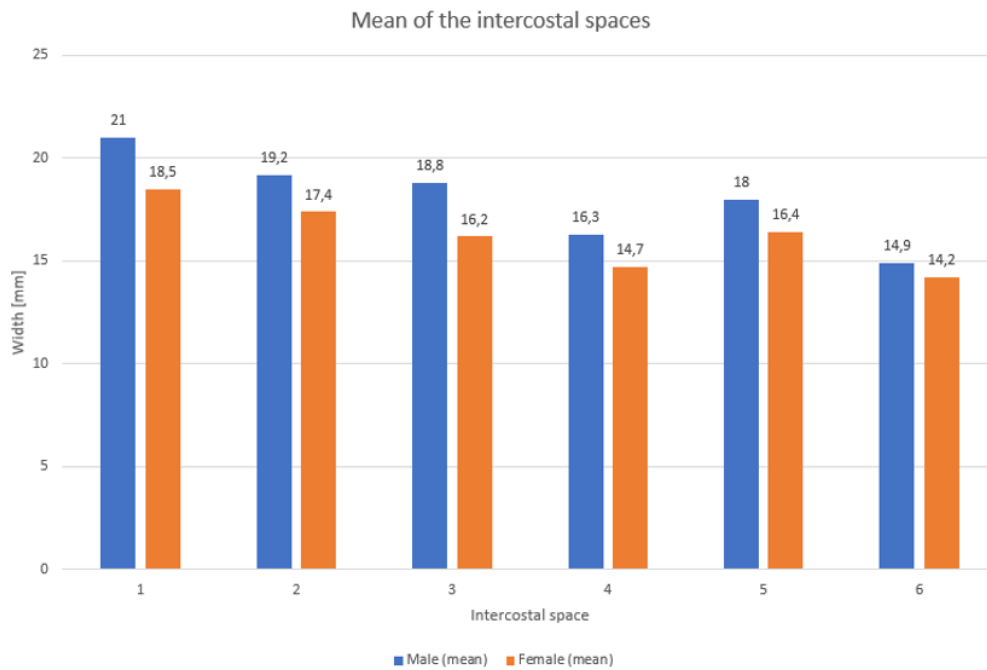
Figure 14: The mean of measurements from 6 intercostal spaces for men and women [3].

The intercostal spaces examined in the article are not exactly the same used to view the heart in cardiac ultrasound imaging. However, based on the fact that all the intercostal spaces measured for men were wider than for women, one can assume that this also applies to the intercostal spaces used when performing a transthoracic echocardiography (TTE). Figure 15 illustrates the areas evaluated of the right inferior rib cage. The dotted lines indicate anterior, mid and posterior axillary lines.
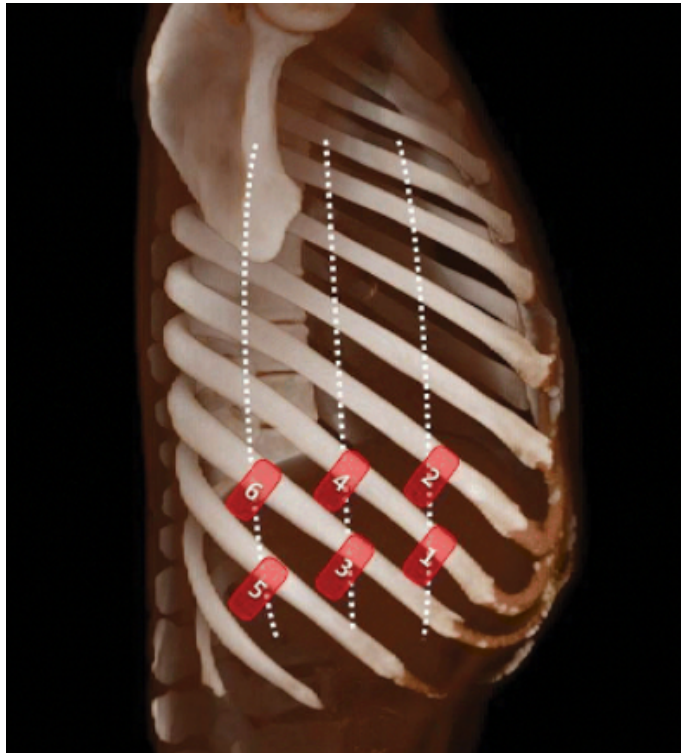
Figure 15: Definitions of areas of the right interior rib cage evaluated. The dotted lines indicate anterior, mid and posterior axillary lines [3].

The measurements were obtained by conducting a sonographic examination, and were validated by CT measurements. The sonographic examinations were performed with one of two sonography machines (Acuson Sequoia 512, Siemens Healthcare; iU-22 xMatrix Ultrasound System, Philips Healthcare) and convex transducers (4C1, Siemens Healthcare; C5-1, Philips Healthcare). These measurements were performed between the most convex points of two adjacent ribs, which is where the acoustic propagation between the ribs was narrowest. The radiologist performing the CT examinations was blinded to the results from the sonographic examinations.

A Wilcoxon signed rank test was conducted to compare the sonographic and CT measurements, and a value of $p < 0.05$ was considered statistically significant. The results revealed that the CT measurements were significantly greater than the sonographic measurements, except in areas 1 and 2. These differences may be due to different physical properties of sonography and CT, and the fact that the sonographic transducer was manually operated.

2.8   Quantitative Metric for Image Quality

The assessment of medical ultrasound image quality can be performed in several ways, both subjectively and objectively. However, there is no common standard for quantitative measurements of the image quality in echocardiograms today [47]. This has resulted in many proposed methods for such measurements in the research community the past few years, where the majority of these

methods are closely related to image quality metrics.

Conventionally, the image quality has been evaluated by measuring the contrast ratio (CR), contrast-to-noise ratio (CNR), and the generalized contrast-to-noise ratio (gCNR) [8]. Even though these metrics have shown to strongly correlate with qualitative assessments by human observers, they suffer from major drawbacks that limit their use in-vivo. They all require identification of two regions of differing, meaning that these metrics provide relative, rather than absolute, measure of image quality [9]. These regions are especially challenging to identify in-vivo, and often require manual interaction.

The focus in this section will be on a metric called the Global Image Coherence (GIC). This metric is based on the coherence, which is a measure of the uniformity of the ultrasonic wave phases. The GIC has the advantage that it does not require any identified regions because it is the accumulation of the simple coherence measure known as the Coherence Factor (CF). Both the principle of coherence and the CF will be explained in the following section in order to understand the GIC.

2.8.1   Coherence

The waves in a wave-field can have different offsets, also known as phase shifts [48]. Coherence is a measure of the uniformity of these phases. If all the waves have random phases, the field is called an incoherent wave field. A coherent wave field contains waves that are in-phase in relation to each other, meaning that the phases are aligned in an orderly fashion.

A transducer in medical ultrasound imaging emits coherent waves into the human body. These waves are, however, scattered and reflected by the different types of tissue before they arrive back at the transducer surface again. This type of wave field can either be scattered coherently or incoherently, where incoherent scattering results in constructive and destructive interference. If the waves are scattered coherently, they will arrive at the transducer simultaneously, meaning that they can be summed with constructive interference. This will result in a stronger signal energy, and therefore also better image quality. Focusing errors, phase aberrations and of-axis scattering are some of the factors that contribute to reduce the degree of coherence [8].

2.8.2   The Coherence Factor

One of the most common ways to calculate the coherence, known as the Coherence Factor (CF), was first introduced by Mallart and Fink in 1994 as the Focusing Criterion [10]. The Coherence Factor is calculated by the ratio between the coherent and incoherent energy across the aperture, as shown in equation 4. This equation gives a metric of CF values for every pixel in the image. The possibility of the signals being summed in-phase is removed by taking the absolute value before

the sum is calculated, meaning that the denominator is the incoherent energy. This means that the nominator is the coherent energy.

$$CF(x,z) = \frac{\left|\sum_{m=1}^{M}\sum_{n=1}^{N} s_{mn}\right|^2}{MN\sum_{m=1}^{M}\sum_{n=1}^{N} |s_{mn}|^2} \tag{4}$$

It is assumed that a 2D-matrix array of M elements in the azimuth direction (along the x-axis) and N elements in the elevation direction (along the y-axis) in a Cartesian coordinate system is used [49]. Focused and steered beams are transmitted in the xz-plane in order to get 2D images, where the z-axis is defined as the depth. The received complex demodulated channel signal (pixel value) on element (m, n) from the point (x, z) on the imaging plane is denoted as given in equation 5.

$$s_{mn} = s(x,z) \tag{5}$$

Figure 16 is a geometrical illustration of the aperture in the xy-plane imaging an arbitrary point (x, z) on the xz-plane [49]. T means transmitted, while R means received.
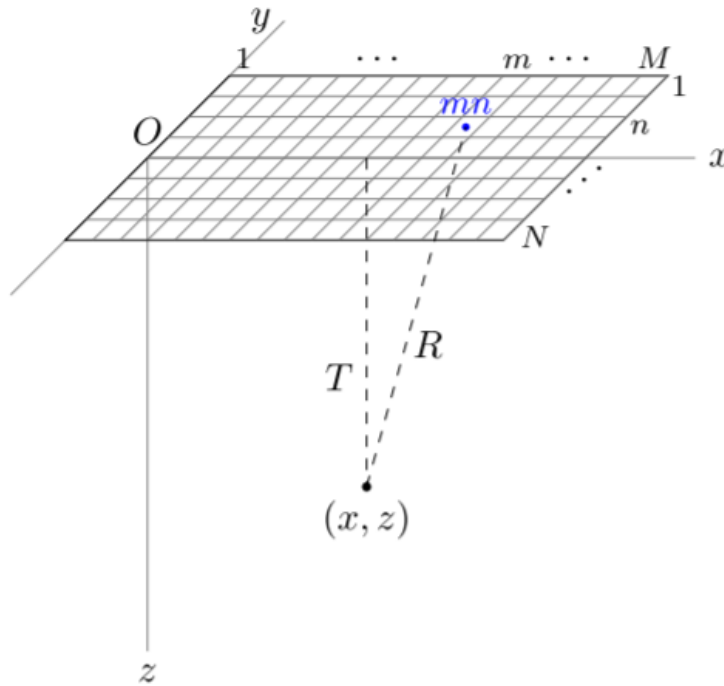
Figure 16: Geometrical illustration of the aperture in the xy-plane imaging an arbitrary point (x, z) on the xz-plane [49].

The Coherence Factor peaks at 2/3 for perfect focusing of multiple scatterers, and at 1 for a single scatterer [50]. This means that a completely incoherent signal has a Coherence Factor of 0. The result is a coherence grid made up of values between 0 and 2/3 for every pixel in the ultrasound image.

2.8.3   The Global Image Coherence

The Global Image Coherence (GIC) is a metric that can be calculated from any coherence method. This metric calculates an average of the pixel coherence values for each frame over a defined range gate, which means that every frame has one value for the GIC. Equation 6 shows an example where the GIC can be calculated from the CF calculated in equation 4.

$$GIC_{CF} = \frac{1}{X(Z_2 - Z_1)} \sum_{x=1}^{X} \sum_{z=Z_1}^{Z_2} CF(x, z) \tag{6}$$

The number of x-pixels in the azimuth direction is denoted as X, while the number of z-pixels in depth is denoted as Z. The range gate is defined as $[Z_1, Z_2]$.

3 Method

The aim of this paper was to calculate and compare the GIC values and three different levels of energy for both men and women, as well as constructing a tool for the cardiologist to view the aperture energy. The data set used contained ultrasound recordings of the heart from 56 patients, and the calculations and visualizations were done in MATLAB (The MathWorks inc, Natick, USA) using the toolbox called USTB. The recordings from the first 22 patients in the data set are the same recordings that were used in the project preceding this master thesis. This chapter explains the different steps in the method used in this paper in detail.

3.1 The Data

The complete data set used contained ultrasound recordings of the heart from 37 male and 19 female patients. All the recordings were obtained at St. Olavs Hospital in Trondheim, but the recordings from the first 22 patients were obtained a few years earlier than the recordings from the last 34 patients. Table 1 shows the information about the first 22 patients in the data set with the patient number, gender and age. The mean age for these patients was 73 years old. These are the same recordings that were used in the project preceding this master thesis [1].

Table 1: The patient number, gender and age for the first part of the complete data set.

Patient	Gender	Age
1	M	78
2	M	72
3	M	59
4	M	70
5	W	84
6	M	54
7	M	71
8	M	78
9	M	78
10	M	74
11	W	76
12	W	77
13	W	84
14	M	86
15	W	67
16	M	84
17	W	70
18	W	70
19	M	65
20	W	69
21	W	72
22	W	63

Table 2 contains the information about the last 34 patients in the data set. The number of male and female patients, as well as the mean age for the genders, are given. The patients' height and BMI were also collected, which was not the case for the first 22 patients.

Table 2: The information about the second part of the complete data set that was obtained a few years later than the first 22 recordings.

	Men	Women	All patients
No. of patients	26	8	34
Mean age	63	64	64
Mean height	181 cm	167 cm	178 cm
Mean BMI	26.7	27.8	27

The data was collected by two experienced cardiologists using an E95 (GE Vingmed Ultrasound

AS, Horten, Norway) ultrasound scanner and a 4Vc-D 2D array probe. The collection of the data is approved by the Regional Committee for Medical and Health Research Ethics (REK). The scanner was set up with second harmonic imaging at a frequency of 3.4 MHz. The transducer has an aperture size of 21.5 mm x 15.6 mm mapped to 10x19 subaperture channels in the azimuth and elevation direction [49].

The total amount of recordings was 291, where all of them except for one had 64 frames. There was one recording that only had 20 frames due to a mistake during the echocardiography. In addition, some patients had more or less than 5 recordings due to technical errors. This means that the data set on average contains 5 recordings from each patient. These 5 recordings are different image views of the heart, and are obtained by positioning the probe as described in section 2.6. The views are summarized in table 3 with their explanations.

Table 3: The image views and their explanations.

View	Full name
PLAX	Parasternal long-axis
PSAX	Parasternal short-axis
A4C	Apical four-chamber
A2C	Apical two-chamber
ALAX	Apical long-axis

The collection of the complete data was done in a random manner. Patients who were scheduled to do an echocardiography were asked if the recordings could be used for research purposes. The recordings from those who agreed were added to the data set used in this paper. The recordings from the different patients are therefore independent.

3.2 USTB

The UltraSound ToolBox (USTB) is a MATLAB toolbox used for processing ultrasonic signals [51]. It is the result of a collaboration between several ultrasound research environments, where NTNU in Trondheim and UiO in Oslo were the contributors from Norway. The aim of the toolbox is to facilitate the comparison between processing techniques in a more accurate way, as well as encourage the publication of data sets and algorithms.

The USTB defines a common set of tools including an ultrasound file format (UFF) that makes it possible to share processed an unprocessed data, and a framework for ultrasound signal processing [52]. Figure 17 illustrates the data structure in UFF and USTB as per April 2017. The framework creates a pipeline for image processing, and lets the user implement various stages of the beamforming process defined as a preprocess, a midprocess and a postprocess [5]. The preprocess is usually a form of complex demodulation where the frequency content of the signal is

moved to the baseband. The output of the preprocess is the input of the midprocess, which is the Delay-and-Sum beamformer. Lastly, the postprocessor takes the output of the midprocess as input. The postprocesses can be different types of beamforming and coherence factor calculations.
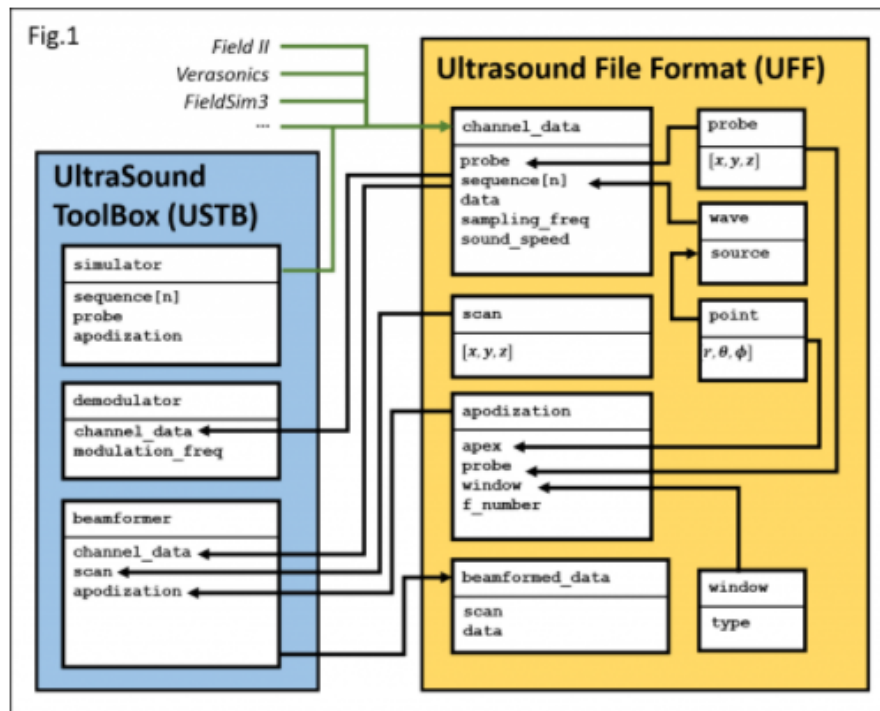
Figure 17: The data structure in UFF and USTB as per April 2017 [51].

3.3   Image Processing

This section explains the most important image processing steps for the grayscale images and for the two different types of aperture energy plots. The processing steps are divided into different subsections in order to present the procedure in an organized manner.

3.3.1   Harmonic Filtering

Harmonic filtering was applied to the raw data from the probe, known as the channel data. This was done by constructing a band-pass filter that passes the second harmonic frequencies and rejects the other harmonic frequencies. The power spectrum of the channel data and the harmonic filtered channel data is shown in figure 18, where the y-axis is given in decibel and the x-axis is given in frequency. The frequency content of the signal is moved to baseband, which means that it has been shifted around the zero-frequency.
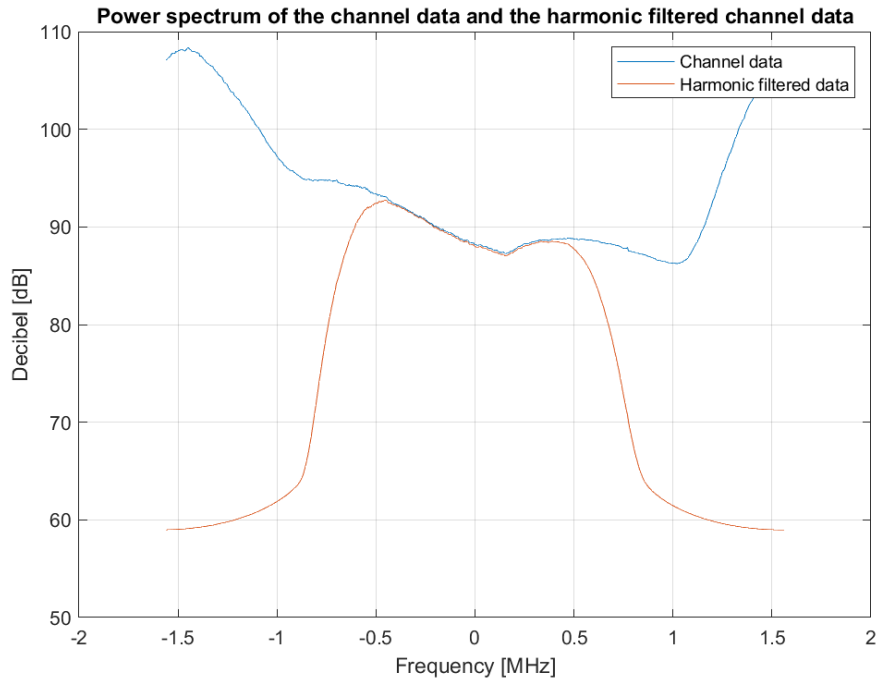
Figure 18: Power spectrum of the channel data and the harmonic filtered channel data.

It is important to mention that the spectrum given in figure 18 is specific for one recording for one patient. The spectrum is therefore not representative for all the patients, but it gives the reader an idea of how the harmonic filtering works on the channel data.

3.3.2   The Scan Setup

The scan setup was defined early in the MATLAB code. This consists of properties like imaging axes and scan depth. Since the data is obtained by imaging the heart, the scanning mode was set to a sector scan. This sector scan consists of an azimuth axis and a depth axis, where the azimuth axis was defined by the USTB channel data object created. The depth axis consists of 512 linearly spaced points, or pixels, with values from 0 to the depth of the ultrasound image acquisition. The pulse center frequency was set to 1.5638 MHz.

3.3.3   Beamforming

The DAS beamforming was set up using the USTB midprocess object. This DAS midprocess was set up with a Hamming window as an apodization function on both transmit and receive. The F-number was set to 5 on transmit and 1.75 on receive. Table 4 shows the different parameters that were set. The delayed data was also extracted in order to calculate the CF.

Table 4: Overview of the different parameters set in the DAS midprocess.

Parameter	Transmit	Receive
Apodization function	Hamming window	Hamming window
F-number	5	1.75

3.3.4   Amplitude Plot

To visualize how different levels of aperture blockage can reduce the reflected signal energy to the transducer, amplitude maps of this energy were constructed. The process of constructing these maps was first introduced in another paper in 2020 [5]. The explanations and equations in this section is based on this paper as well as section 3.2 in the project report that is the basis for this master thesis [1].

The beamformed and filtered channel data is denoted as $y(i, j, k, l)$, where i is the number of range samples, j is the number of elements, k is the number of beams and l is the number of frames. A range of the total number of samples, N_s, was used to find the amplitude information of the channel data. This range was defined as a depth region with a start value, R_s, and end value, R_e. Energy from each depth inside this region was summed for each beam. Since the channel data is complex, the absolute value was taken to keep the amplitude information and remove the phase information. The mean over the range of samples was also taken, which reduces the channel data with one dimension. This results in the channel data given by equation 7.

$$P(j, k, l) = \frac{1}{R_e - R_s} \sum_{i=R_s}^{R_e} |y(i, j, k, l)| \tag{7}$$

The energy over the aperture was obtained by squaring the channel data. This data is denoted as $A(j, k, l)$ in equation 8. The logarithm was taken to display the amplitude maps in a decibel scale.

$$A(j, k, l) = 20 \cdot \log_{10}(P(j, k, l)) \tag{8}$$

The energy for each beam, b_n, was displayed in a mesh grid by interpolating the 10x19 subapertures to 48x32 subapertures. Each beam can be thought of as a small rectangular that builds up the resulting image. As explained above, the energy in each rectangle is summed over the specified depth region. In figure 19, the depth region is depicted in blue. The x- and y-direction are the azimuth and elevation direction, respectively.
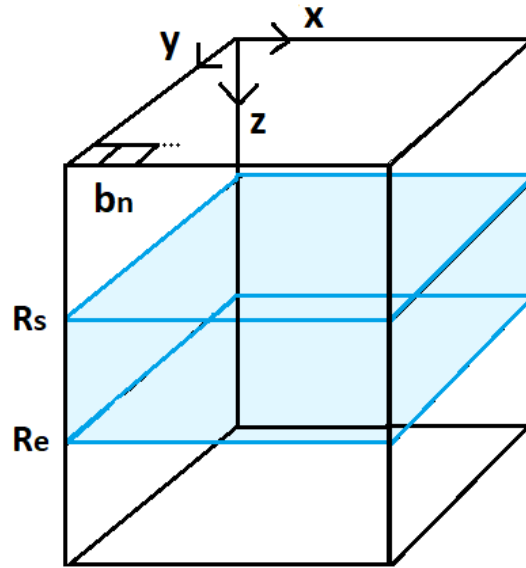
Figure 19: Illustration of how the amplitude maps are constructed, where R_s and R_e define the blue depth region.

The energy was normalized with respect to the individual maximum for all the beams. This is done by using equation 9 [5]. The max-operator returns one value for each beam.

$$A(j,k,l) = A(j,k,l) - \max_{\{j,k\}}\{A(j,k,l)\} \tag{9}$$

An example of an amplitude map is shown in figure 20. Each rectangle in the map contains energy from one beam, and the beam-number is depicted in red in the left corner.
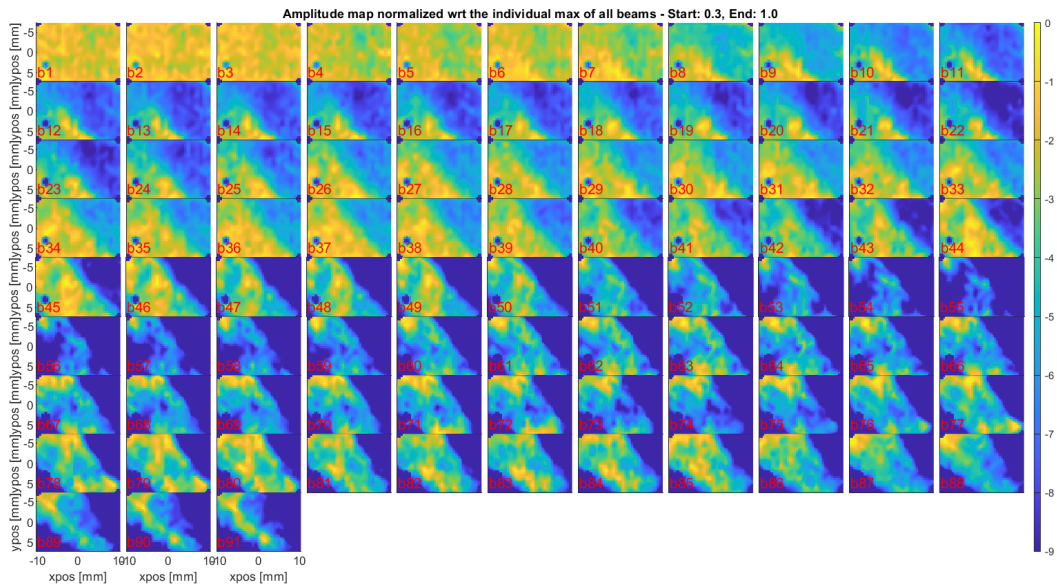
Figure 20: Amplitude map of the aperture energy normalized with respect to the individual maximum of all beams with the scale of attenuation set to 0 to -9 dB.

The scale of attenuation in figure 20 was set to range from 0 dB to -9 dB, and the colours representing the energy were different shades of yellow, green and blue. A yellow colour represents a lot of reflected energy, meaning that there is almost no attenuation of the energy due to blockage of the ribs. The green and blue colours represent attenuated energy, where a deep blue colour means a high attenuation of energy. In figure 20 it is clear that the first beams contain the energy with the least amount of attenuation. It is also evident that there is most likely a rib blocking the upper right and lower left corner of the aperture because of the high attenuation level here.

At -6 dB half the energy in the signal is attenuated. Based on this fact, one can change the scale of attenuation to best visualize the energy reduction. In figure 20 it is clear that signal energy lower than -6 dB is represented with a darker blue colour. In figure 21 -6 dB is represented with a green/yellow colour, meaning that the overall energy looks higher and more uniform even though it is the same signal as in figure 20. The same level of energy attenuation can therefore be represented by different shades of colours by changing the scale of attenuation.
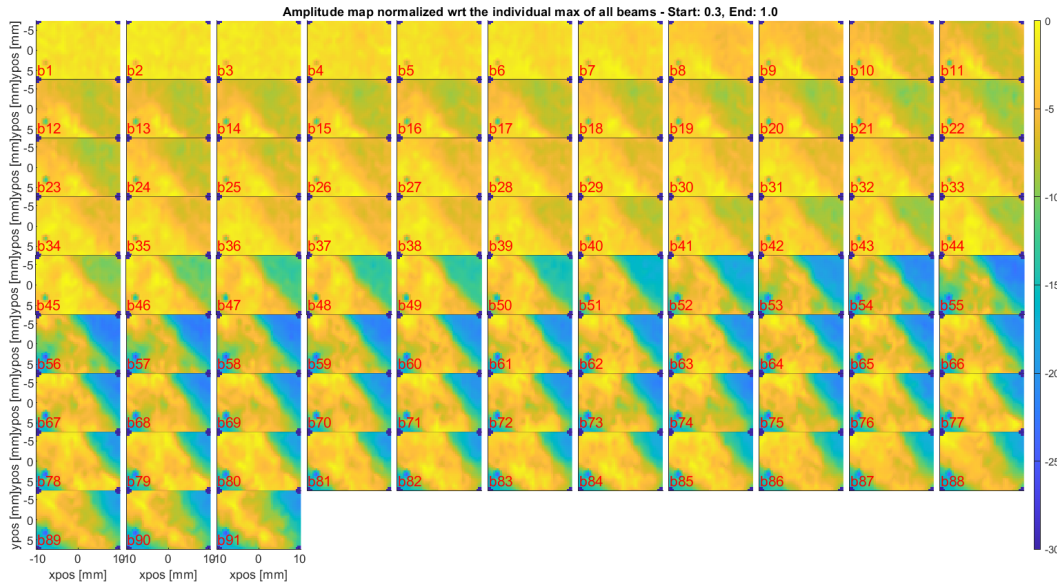
Figure 21: Amplitude map of the aperture energy normalized with respect to the individual maximum of all beams with the scale of attenuation set to 0 to -30 dB.

A number of different depth regions were tested to see which values for R_s and R_e were the best fitted. Figure 22 shows an amplitude map for the region 0-30% of the total depth, while figure 23 shows the region 30-100%. This means that R_s and R_e were set to 0 and $0.3 \cdot N_s$, respectively, for the first amplitude map. For the second amplitude map, R_s and R_e were set to $0.3 \cdot N_s$ and $1.0 \cdot N_s$, respectively. The scale of attenuation was set to 0 to -18 dB for both figures in order to properly view the difference between them.
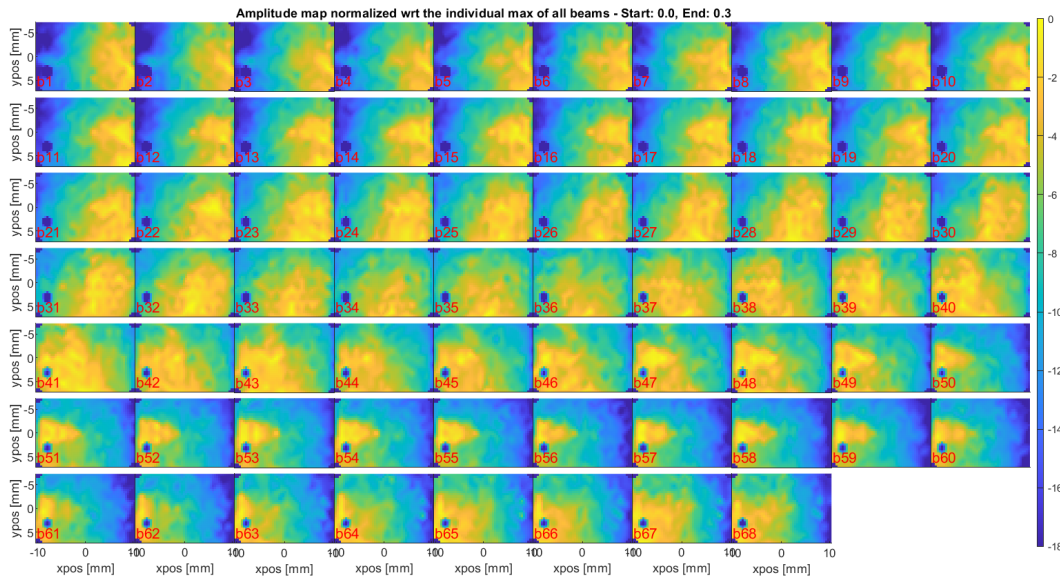
Figure 22: The energy map from the first frame of one of the recordings which shows the energy in the region closest to the transducer, 0-30% of the total depth.
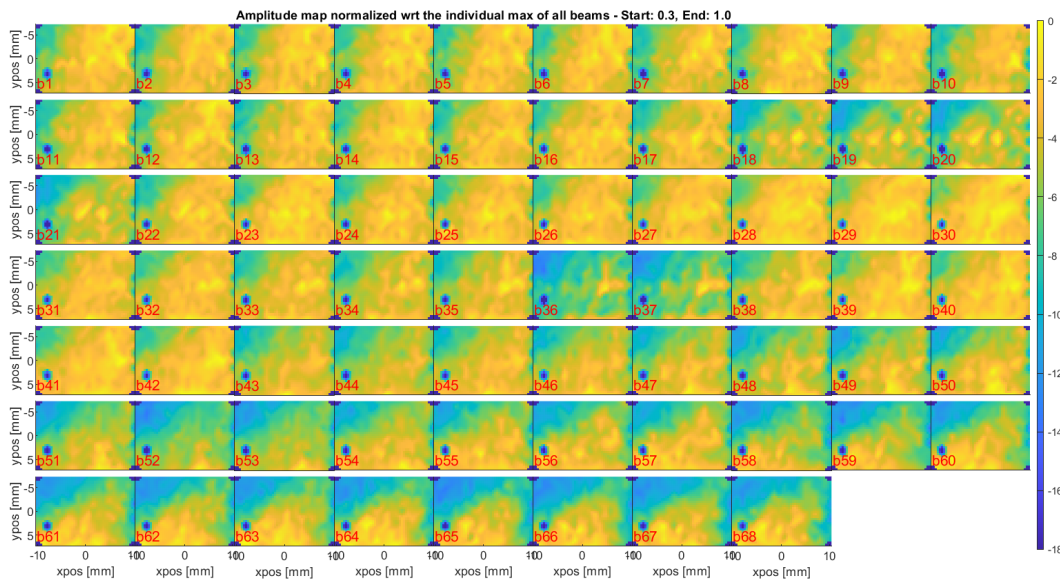
Figure 23: The energy map from the first frame of one of the recordings which shows the energy in the region 30-100% of the total depth.

It is evident that there is a clear difference between the amplitude maps above even though they are from the same frame of the same recording. The energy in figure 22 seems to be focused in one spot, and there is also more low signal values than in figure 23. It is also clear from figure 23 that the reduction of signal energy is somewhat constant in both the azimuth and elevation direction. This comparison illustrate how the energy is not stable in the near-field of the aperture. An explanation for this is the fact that the many thousands elements in the probe are mapped to only 190 elements, meaning that the elements are larger. Larger elements will result in increased

sensitivity for the direction the beams are transmitted in. It is approximated that the elements have a 45 degree directivity, which means that the elements receive the signal more efficiently deeper in the image region than close to the transducer. This is the reason why R_s and R_e were set to $0.3 \cdot N_s$ and $1.0 \cdot N_s$ in this paper.

Another way to visualize the amplitude maps is to take the mean of the beams. The data is then reshaped to a 10x19 grid, showing the energy from all the beams in one rectangle. These dimensions were chosen because the total number of elements in the probe is 190. Figure 24 is the mean of the amplitude map in figure 23.
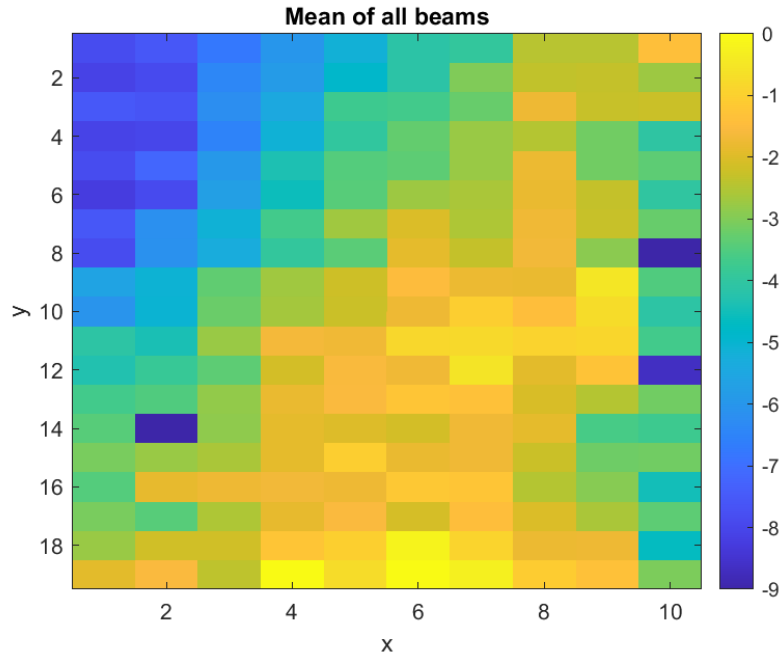
Figure 24: Amplitude plot when taking the mean of the beams in the amplitude map.

3.3.5   Traffic Light Plot

During an echocardiography the cardiologist has a lot of things to focus on, like keeping the probe still and in the right position at the same time as assessing the heart on the ultrasound screen. It is therefore important that the amplitude plot is as simple and intuitive as possible if it shall be used as a tool for the cardiologist to see aperture blockage caused by the ribs.

One way to simplify the amplitude plot is to reduce the amount of colours in the attenuation scale. This can for example be three different colours that represent different energy levels in the signal. Intuitive colours for this is green, yellow and red, which are the colours of a traffic light. A green colour would then mean that there is a lot of energy in the reflected signal, which will correspond to little to no aperture blockage by the ribs. A yellow colour would mean that there is some reduction of energy in the reflected signal. A red colour would mean that a significant amount of the energy in the signal is attenuated, and that there potentially is a ribs blocking parts of the aperture. An

example of a simplified version of the amplitude plot in figure 24 is shown in figure 25.

Traffic light plot
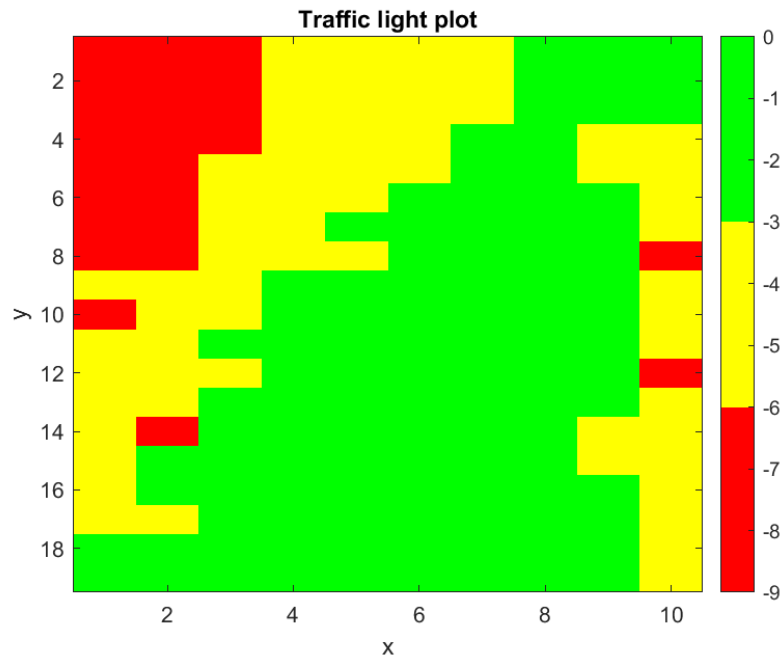
Figure 25: A simplified version of the amplitude plot in figure 24.

The scale of attenuation is divided into three energy levels where green represents energy from 0 dB to -3 dB attenuation, yellow represents energy attenuated more than -3 dB to -6 dB, while red represents energy attenuated more than -6 dB. The reason why the red colour was set to this level of attenuation is because only half the signal energy is left if the signal is attenuated with -6 dB. A low signal energy can reduce the image quality in an echocardiography, which means that the cardiologist wants a traffic light plot containing as much green as possible.

3.4   Data Visualization

A video of the amplitude plots and the ultrasound grayscale images was made in order to properly compare them. This was done by looping over the 64 frames for each recording to create a subplot figure of the grayscale image and the amplitude plot for each frame. Every subplot figure was appended to the previous one made, meaning that all the 64 subplots created a GIF. This GIF was then converted to a video in MPEG-4 format by a custom made MATLAB function. The framerate was set to 15, which means that the videos show 15 frames per second. Two examples of a subplot of one frame for one recording is shown in figure 26 and figure 27. The image view in this specific recording is the PLAX view.
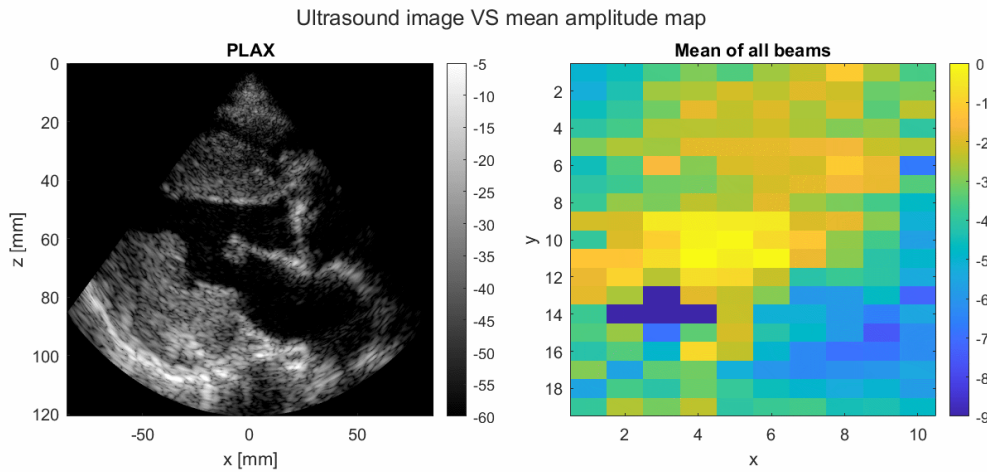
Figure 26: An example of a subplot figure of one frame of the grayscale image and the mean amplitude map.
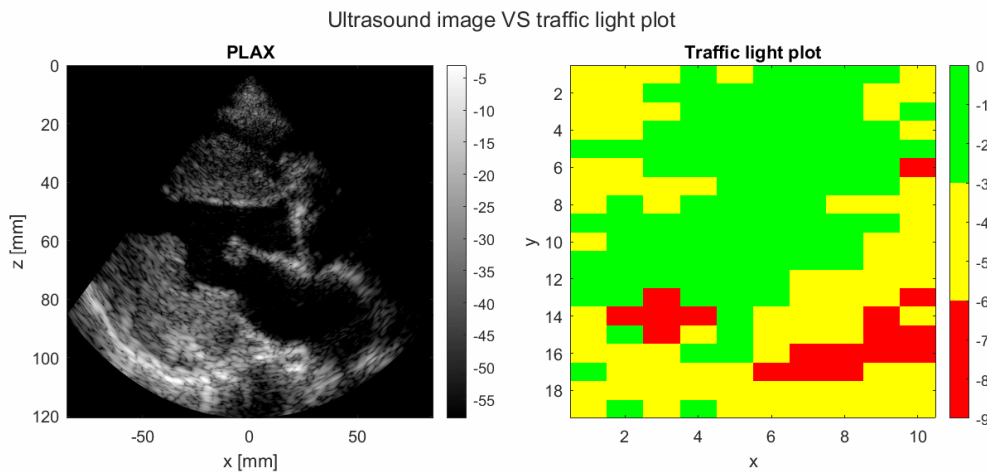
Figure 27: An example of a subplot figure of one frame of the grayscale image and the traffic light plot.

The grayscale image showing the heart was created using a function called *pcolor* in MATLAB which displays the data as an array of colored cells. The colormap was set to the default colormap in MATLAB called *parula*. In order to get a grayscale image, the colors in the colormap were set to *gray*. The dynamic range and gain was set to 55 dB and 5 dB, respectively. The depth axis, z, is given in millimeters, and varies from view to view.

In order to make the videos as optimal as possible, some adjustments needed to be implemented for both the amplitude plots and the grayscale images. Every frame in the grayscale video was normalized against the maximum value of the first frame for the purposes of removing flicking of the signal strength. For the amplitude plots it was necessary to apply a frame filter to smooth out the variations in the reflected signal values throughout the video. This was done by first defining a ramp of filter delays which weight the most recent frames highest. These filter weight always sums up to 1. The number of filter weights is as long as the filter length, unless the number of frames available is less than the filter length. If the filter length is for example set to 5, then the first

five frames are weighted with the number of frames available. This means that the second frame only gets weighted with the first frame, the third frame only gets weighted with the two previous frames, etc. Equation 10 is used to calculated the filter weights, W. F is a vector with integer values from 1 to the filter length, while N_{frames} is the number of frames available when there is less available frames than the filter length. The maximum value of N_{frames} is the filter length.

$$W = \frac{F(1 : N_{frames})}{\sum_{n=1}^{N_{frames}} F(1 : N_{frames})} \tag{10}$$

An overview of the filter weights for different numbers of available frames are shown in table 5 when the filter length is set to 5. The filter weights are used as coefficients in the *filter* function in MATLAB in order to get the filtered data.

Table 5: Overview of the filter weights for different numbers of available frames when the filter length is set to 5.

Frames available	Filter weights
1	[1]
2	[0.3333, 0.6667]
3	[0.1667, 0.3333, 0.5]
4	[0.1, 0.2, 0.3, 0.4]
5 (or more)	[0.0667, 0.1333, 0.2, 0.2667, 0.3333]

3.5   Calculations

The main calculations done in this master thesis were the GIC values and the different energy levels. These calculations were done for each recording in MATLAB, and the results were saved in an Excel-file.

3.5.1   GIC

The CF values for each frame was calculated first in order to further calculate the GIC value. This was done by using equation 4. The number of elements, M, in the azimuth direction was set to 19, while the number of elements, N, in the elevation direction was set to 10. The output of the equation is a coherence metric of CF values for every pixel in the image. As mentioned in section 2.8.3, the GIC calculates an average over these CF values for a defined range gate. This range gate was set to the last 70% of the z-pixels in equation 6, meaning that $Z_1 = 0.3 \cdot Z$ and $Z_2 = Z$. This depth range is the same range used for the amplitude plots. Since the depth axis consists of 512 linearly spaced points, the range gate resulted in $Z_1 = 155$ and $Z_2 = 512$. The number of x-pixels in the azimuth direction, X, varied from recording to recording. A summary of the parameters and values used are given in table 6 with an explanation.

Table 6: Summary of the parameters and the values used to calculate the GIC.

Parameter	Explanation	Value
M	Number of elements in the azimuth direction	19
N	Number of elements in the elevation direction	10
Z	Total number of depth pixels	512
Z1	Start pixel in the range gate	155
Z2	End pixel in the range gate	512

3.5.2   Reduction of Energy

The percentage of the three energy levels was also calculated. This was done by looping through the signal energy in the 19x10 subapertures and counting the number of values within the three different limits introduced in section 3.3.5. Equation 11 was used to find the percentage values of the different energy levels. B is the percentage of energy for either the green, red or yellow limit, while $b(elements)$ is the number of signal values in the subapertures that are within the chosen limit. The total number of elements, $N_{elements}$, is set to 190.

$$B = \frac{100}{N_{elements}} \sum_{elements=1}^{N_{elements}} b(elements) \tag{11}$$

The calculation in equation 11 was done for the three limits for every frame in each recording. This means that each recording had $3 \cdot 64$ percentage values, B.

3.6   Simulation of a New Case of Rib Blockage

In this section, simulations of a new case of rib blockage is tested in a water tank. For this case, the energy is not assumed to be reflected back to the transducer after specular reflections at the rib. This type of rib blockage is therefore not mentioned in the article from 2019 as it was here assumed that the ultrasonic energy was reflected back to the transducer [2]. All experimental data was aquired with an 4Vc-D 2D array probe connected to an E95 (GE Vingmed Ultrasound AS, Horten, Norway) ultrasound scanner.

A synthetic ventricle was used to simulate the heart. This ventricle was made up of 10% polyvinyl alcohol (PVA), 10% glycerol, 1% graphite and 79% water [2]. A picture of the ventricle and its harmonic ultrasound image is shown in figure 28.
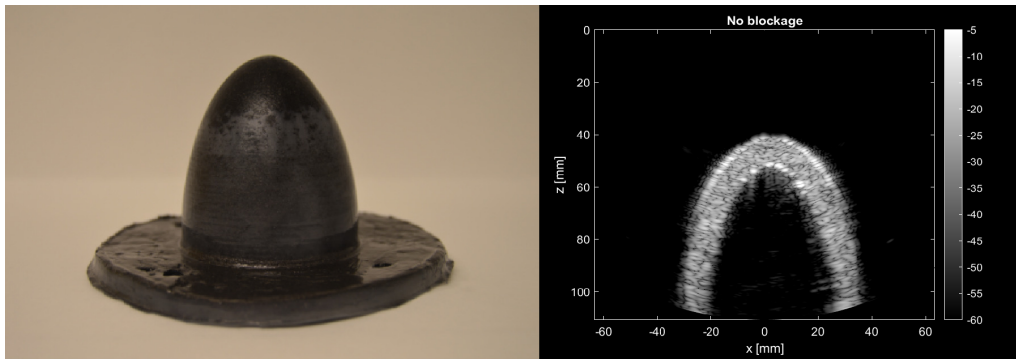
Figure 28: Picture of the synthetic ventricle used to simulate the heart with its harmonic ultrasound image.

A picture of how the experiment was set up is shown in figure 29.

Figure 29: Pictures of how the experiments of the new rib blockage in the water tank was set up.

A closer look at the set up is shown in figure 30. The ventricle was emerged in ionized water, and the probe was set above the middle of it. A black box made of plastic was used to simulate rib blockage. This plastic box was angled to prevent the ultrasonic energy to be reflected back to the

transducer.
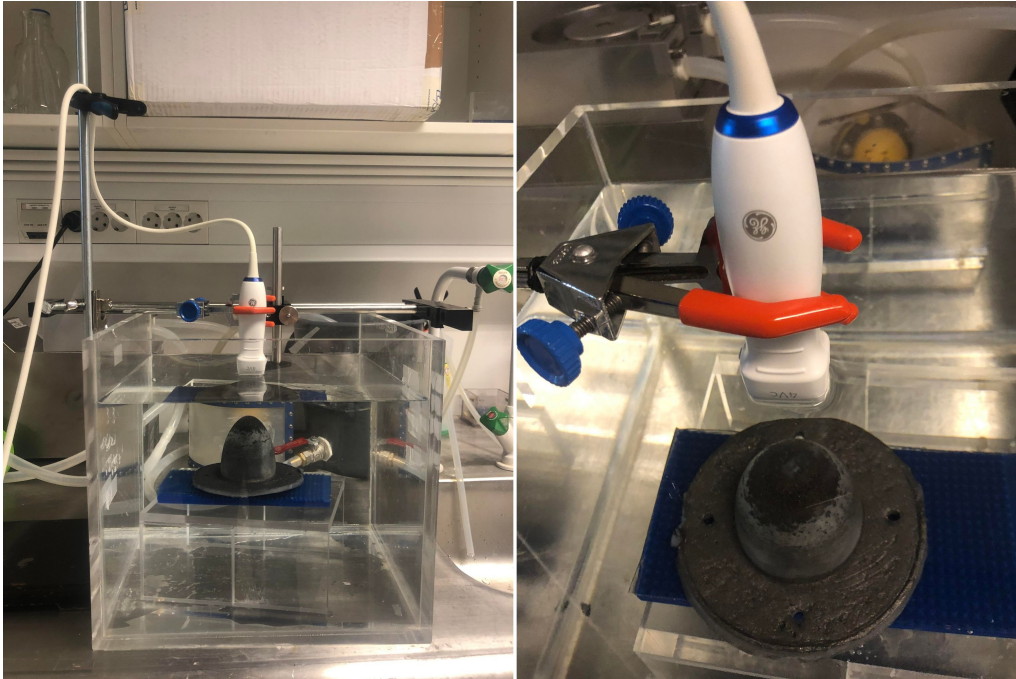
Figure 30: Pictures of how the experiments of the new rib blockage in the water tank was set up.

Three experiments were conducted, where the black plastic box was positioned to simulate different kinds of blockage. The three types of blockage was in the azimuth direction, the elevation direction and a diagonal blockage in both directions. This is shown in figure 31, where the diagonal blockage is to the left, the azimuth blockage in the middle and the elevation blockage to the right. The ventricle was moved a bit when simulating blockage in the elevation direction to image more of the curvature of it. This was done because it would be easier to see the effect the blockage had on the resolution in the elevation direction, as well as the focus.
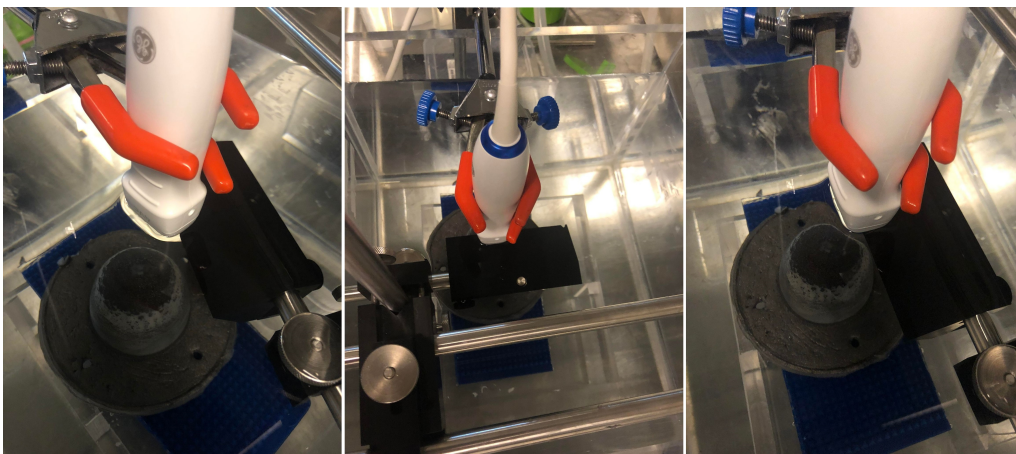
Figure 31: Pictures of the set up for the three different types of blockage.

4   Results

In this chapter, the results are presented in separate sections. The purpose of the first section is to show some examples of the five different cases explained in section 2.6. The next section will demonstrate the results from the simulations of a new case of rib blockage. The two following sections contain the GIC values and the energy levels for the different image views, as well as the differences between men and women. The second last section contains the GIC values and the differences in the energy levels for different heights and BMI's. The purpose of the last section is to show some trends of the GIC values, the blockage levels and the image quality that occurred in the processed data set.

For assessing the image quality in the ultrasound videos and the blockage in the traffic light plots, as well as identifying trends in the data, the 22 patients in table 1 was used. The recordings from all the 56 patients were used to produce the statistics presented in section 4.3 and 4.4. The reason for this is that the recordings from the last 34 patients were obtained after the recordings from the first 22 patients were processed, and there were not enough time to process all the recordings as a complete data set. There was also additional information about the last 34 patients, like their height and weight, that were not collected for the first 22 patients.

4.1   Examples of Five Different Cases

The intention of this section is to show some examples of the five different cases explained in section 2.6, which were introduced by Fatemi et al. in 2019 [2]. As previously mentioned, the data set used contained the recordings from the first 22 patients. One frame of the ultrasound recording and the corresponding traffic light plot of the different cases will be shown to illustrate the effect on the image quality. Since image quality in medical ultrasound imaging is complex and often reduced due to a number of different factors, the examples shown may contain a combination of the cases explained. The examples are, however, chosen because they are the ones that best illustrates the five different cases.

An example of case (a) is shown in figure 32. This is the case where the ultrasound energy is reflected outside the rib cage due to specular reflections at the bone surface. This case can be recognized by static clutter in the ultrasound recording. It was evident in the recording of the example in figure 32 that there was static clutter for all the depths to the right. This clutter could also be seen at the top of the image sector where it looked more like a still image than a video for all the 64 frames. In addition, the lateral resolution was poor in the majority of the frames.

Figure 32: An example of a subplot figure of one frame of the ultrasound recording and the traffic light plot for case (a).

The information about this example is summarized in table 7, where the GIC and the energy reduction levels are the mean values for the 64 frames processed. It is evident that the majority of the beams are only attenuated with -3 dB or less, which agrees with the traffic light plot in figure 32.

Table 7: Overview of the information for the example of case (a), where the GIC and the energy levels is the mean values over all 64 frames.

Patient	Gender	View	Mean GIC	Green [%]	Yellow [%]	Red [%]
11	Woman	PSAX	13.35	67.00	30.12	2.88

An example of case (b) is shown in figure 33. This is the case where the ultrasound energy is reflected inside the rib cage after hitting the surface of the ribs. Common consequences of this are static clutter and reveberations at the top of the image sector. It is also possible to see reveberations from the lung flicker with respirations, as well as reveberations from the out-of-scan-plan tissue move with the heart cycle. There was a large amount of static clutter at the top of the image sector in the example in figure 33. There were also some reveberations, and the noise moved and flickered throughout the whole recording.
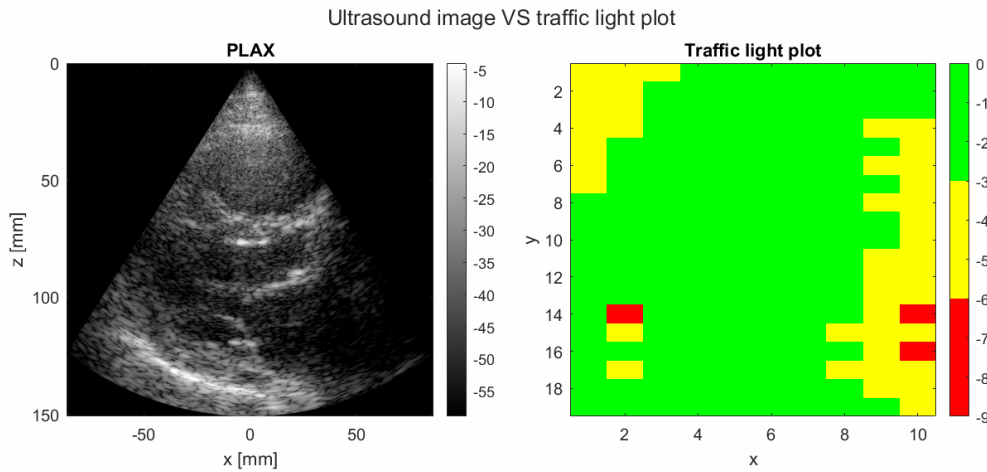
Figure 33: An example of a subplot figure of one frame of the ultrasound recording and the traffic light plot for case (b).

The information about this example is summarized in table 8. Like the example in figure 32, the majority of the beams were attenuated with -3 dB or less. This is also confirmed by the traffic light plot in figure 33.

Table 8: Overview of the information for the example of case (b), where the GIC and the energy levels is the mean values over all 64 frames.

Patient	Gender	View	Mean GIC	Green [%]	Yellow [%]	Red [%]
1	Man	PLAX	16.40	67.85	27.58	4.56

Figure 34 and 35 illustrate two examples of case (c), which is the case where the ultrasound energy is reflected in the soft tissue outside the rib cage before it reaches the heart. This results in reverberations, and is visible as noise in the whole image, as well as static clutter in the near field of the transducer. The example in figure 34 is characterized by noise to the point where it is hard to properly see the structures of the heart. It is also possible to see static clutter, as well as some reverberations, at the top of the image like it was in the example in figure 33. The example in figure 35 is characterized by reverberations at the top of the image sector, as well as noise covering almost half the image region.
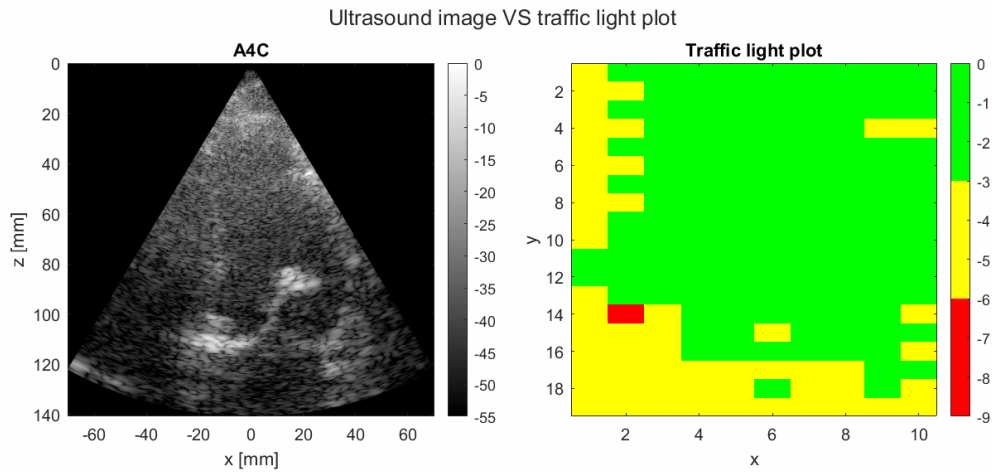
Figure 34: An example of a subplot figure of one frame of the ultrasound recording and the traffic light plot for case (c).
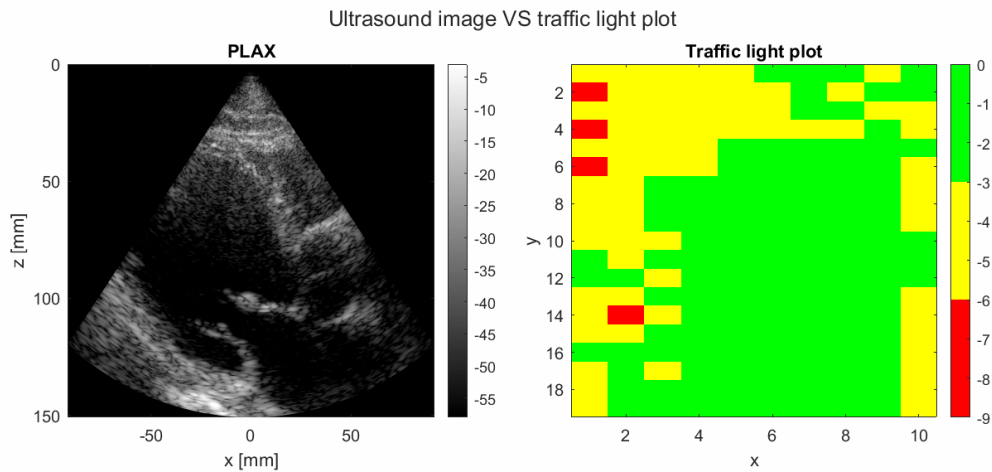
Figure 35: An example of a subplot figure of one frame of the ultrasound recording and the traffic light plot for case (c).

The information about these examples are summarized in table 9. It is evident that the majority of the beams are only attenuated with -6 dB or less, which agrees with the traffic light plot in both examples. There is also approximately no red blockage in the plots.

Table 9: Overview of the information for the example of case (c), where the GIC and the energy levels is the mean values over all 64 frames.

Patient	Gender	View	Mean GIC	Green [%]	Yellow [%]	Red [%]
1	Man	A4C	11.40	59.70	39.51	0.80
2	Man	PLAX	18.40	73.85	24.38	1.77

The example in figure 36 is of case (d) where the heart is partially covered by the lung in the azimuth direction. One side of the ultrasound recording will be cluttered when this happens, and it will move in and out of the image sector with respiration. This effect is easier to see in an actual recording than in an image of the recording. It is, however, still possible to see that the left side of

the example in figure 36 is cluttered with a highly reflective tissue. This noise moved in and out of the image sector.
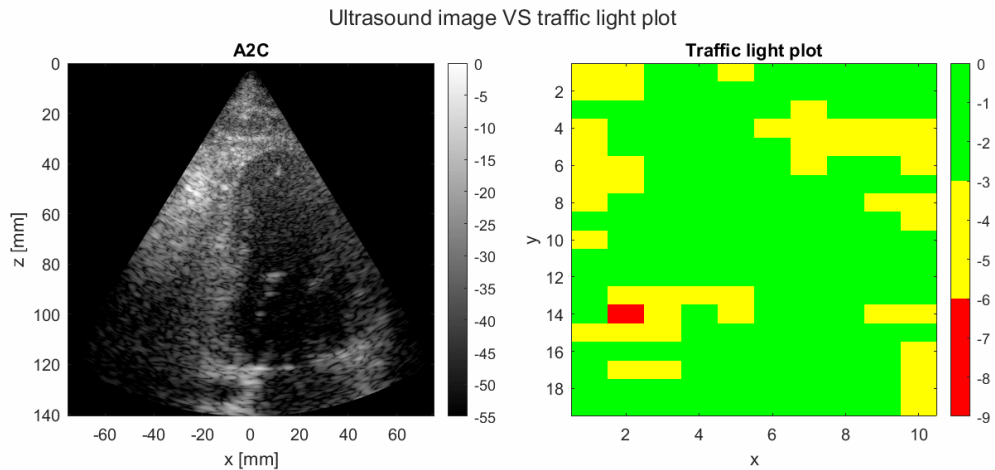
Figure 36: An example of a subplot figure of one frame of the ultrasound recording and the traffic light plot for case (d).

The information about this example is summarized in table 10. The majority of the beams are only attenuated with -3 dB or less, which agrees with the large areas of green in the traffic light plot in figure 36. There is also here little to no red blockage in the plot.

Table 10: Overview of the information for the example of case (d), where the GIC and the energy levels is the mean values over all 64 frames.

Patient	Gender	View	Mean GIC	Green [%]	Yellow [%]	Red [%]
7	Man	A2C	19.20	71.23	27.95	0.81

Figure 37 is an example of case (e). This was the case where the heart was partially covered by the lung in the elevation direction, which could lead to the whole image being cluttered, as well as clutter which flickers with respiration. It could also be possible to see bands of noise in the image. In the example given for this case it was somewhat possible to see both that the clutter flickered with respiration and that there were bands of noise in the image. This example did also have some reverberations at the top of the image sector.
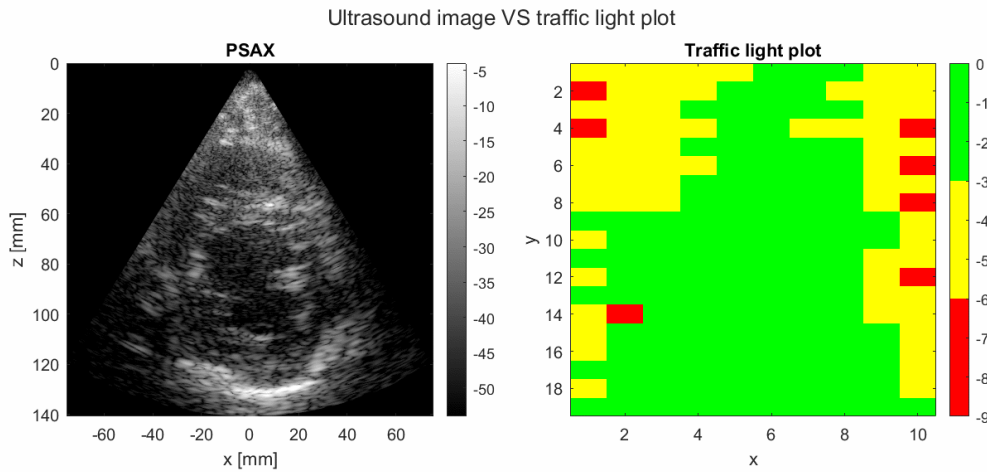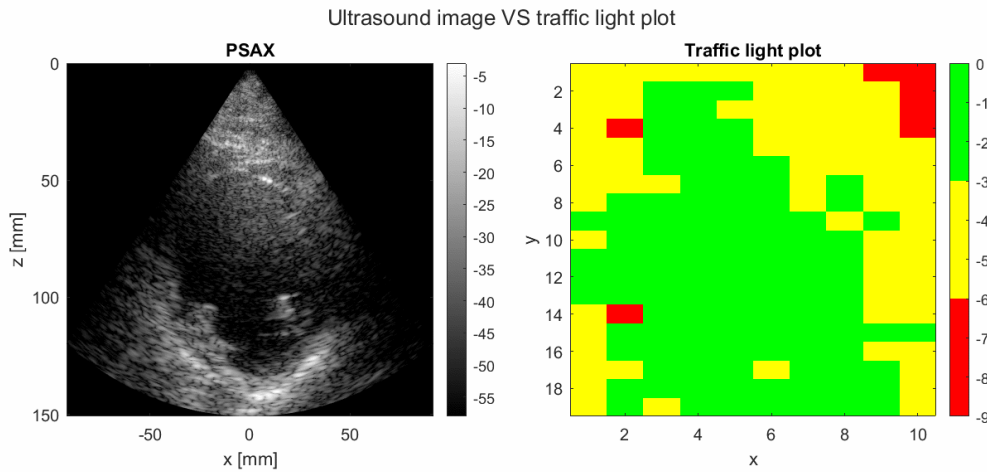
Figure 37: An example of a subplot figure of one frame of the ultrasound recording and the traffic light plot for case (e).

The information about this example is summarized in table 11. It is here evident that there is a reduction of signal energy in both the azimuth and elevation direction in the traffic light plot, which could possibly be a rib blocking the elements. The majority of the plot is, however, green.

Table 11: Overview of the information for the example of case (e), where the GIC and the energy levels is the mean values over all 64 frames.

Patient	Gender	View	Mean GIC	Green [%]	Yellow [%]	Red [%]
2	Man	PSAX	14.11	68.73	30.13	1.14

4.2   A New Case of Rib Blockage

In this section, the results from the simulations of the new case of rib blockage in section 3.6 will be presented. In addition to this, some examples of this type of rib blockage will be given in order to see the effect on the cardiac image quality in real patient data.

Figure 38 shows the same harmonic ultrasound image as in figure 28. The corresponding traffic light plot is also depicted. This is the case where the plastic box was not placed in front of the transducer, meaning that there is no intentional blockage of the elements.
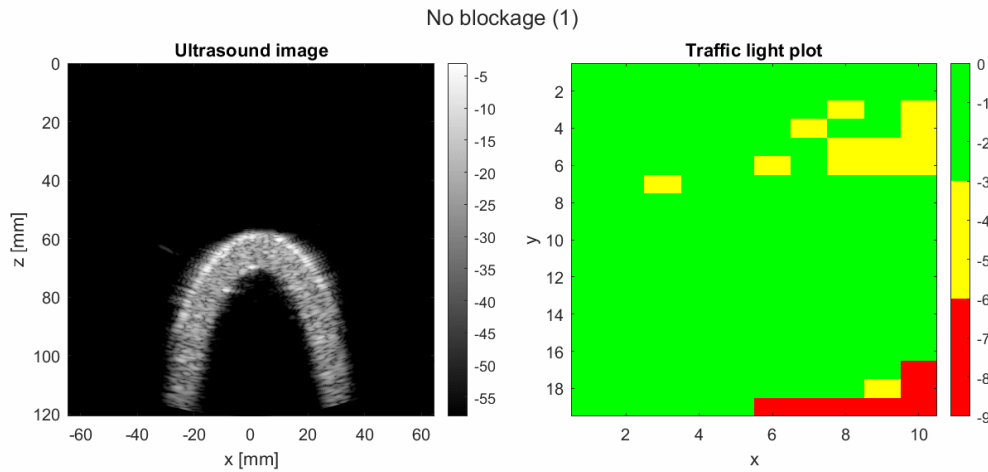
Figure 38: The harmonic ultrasound image and the traffic light plot of the case where the plastic box is not blocking any of the elements.

Figure 39 shows the harmonic ultrasound image and the traffic light plot of the case where the plastic box was blocking parts of the aperture in both azimuth and elevation direction. It is evident that the image quality is not as good as in figure 38. The outline of the ventricle is not as even, and there is a loss of signal and a reduction of lateral resolution at the left of the ventricle where the plastic box was placed. There are also some reverberations in the left of the image which were not in figure 38.
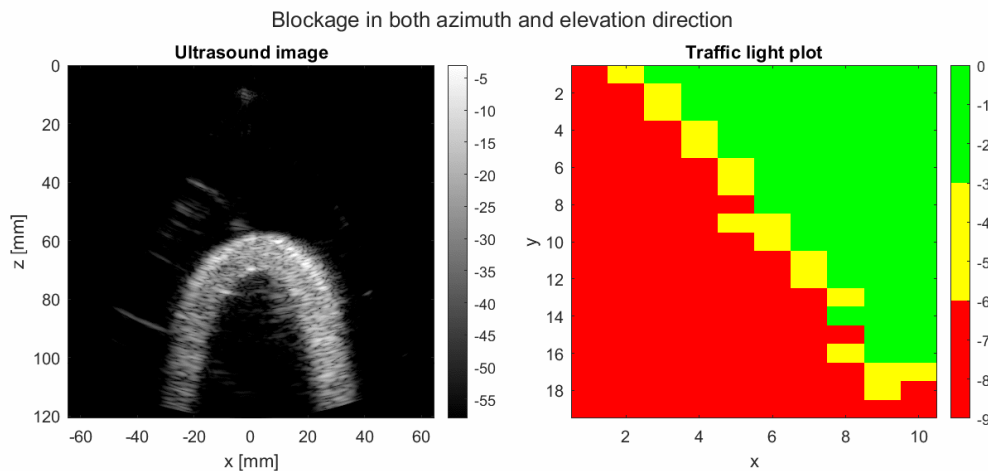
Figure 39: The harmonic ultrasound image and the traffic light plot of the case where the plastic box is blocking some of the elements in both azimuth and elevation direction.

The case where the plastic box was blocking some of the elements in the azimuth direction is given in figure 40. The effects on the image quality is here a lot similar to the effects in figure 39, but the signal loss seems to be greater for this case. There is also a more clear reduction of the lateral resolution.
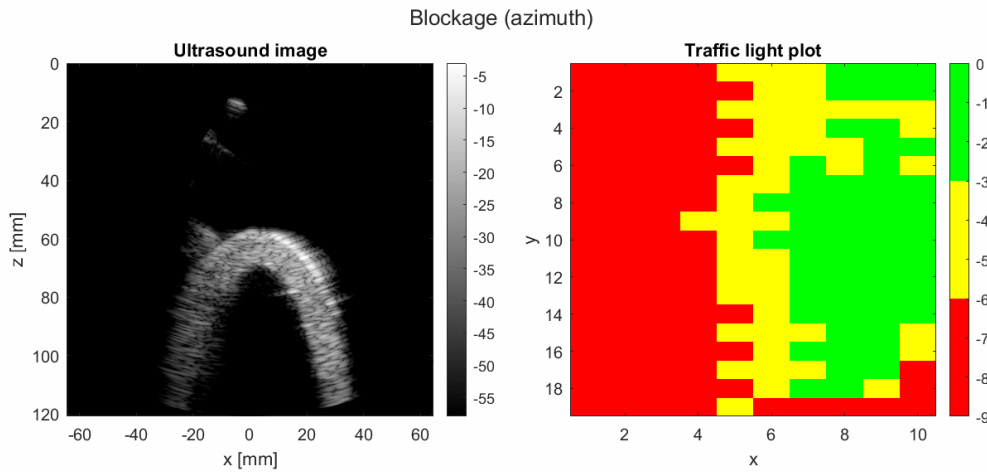
Figure 40: The harmonic ultrasound image and the traffic light plot of the case where the plastic box is blocking some of the elements in the azimuth direction.

Figure 41 shows the results when the plastic box was not blocking any of the elements, but the ventricle was moved so that it was no longer positioned below the centre of the transducer. It is here possible to see some of the symmetry of the ventricle as it looks thicker and a bit more uneven at the edges.
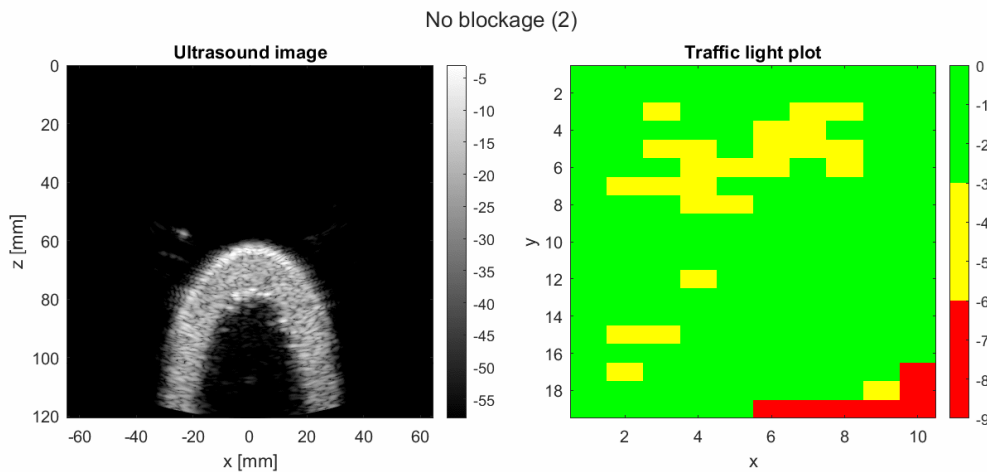
Figure 41: The harmonic ultrasound image and the traffic light plot of the case where the plastic box is not blocking any of the elements, but the ventricle is moved.

The case where the plastic box is blocking some of the elements in the elevation direction is given in figure 42. The signal loss is here more uniform in the image than in figure 39 and 40. The focus is also poorer than in figure 41.
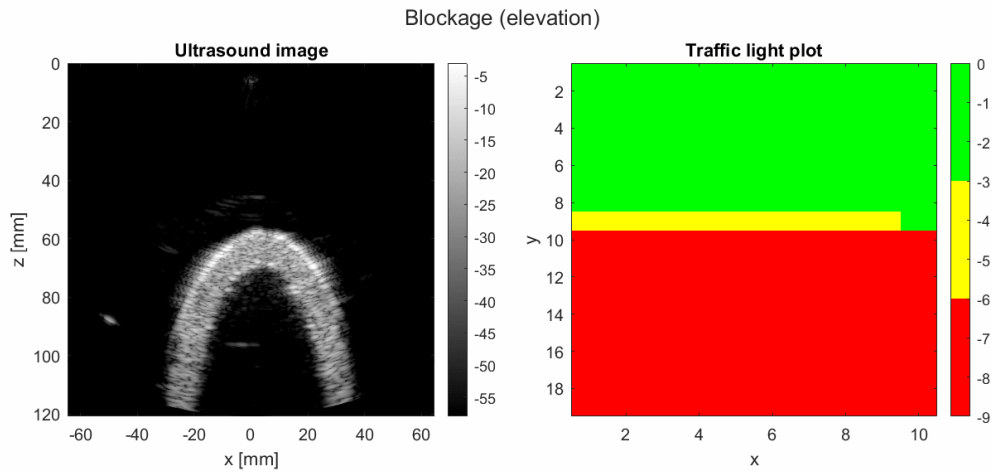
Figure 42: The harmonic ultrasound image and the traffic light plot of the case where the plastic box is blocking some of the elements in the elevation direction.

Two examples of blockage in both the azimuth and elevation direction is given in figure 43 and 44. In figure 43 it is possible to see a large shadow to the left, which is almost completely static throughout the ultrasound recording. There is also a large amount of static clutter in the near field, as well as a reduced lateral resolution in the image. The traffic light plot is also characterized by larger amounts of yellow energy. In figure 44, however, the blockage is more clear in both directions. There is also a shadow to the left, as well as a reduced lateral resolution. The focus was also a bit reduced in this recording.
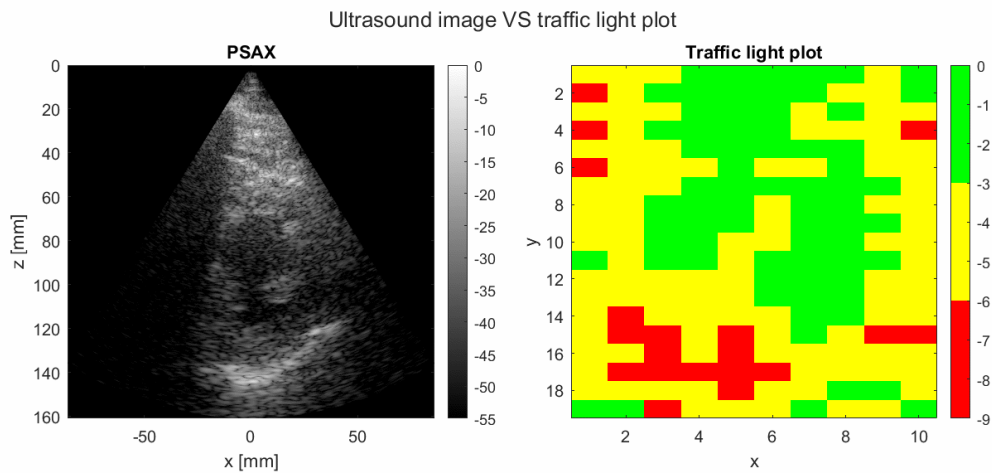
Figure 43: An example of blockage in both the azimuth and elevation direction.
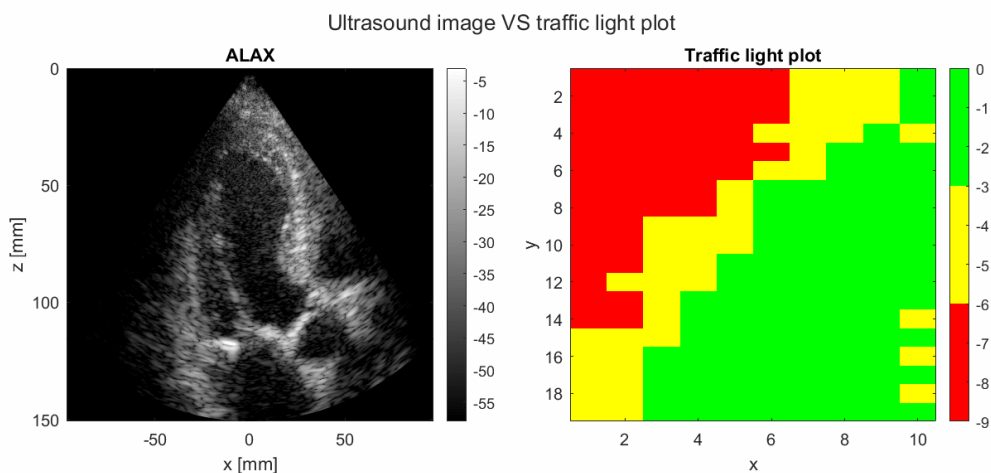
Figure 44: An example of blockage in both the azimuth and elevation direction.

The information about these examples is summarized in table 12, where the GIC and the energy reduction levels are the mean values for the 64 frames processed. It is evident that the example in figure 44 has a larger amount of red energy.

Table 12: Overview of the information for the example of blockage in both the azimuth and elevation direction given in figure 43 and 44.

Patient	Gender	View	Mean GIC	Green [%]	Yellow [%]	Red [%]
16	Man	PSAX	12.55	45.18	48.48	6.34
4	Man	ALAX	16.79	44.16	22.78	33.06

Figure 45 and 46 shows two examples of blockage in the azimuth direction. The blockage is more strictly in the azimuth direction in figure 45 than in figure 46. It is possible to see a shadow to the left in the ultrasound image in figure 45, and the lateral resolution is clearly reduced. There is also static clutter and reverberations in the top of the image sector. Figure 46 did not have a very visible shadow, but the recording had a clearly reduced lateral resolution, especially to the left.
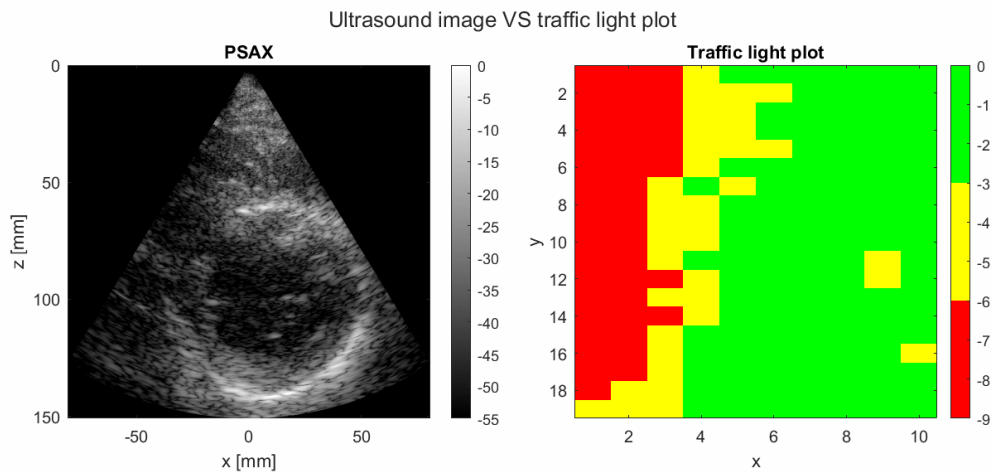
Figure 45: An example of blockage in the azimuth direction.
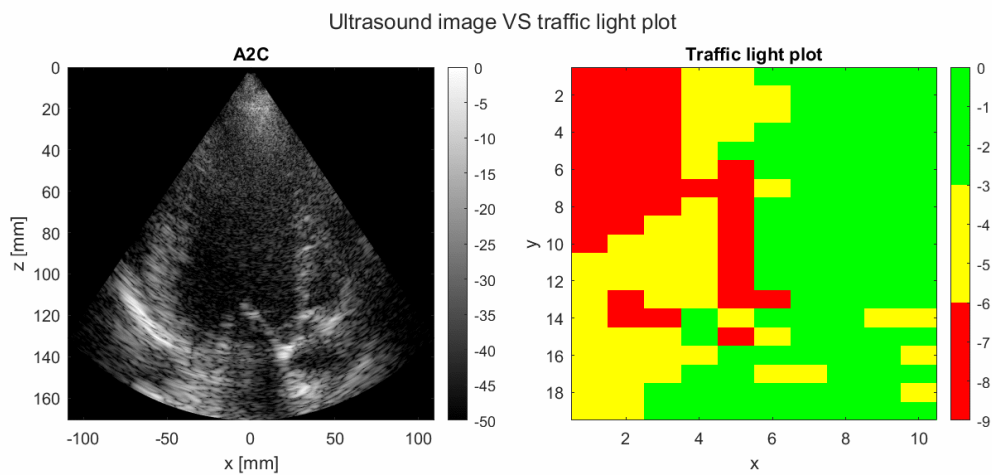
Figure 46: An example of blockage in the azimuth direction.

The information about this example is summarized in table 13, where the GIC and the energy reduction levels are the mean values for the 64 frames processed. About half of the aperture is blocked with the red and yellow energy level for both examples.

Table 13: Overview of the information for the example of blockage in the azimuth direction given in figure 45 and 46.

Patient	Gender	View	Mean GIC	Green [%]	Yellow [%]	Red [%]
14	Man	PSAX	11.92	49.42	29.79	20.80
20	Woman	A2C	14.85	43.84	29.99	26.17

The two next examples in figure 47 and 48 shows blockage in the elevation direction. The blockage in figure 47 is clearly visible in the traffic light plot as it is dominated by the red energy level. There is a lot of noise in the whole ultrasound image, and the focus of the beams seems to be reduced. It is also possible to see a large reverberation artifact to the left in the image. In figure

48, it was possible to see reverberations, as well as a reduced focus. The blockage is here a bit less red than in the previous example.
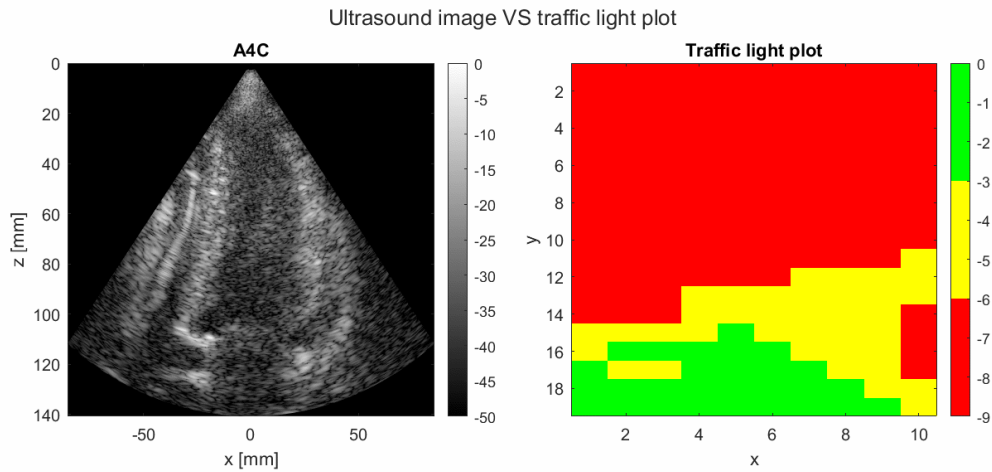
Figure 47: An example of blockage in the elevation direction.
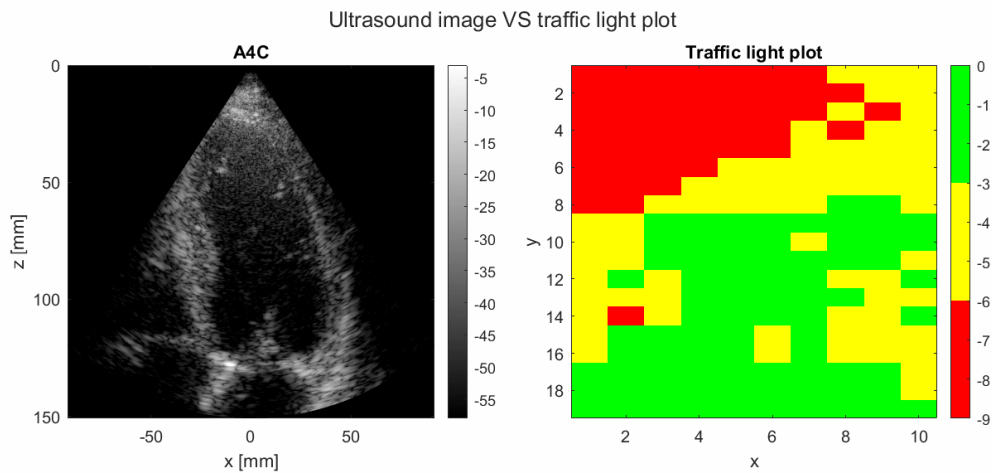
Figure 48: An example of blockage in the elevation direction.

The information about the examples is summarized in table 14, where the GIC and the energy reduction levels are the mean values for the 64 frames processed. As mentioned above, the traffic light plot in figure 47 is dominated by the red energy level. There is also more of the yellow energy level than of the green one. The red blockage for the example in figure 48 is half of the red blockage in figure 47, and the GIC value is higher.

Table 14: Overview of the information for the example of blockage in the elevation direction given in figure 47 and 48.

Patient	Gender	View	Mean GIC	Green [%]	Yellow [%]	Red [%]
3	Man	A4C	13.55	15.39	18.26	66.34
4	Man	A4C	18.18	37.11	31.33	31.56

4.3   Differences Between Image Views

The results for the GIC values and the different energy levels for the five image views in table 3 are presented in this section. The results from the GIC calculations will presented first, followed by the results from the energy calculations. The complete data set was used for the results in this section. This data set contained 37 men and 19 women with a total of 291 recordings.

4.3.1   GIC for Different Image Views

The results for the calculated GIC values for the different image views are shown in the box plot in figure 49. The y-axis shows the GIC values multiplied with 1000, while the x-axis shows the image views. The medians, as well as maximum and minimum values, are summarized in table 15, and are visualized as red lines in the box plot.
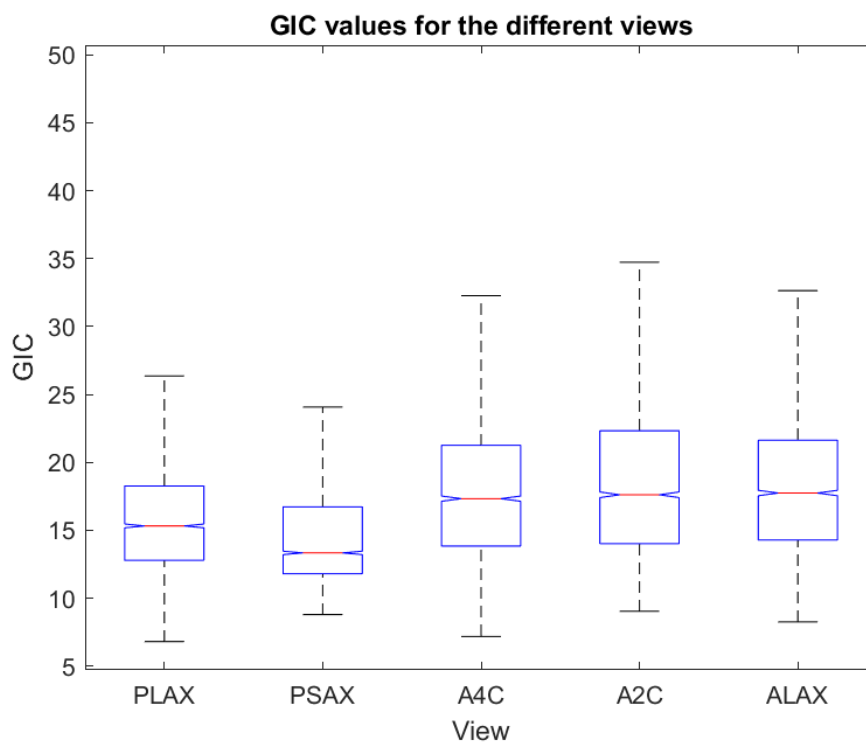
Figure 49: Box plot of the calculated GIC values for the 5 different views explained in section 2.6.

Table 15: Medians, as well as the maximum and minimum, of the GIC values for the different views.

View	Median of GIC	Maximum GIC	Minimum GIC
PLAX	15.33	42.40	6.82
PSAX	13.34	47.90	8.80
A4C	17.33	46.40	7.18
A2C	17.62	48.62	9.05
ALAX	17.75	45.45	8.26

The top and bottom of each box in the box plot represent the 25th and 75th percentiles [53]. The distance between these percentiles is called the interquartile range. The lines above and below the boxes are called whiskers, and they range from the end of the interquartile range to the furthest observation within the whisker length [1]. Observations that are beyond these whiskers are classified as outliers. These outliers are usually visualized as red crosses in the box plot, and are defined as values more than 1.5 times the interquartile range away from the bottom or top of the box. These outliers are made invisible in the box plots given in this thesis to make them cleaner. If the notch in one box is not overlapping with the notch in another box, then the boxes have different medians at a 5% significance level.

It is evident from both the box plot and the table above that all the apical views have significantly higher medians than the parasternal views. The box plot shows that the apical views have the most distance between their 25th and 75th percentiles. The PLAX view also seems to have significantly higher median than the PSAX view, which means that the PSAX view has the lowest median of all the views. This is confirmed in table 15.

Figure 50 and 51 show histograms of calculated CF values for the apical and the parasternal views, respectively. The histograms are made up of 2 frames for each of the first 116 recordings. The y-axis shows the percentage of the values, while the x-axis shows different bins. It is evident that the majority of the CF values are calculated to be in the range 0.0009-0.004 for both the apical and the parasternal views.
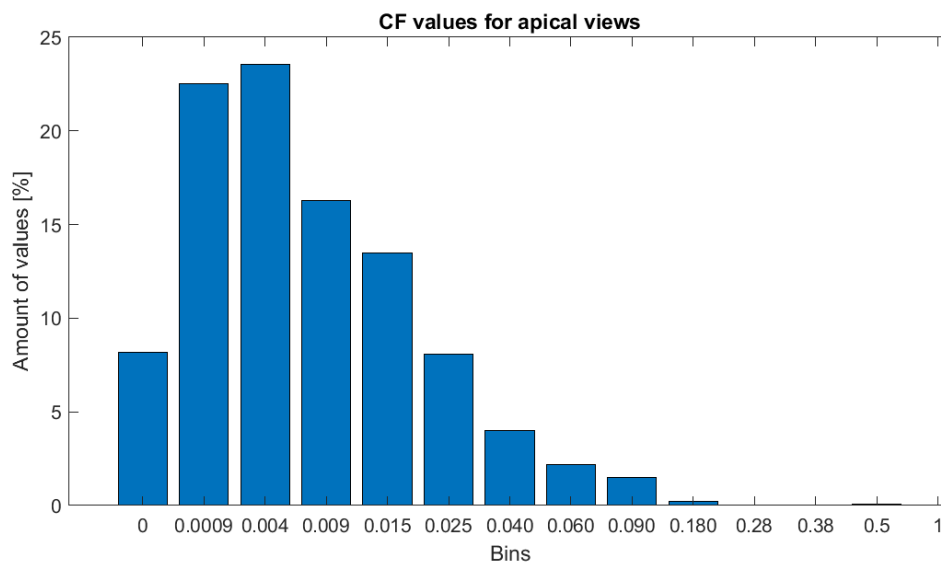
Figure 50: Histogram of the calculated CF values for the apical views.
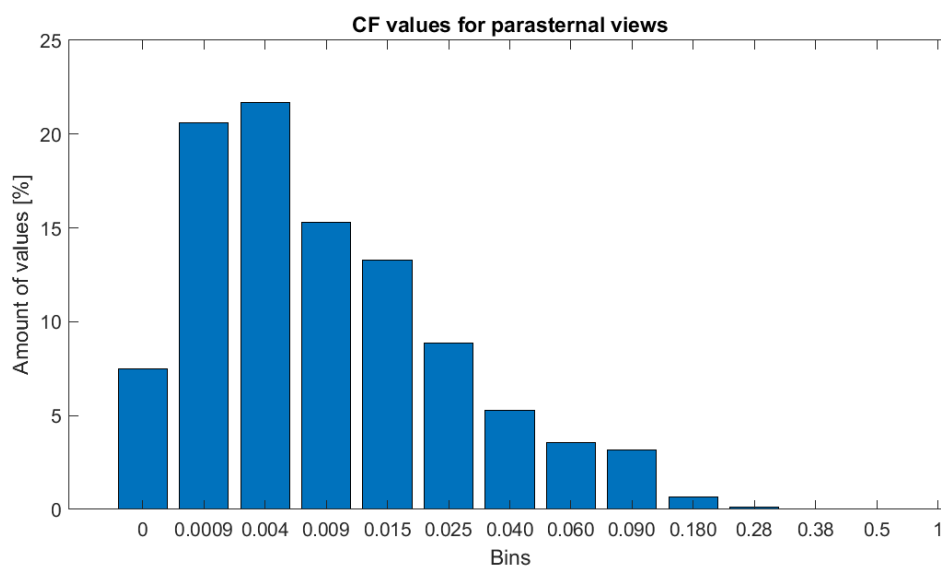
Figure 51: Histogram of the calculated CF values for the parasternal views.

4.3.2   Different Levels of Blockage for Different Image Views

The percentage values for the different energy levels, or blockage, are shown in the box plots in figure 52, 53 and 54. The first box plot is the total amount of green energy, while the other two plots are the total amount of yellow and red energy. The medians of the energy levels are summarized in table 16.
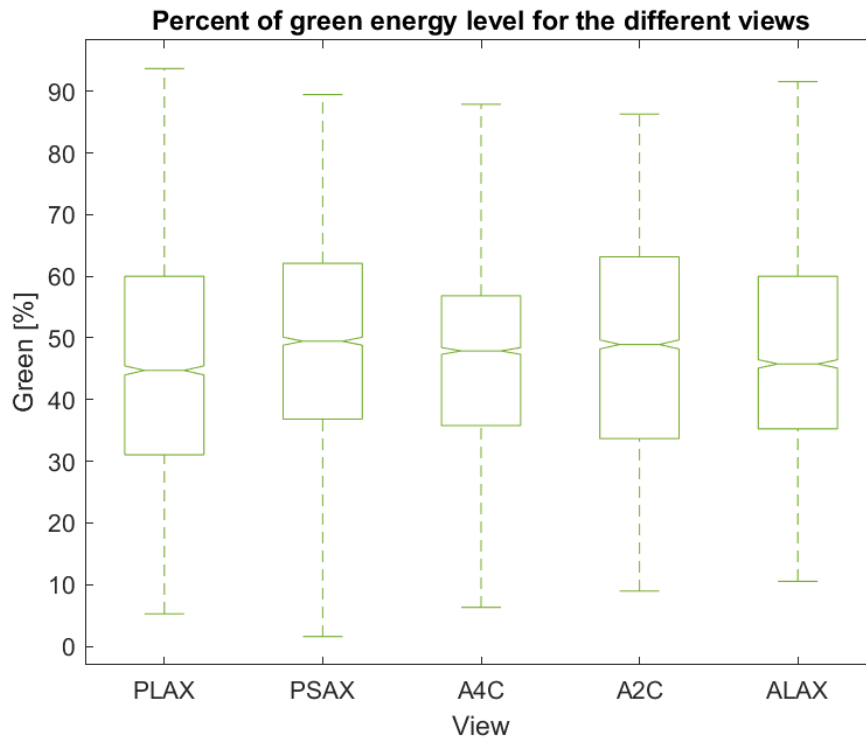
Figure 52: Box plot of the green energy level for the 5 different views explained in section 2.6.
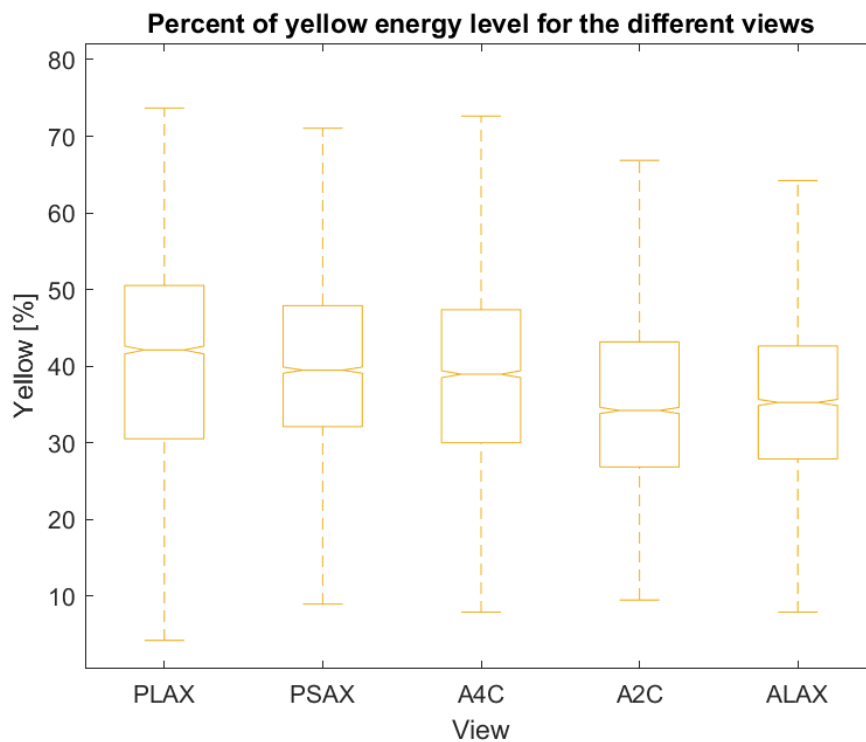
Figure 53: Box plot of the yellow energy level for the 5 different views explained in section 2.6.

Percent of red energy level for the different views
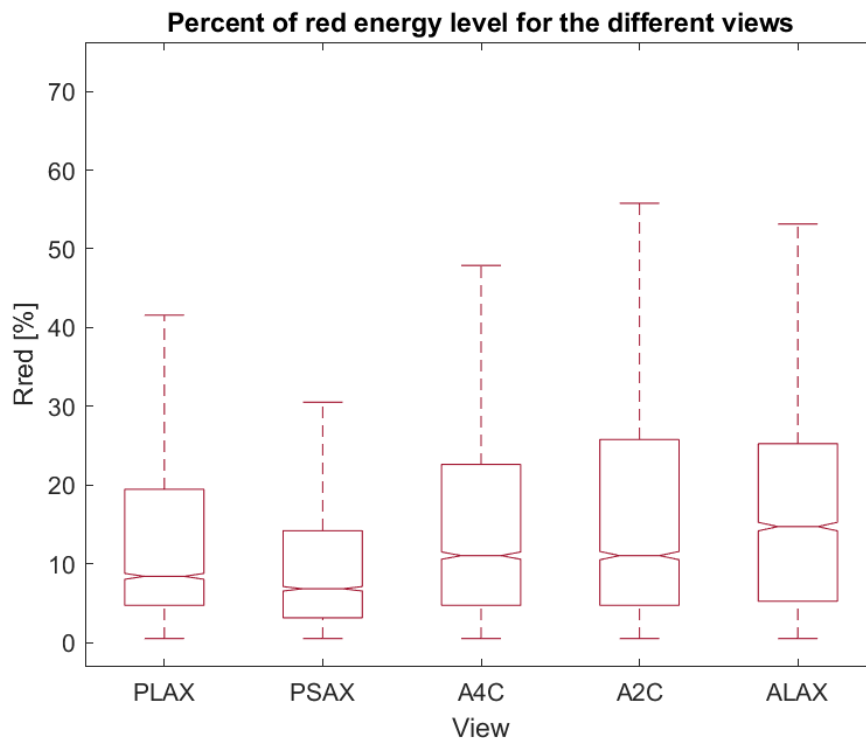
Figure 54: Box plot of the red energy level for the 5 different views explained in section 2.6.

Table 16: Medians of the blocked aperture for the different views given in percent.

View/Median of blockage	Green [%]	Yellow [%]	Red [%]
PLAX	44.74	42.11	8.42
PSAX	49.47	39.47	6.84
A4C	47.90	38.95	11.10
A2C	48.95	34.21	11.10
ALAX	47.79	35.26	14.74

It is evident from the boxes in figure 52 that the ALAX and the PLAX view have significantly lower level of green in the amplitude plots than the rest of the views. The PSAX and the A2C view seem to have the highest level of green. For the yellow energy level in figure 53, it is possible to see that there is a little bigger difference between the views. The A2C view has significantly lower level of yellow than the rest of the views, and the PLAX view has the highest level of yellow. It is also possible to see in table 16 that the A2C view has the lowest median of yellow, while the PLAX has the highest.

The box plot in figure 54 shows that all the apical views have significantly more red energy than the parasternal views. The ALAX view has significantly more red energy than the rest of the views. It is also the apical views that have the most distance between their 25th and 75th percentiles. From table 16 it is evident that the ALAX view has the largest median, while the PSAX view has the

lowest.

4.4   Comparisons Between Men and Women

The purpose of this section is to present the results when both the GIC values and the energy levels are compared for male and female patients. As mentioned, the data set used contained 37 men and 19 women with a total of 291 recordings.

4.4.1   GIC for Men and Women

Figure 55 shows a box plot of the GIC values compared for men and women. The medians and the maximum and minimum values are summarized in table 17.
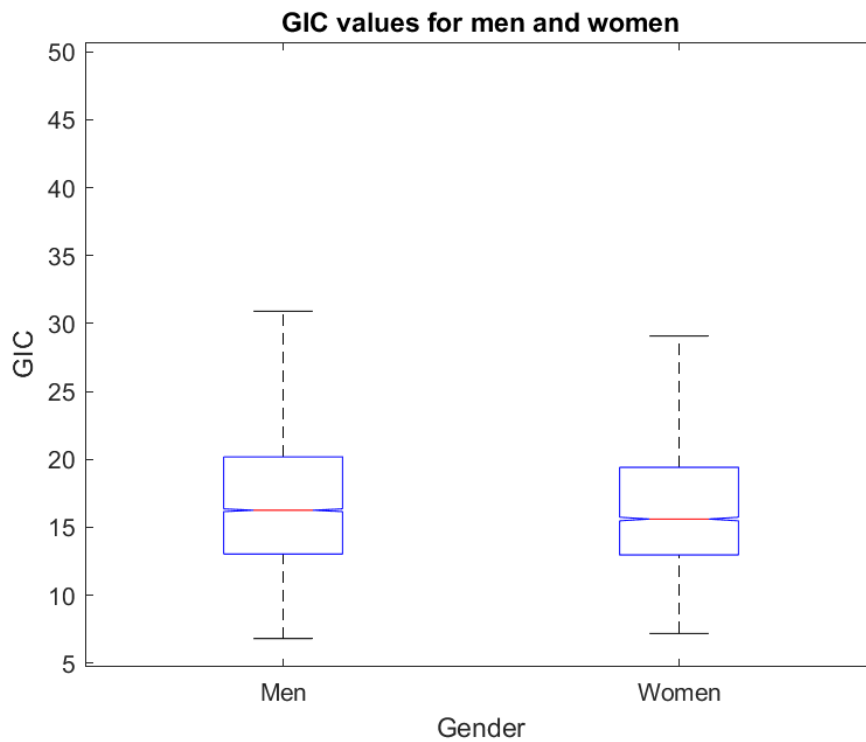
Figure 55: Box plot of the GIC values for 37 men and 19 women.

Table 17: Medians, as well as maximum and minimum, of the GIC values for 37 men and 19 women.

Gender	Median of GIC	Maximum GIC	Minimum GIC
Men	16.26	47.90	6.82
Women	15.61	48.62	7.18

A right-tailed Wilcoxon rank sum test was also conducted [54]. This test tests the alternative hypothesis, which is if the median of GIC for men is higher than for women [1]. The null-hypothesis

is the opposite of the alternative hypothesis, and gets rejected when the p-value < 0.05. A p-value < 0.05 means that the GIC value for men are significantly higher than for women. The resulting p-value was ≈ 0, meaning that the GIC values for men were significantly higher than for women. This is visible in the box plot as the notches do not overlap.

The box plot in figure 56 shows the GIC values for male and female patients for the different image views. The medians of the GIC values are summarized in table 18. It is possible to see that the apical views have the most distance between the 25th and 75th percentiles. The medians of GIC for the apical views are also higher than the parasternal, except the ALAX view for women. It is also evident from both the table and the box plot that women have significantly higher GIC than men for the PSAX and the A2C view. Men have significantly higher GIC than women for the PLAX and the ALAX view.
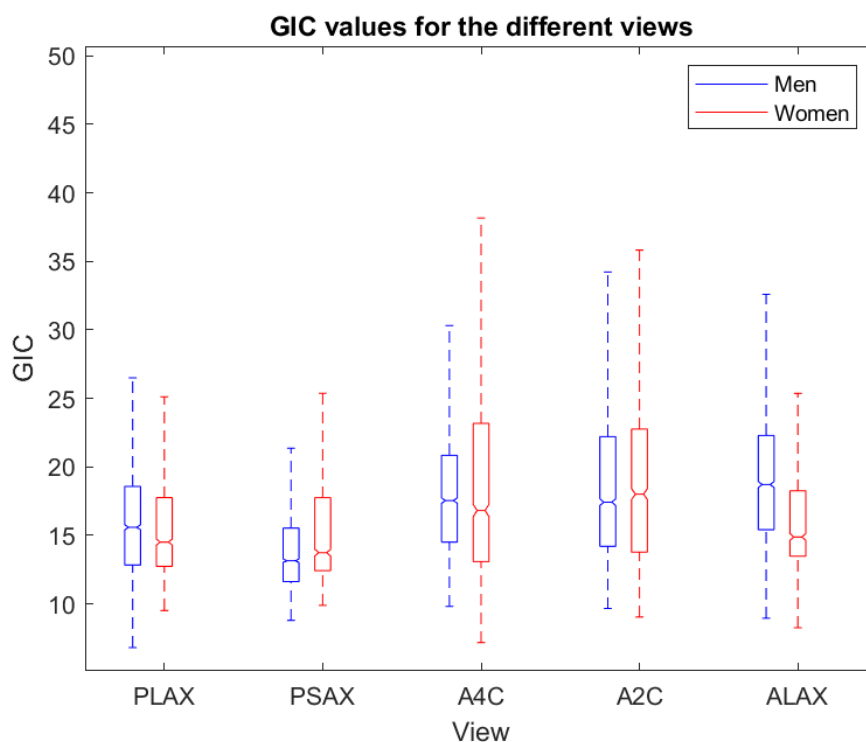
Figure 56: Box plot of the GIC values for male and female patients for the different image views.

Table 18: Medians of the GIC values for both men and women for the different views.

View/Median of GIC	Men	Women
PLAX	15.60	14.51
PSAX	13.15	13.74
A4C	17.54	16.82
A2C	17.43	18.01
ALAX	18.71	14.88

The p-values between men and women for each view are listed in table 19. The test is a right-tailed Wilcoxon rank sum test, as described above. These values confirm the significant differences previously stated. It is only the A4C view that has no significant difference between the genders. The p-value is, however, closer to 0.05 than to 0.95.

Table 19: The resulting p-values for the different image views when comparing the GIC for men and women.

View	p-value
PLAX	0
PSAX	1
A4C	0.11
A2C	0.95
ALAX	0

4.4.2   Different Levels of Blockage for Men and Women

The box plot in figure 57 shows the differences in the three energy levels for men and women. The energy on the y-axis is given in percent, and the x-axis is the different levels of energy. The medians are summarized in table 20.
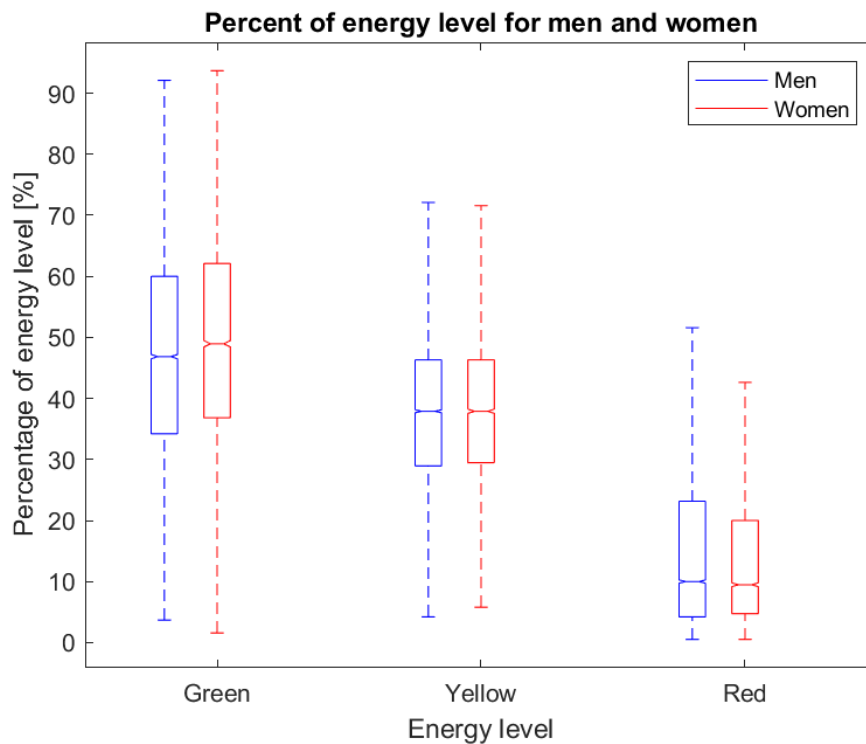
Figure 57: Box plot of the three energy level for 37 men and 19 women.

Table 20: Medians of the blocked aperture for both men and women for the different levels of blockage given in percent.

Gender/Medians of blockage	Green [%]	Yellow [%]	Red [%]
Men	46.84	37.89	10.00
Women	48.95	37.89	9.47

The p-values are summarized in table 21. This ranksum test test the alternative hypothesis that the median of the different levels of blockage for women are higher than for men. A p-value < 0.05 therefore means that women have significantly more blockage than men. It is evident from the table that women have significantly more green than men, and that men have significantly more red than women. There is not a significant difference in the yellow energy level.

Table 21: The resulting p-values for the different levels of blockage when comparing the values for men and women.

Level of blockage	p-value
Green	0
Yellow	0.6998
Red	1

The box plot in figure 58 shows the red blockage level when comparing the male and female patients for each image view. It is evident that there are large variations within each view. Women have significantly more red energy than men for the ALAX and the A4C view. This is possible to verify by the p-values given in table 22 as they are < 0.05. Men have significantly more red energy than women for the PLAX, the PSAX and the A2C view. This is also verified by the corresponding p-values.
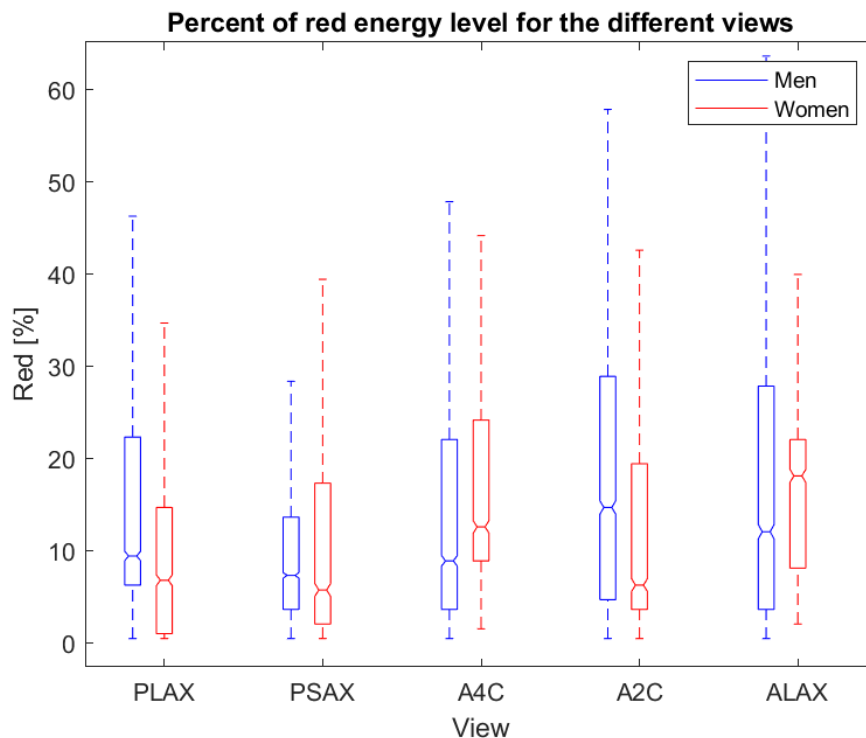
Figure 58: Box plot of the red energy level for 37 men and 19 women.

Table 22: The resulting p-values for the different image views when comparing the red energy level for men and women.

View	p-value
PLAX	1
PSAX	1
A4C	0
A2C	1
ALAX	0

4.5   Comparisons Between Different Heights and BMI

The article described in section 2.7 also stated that the height had a positive correlation with the widths of the intercostal spaces [3]. This section will therefore compare the GIC and the different energy levels for patients with different heights. The GIC and the different energy levels will also be compared for patients with different BMI. The data set used contained the recordings from the last 34 patients in the complete data set. This is 175 recordings from 26 men and 8 women.

4.5.1   GIC for Different Heights and BMI

The box plot in figure 59 shows the differences in the GIC for patients taller and shorter than 178 cm. The data set used is the one described in table 2, and the mean height were the height used in the box plot to distinguish between taller and shorter patients.
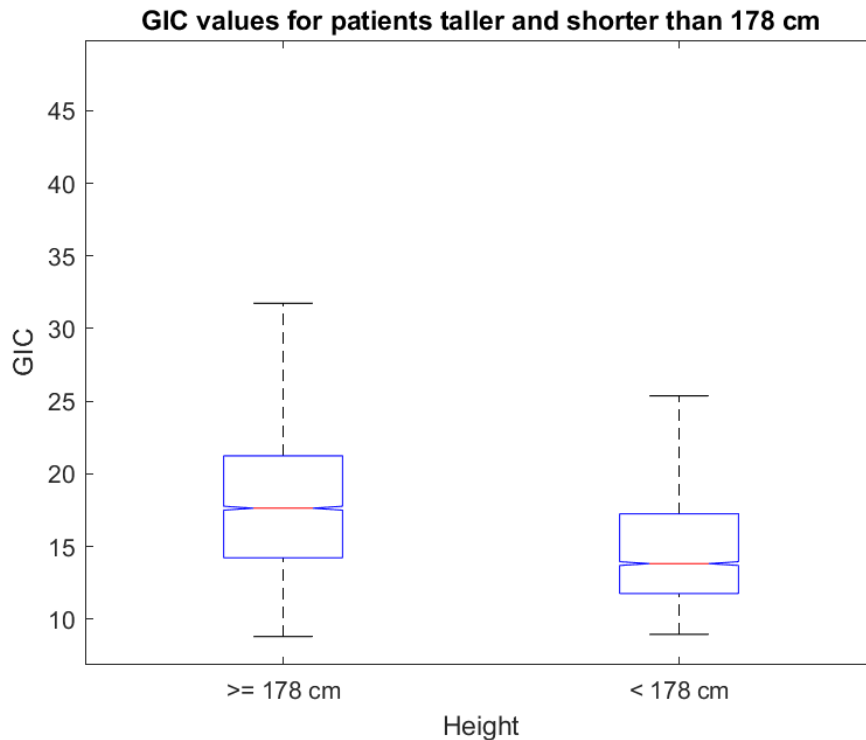
Figure 59: Box plot of the GIC values for patients taller and shorter than the mean height of 178 cm for the used data set.

The resulting p-value for this box plot was 0, which means that patients taller than 178 cm had significantly higher GIC than the patient shorter than this. This did not change when the height was lowered to 170 cm.

The gender distribution when distinguishing between different heights is shown in tab 23. The heights are defined as taller and shorter than both 178 cm and 170 cm. The total amount of patients was 34 with 26 men and 8 women.

Table 23: The gender distribution when distinguishing between different heights.

Gender/height	$\geq$ 178 cm	< 178 cm	$\geq$ 170 cm	< 170 cm
Men	20	6	26	0
Women	0	8	2	6

The box plot in figure 60 shows the differences in the GIC for patients with a BMI above and below 25. This BMI was chosen because this is the maximum BMI a person can have without

being classified as overweight.
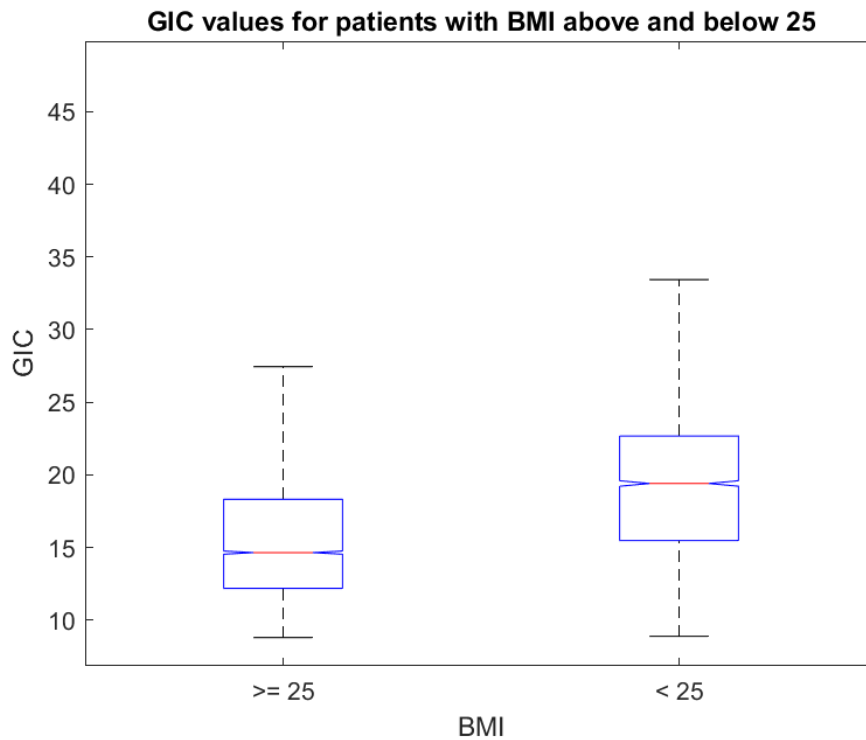
Figure 60: Box plot of the GIC values for patients with BMI above and below 25.

The resulting p-value for this box plot was 0, which means that the patients with a BMI below 25 had significantly higher GIC than the patients with a BMI above 25. This is also clearly visible in the box plot as the notches are not overlapping, and the fact that the box for a BMI below 25 had a higher maximum value. The gender distribution for this result is given in table 24. Only 2 out of 8 women had a BMI below 25, while 16 out of 26 men had a BMI above 25.

Table 24: The gender distribution when distinguishing between different BMI.

Gender/BMI	≥ 25	< 25
Men	16	10
Women	6	2

4.5.2   Different Levels of Blockage for Different Heights and BMI

The box plot in figure 61 and 62 shows the different energy levels for patients taller and shorter than 178 cm and 170 cm, respectively. It is possible to see a difference in both the green and the red energy level when comparing these plots. For the plot where the height was set to 178 cm there was not a visible difference in the green level. The red level, however, had a visible difference where patients taller than 178 cm had a larger median. The difference in the green level is more visible in the second plot where the height was set to 170 cm. The median of GIC for this level

for patients taller than 170 cm is now higher than in the previous box plot. There was also more difficult to see a clear difference in the red level, but it seems like the median for patients under 170 cm has increased.
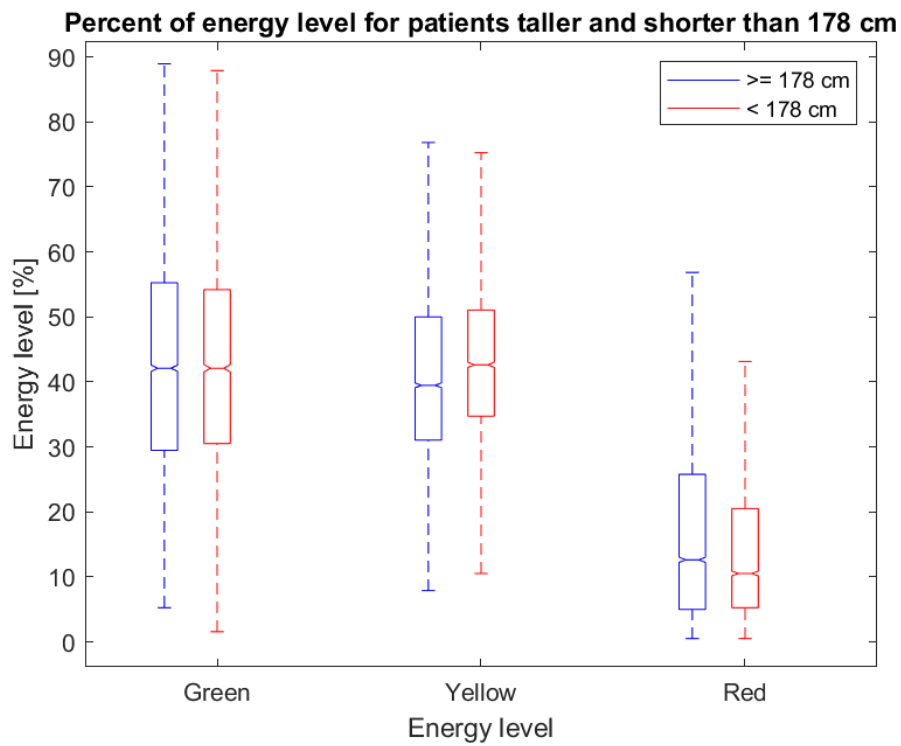
Figure 61: Box plot of the different energy levels for patients taller and shorter than 178 cm, which was the mean height for the data set used.
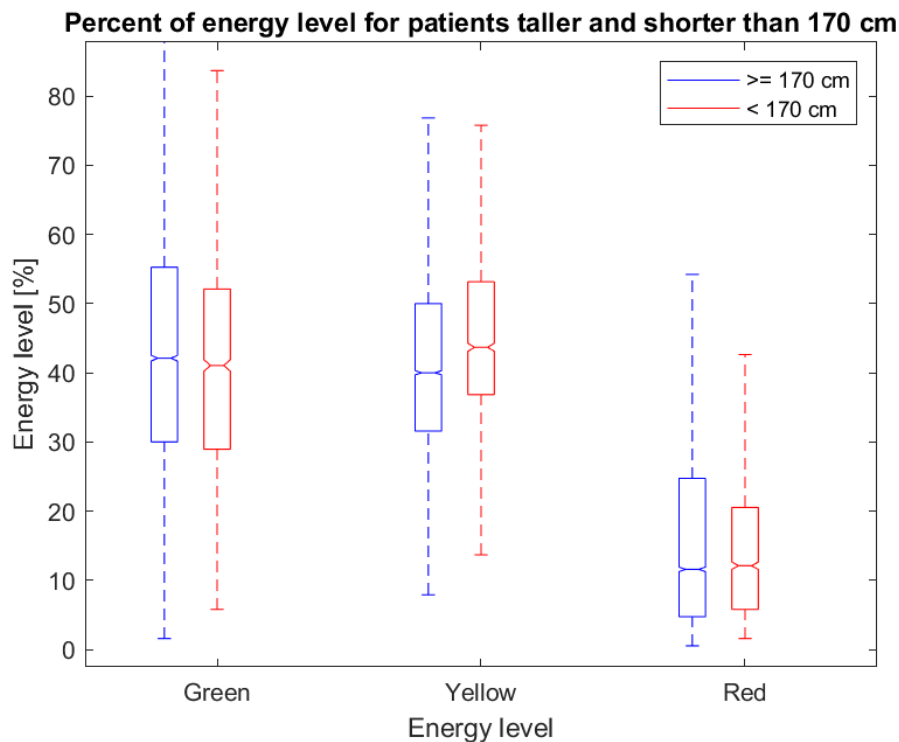
Figure 62: Box plot of the different energy levels for patients taller and shorter than 170 cm.

The resulting p-values for both of these box plots are listed in table 25. This shows that patients taller than 178 cm had significantly more red energy, while patients shorter than 178 cm had significantly more yellow energy. There is no significant difference for the green level, but the p-value is closer to 0.05 than 0.95. This p-value increased to 1 when the height was set to 170 cm, which means that patients taller than 170 cm had significantly more green. The p-value for the red level decreased to 0.9482, which is just below the limit that says that patients taller than 170 cm had a significant higher median.

Table 25: The resulting p-values for the different energy levels for patients taller and shorter than 178 cm and 170 cm.

Level of blockage/p-values	178 cm	170 cm
Green	0.2689	1
Yellow	0	0
Red	1	0.9482

The differences in the energy levels for patients with a BMI above and below 25 are shown in the box plot in figure 63. It is evident that there are large variations for the different energy levels, and that patients with a BMI above 25 have significantly more green and yellow than patients with a BMI below this value. These observations are verified by the p-values in table 26.
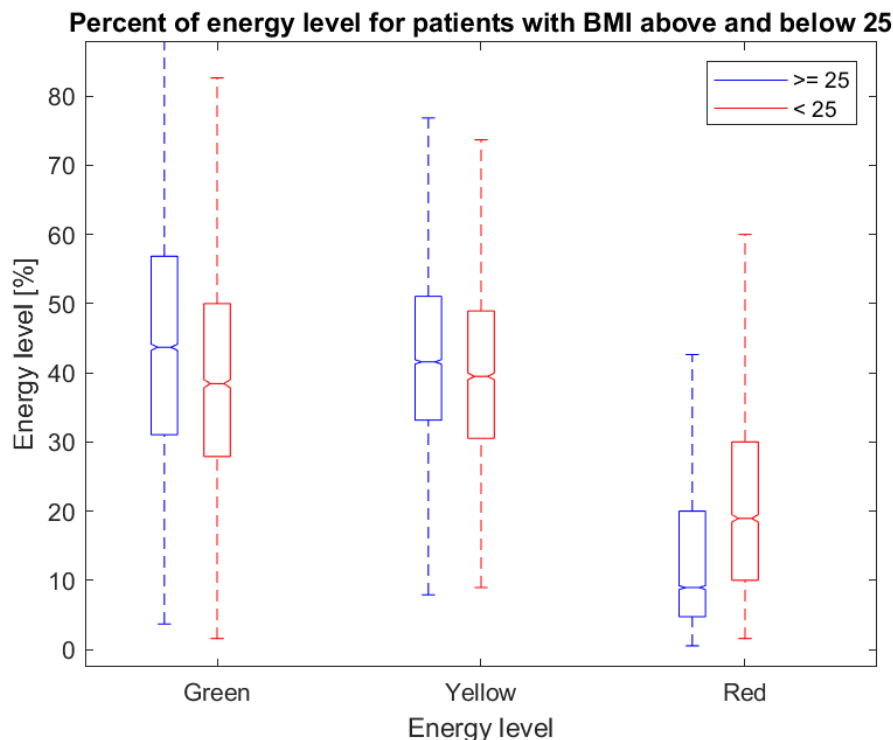
Figure 63: Box plot of the different energy levels for patients with BMI above and below 25.

Table 26: The resulting p-values for the different energy levels for patients with a BMI above and below 25.

Level of blockage	p-value
Green	1
Yellow	1
Red	0

4.6   Trends in the Processed Data

The purpose of this section is to highlight some visible trends for the image quality, the amount of blockage and the GIC values in the processed data. The data was divided into low and high GIC values, as well as small and large amounts of blockage, in order to reveal such trends. The data set used contained 22 patients with a total of 116 recordings.

As mentioned in section 4.3.1, there were significant differences in the medians of the GIC values for the parasternal and apical views, which means that the mean GIC value for a recording must be compared to the median of that view to conclude whether it is a high or low value. The videos with the minimum and the second minimum mean GIC values for each view were compared. This revealed that there was a high level of noise and clutter throughout the whole recording for a majority of the recordings. It was also generally a low amount of red energy, where the blockage was dominantly in the azimuth direction, as well as in both azimuth and elevation direction in the

corner of the traffic light plot. All the recordings also had static noise in the top of the image in the near field of the transducer. Figure 64 shows an example of an ultrasound image of the PSAX view which had a low mean GIC value (9.9).
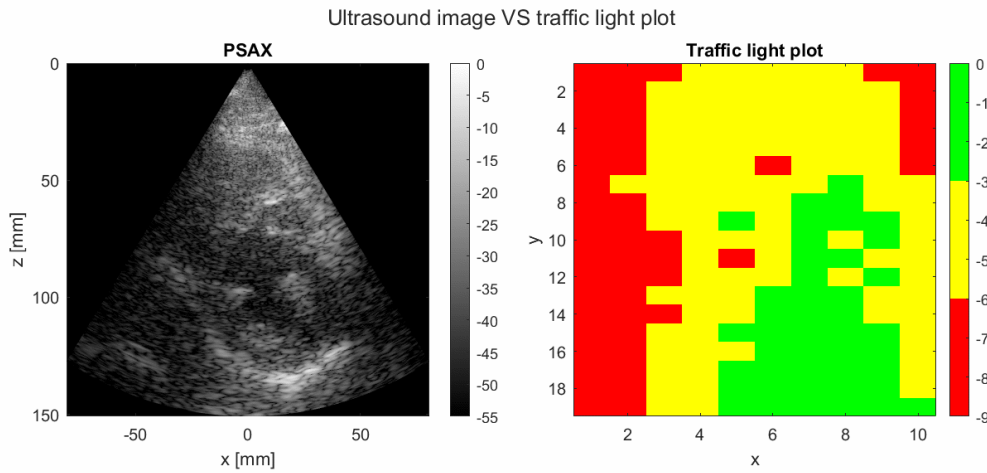
Figure 64: An example of an ultrasound image and the corresponding traffic light plot which had a low mean GIC value.

The recordings with the maximum and the second maximum mean GIC values were also compared. Figure 65 shows an example of an ultrasound image from the PLAX view which had a high mean GIC value (36.97). It is approximately the same levels of blockage for these recordings as for the ones with low GIC values, except that there seems to be a little less red energy. The blockage was also not as consistent in the azimuth direction as it was for those with low GIC values. There were also overall lower clutter and noise levels in these recordings, which had a positive effect on the image quality. Static noise in the near field were also visible for some of the recordings.
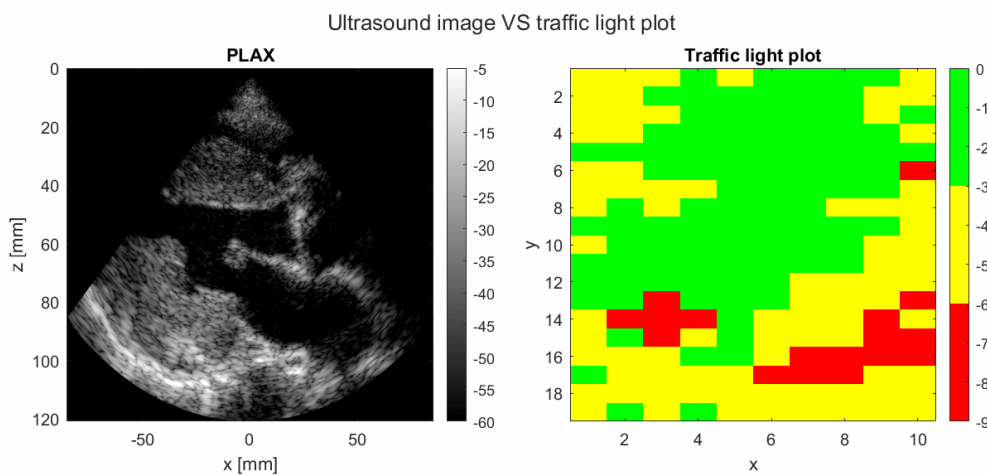
Figure 65: An example of an ultrasound image and the corresponding traffic light plot which had a high mean GIC value.

Large and small amounts of blockage were decided from the 75th percentile of the boxes in the box plot in figure 66. Values above the 75th percentile were considered as a low amount of blockage for the green level, and a medium and large amount of blockage for the yellow and red level,

respectively. A summary of these percentiles and the median values are given in table 27.
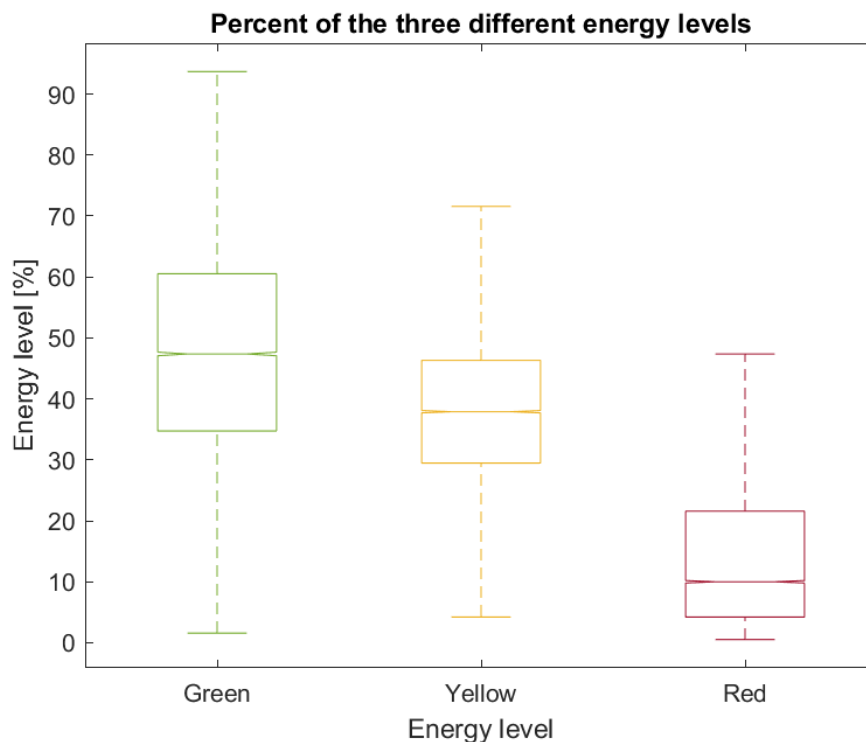
Figure 66: Box plot of the three levels of blockage for the processed data.

Table 27: Medians of the different blockage levels, as well as the 75th percentiles, given in percent.

Level of blockage	Median [%]	75th percentile [%]
Green	54.74	66.32
Yellow	33.16	41.10
Red	7.37	18.95

Approximately 79% of recordings with a red blockage level above 19% were of the apical views, while approximately half of the recordings had a GIC value under the median. All the recordings with the most extreme red blockage level (above 30%) were of the apical views. The overall image quality for these recordings varied a lot. There were recordings were the structures of the heart "drowned" in noise, and there were recordings which had a decent contrast and resolution. It was also possible to see a degradation of the lateral resolution in almost all the recordings with a red energy level above 30%. Figure 67 and 68 show two examples with a red energy level above 30% that have quite different image quality.

Figure 67: An example with a red energy level above 30%.

Figure 68: An example with a red energy level above 30%.
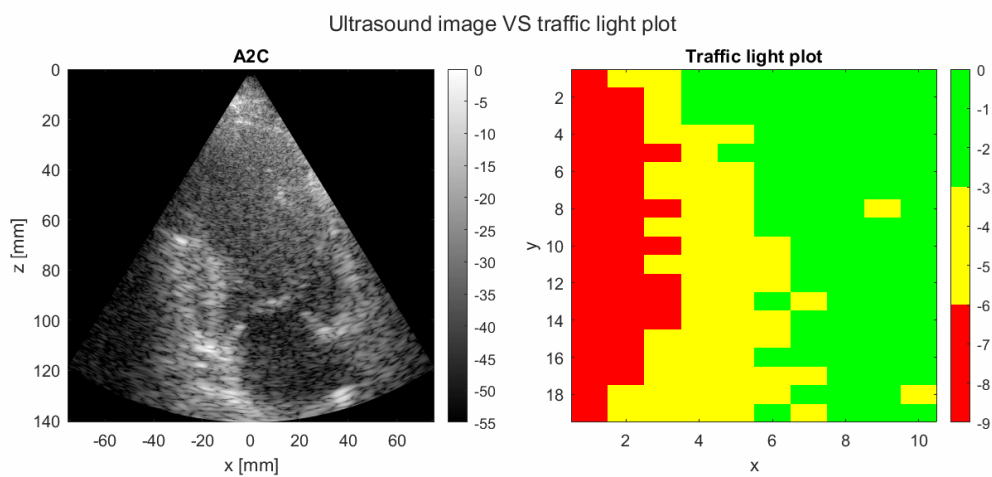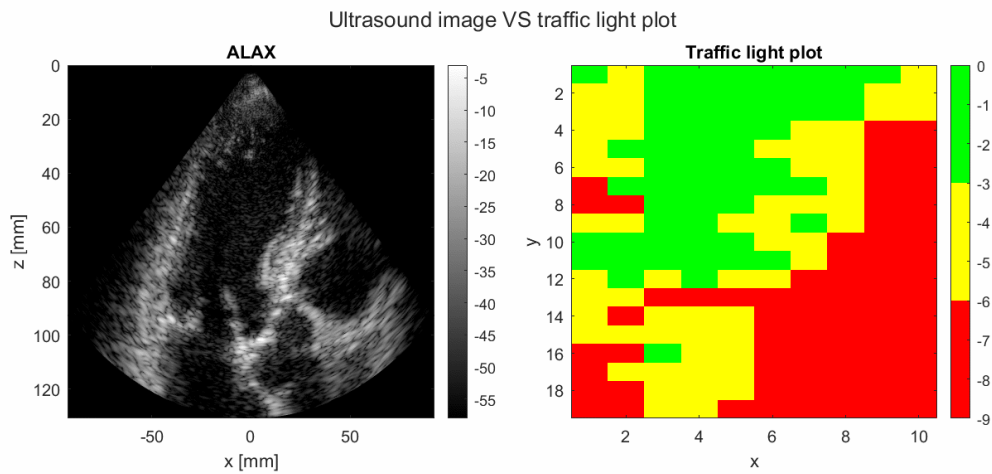
Approximately half of the recordings with a yellow energy level above 41% were of the parasternal views. The image quality varied a lot for these recordings, were the majority of the recordings had some kind of artifact that reduced the image quality. Figure 69 shows an ultrasound image of the video with the maximum amount of yellow energy, which was 52.79%.
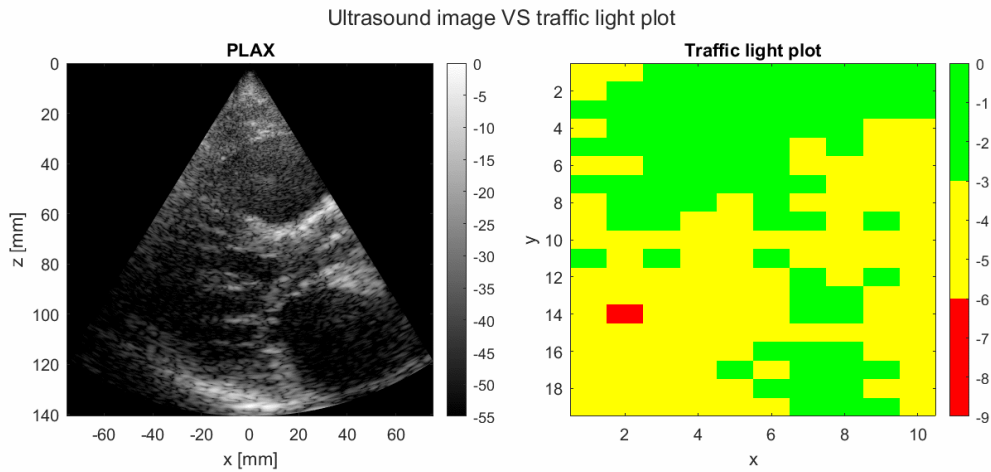
Figure 69: An ultrasound image and the corresponding traffic light plot of the recording with the maximum amount of yellow energy reduction level, which was 52.79%.

The recordings with over 67% of green level of energy reduction had a very small amount of red energy level, where half the videos had a GIC value above the median. Almost all of the recordings had a high level of noise throughout the whole image sector. The recording with the maximum amount of green (88.12%) had such a high level of noise that it was hard to properly see the heart. This is showed in figure 70. Figure 71 is of another example where the image quality is visibly better than in figure 70.
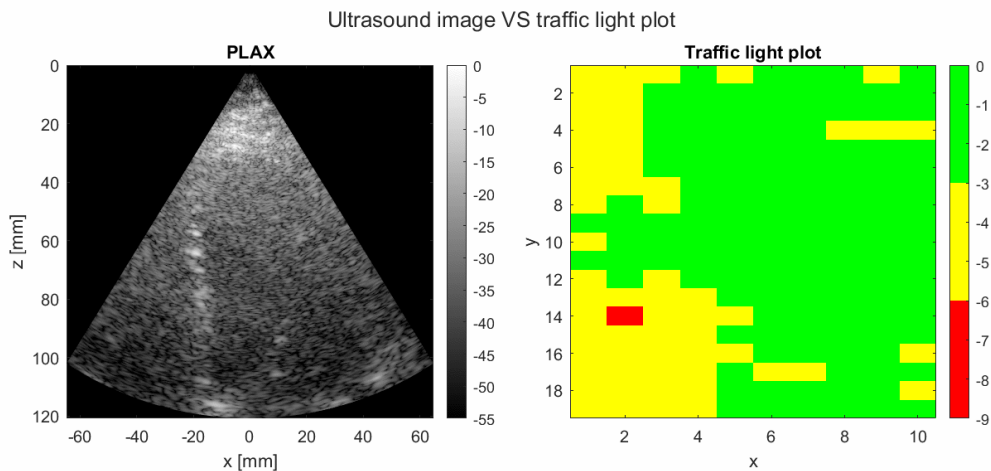
Figure 70: An ultrasound image and the corresponding traffic light plot of the recording with the maximum amount of the green energy level, which was 88.12%.
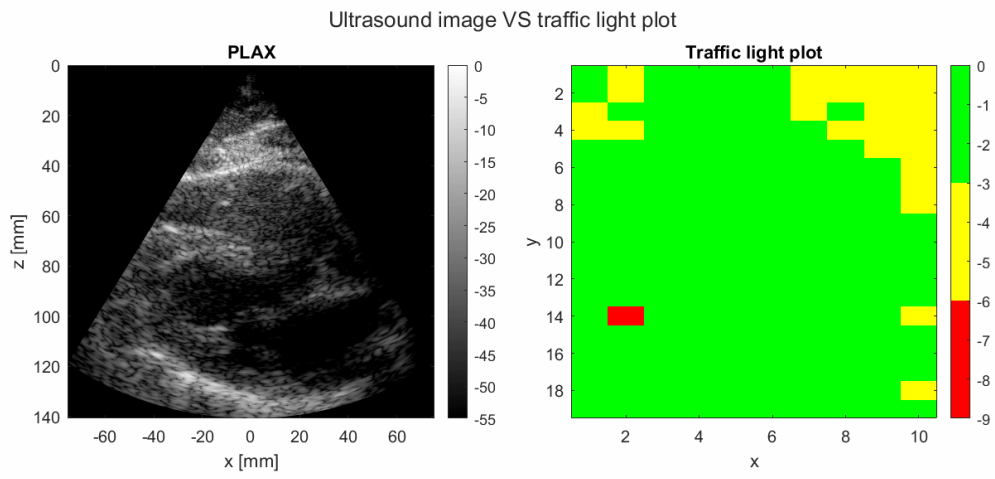
Figure 71: An example with a green energy level above 41%.

5   Discussion

In this chapter, the results presented in chapter 4 is discussed. The discussion is divided into eight sections to make the chapter more structured and easier to follow. The last section is intended to provide an overview over the main results discussed.

5.1   Important Comments

As described in the project preceding this master thesis, a weakness with the method for visualizing the aperture energy was discovered [1]. This weakness was described to produce false blockage concentrated in the middle of the energy plots, as shown in figure 72. From the figure it is evident that a large amount of the beams in the middle of the scanning sector are inside the ventricle at the start depth. The majority of the signal values for these beams, especially those who enters through the valve, are low. Since the sum of these values will result in a low energy value, it was concluded that this was the reason for why the special case of blockage occurred.
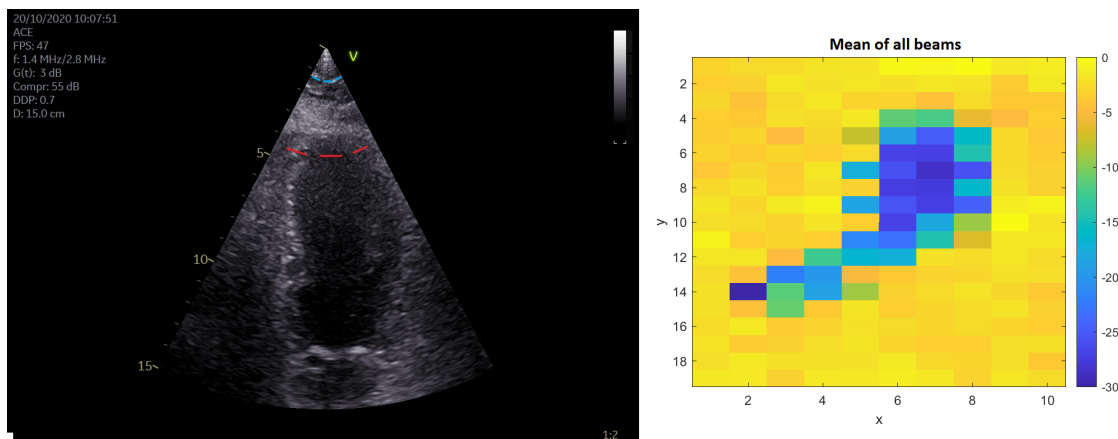
Figure 72: The ultrasound image and the corresponding amplitude plot of a special case where the energy is attenuated in a concentrated spot.

It was further explained that changing the start depth to a value lower than 30% could potentially fix the problem. This was, however, tested during this master thesis by dividing the depth region into smaller sections in order to see where this blockage first appeared. The results revealed that the blockage first occurred in the depth between 1.2-1.35 cm, which means that the start and end depth were set to 8% and 9%, respectively. In figure 72 it is clear that this region, depicted in light blue, is not the inside of the ventricle. Since the patient did not have any medical devices implemented near or inside the heart, for example a pacemaker, the blockage had to be explained by some kind of structure in the patients chest. This structure has to have a high reflectivity as the energy is attenuated throughout the whole depth region. What exactly this structure is, is currently not known.

Since it was revealed that the cause of the blockage was not due to a weakness with the method, the same method for visualizing the aperture energy described is therefore used in this master thesis. In addition to this, the same probe with the same error in one or more of the elements were used in this thesis. This means that there is attenuated energy in one specific spot in the energy plots for the examples shown. This attenuation will therefore not be taken into consideration when discussing the amplitude plots further.

5.2   A New Case of Rib Blockage

This section is of high importance as it proves that there is one more case of rib blockage that were not demonstrated in the article by Fatemi et. al. in 2019 [2]. The difference with this new type of rib blockage is that it is not assumed that all the ultrasonic energy is reflected back to the probe. The results from the simulations in section 4.2 also revealed the differences between rib blockage in different directions, and how this direction affects the image quality.

Figure 40 shows the results from the simulated blockage in the azimuth direction. It is obvious that the overall image quality is reduced when compared to figure 38, which shows the results when the transducer was not blocked. The signal strength on left side of the harmonic image, which was the side the plastic box was placed in front of the transducer, is clearly reduced. When the azimuth direction of the aperture is blocked, the active aperture is reduced, which will result in a reduction in the lateral resolution. This is also evident from the simulations as the structures look more "stretched" out in the lateral, or azimuth, direction in the whole image. In addition, some reverberations are visible in the left of the image. This is also typical for specular reflections at smooth surfaces like a rib.

Two examples of blockage in the azimuth direction are shown in figure 45 and 46. The traffic light plots show that there is an azimuth blockage to the left, which is quite significant as a large part of it is in the red energy level. The left side of the ultrasound image in figure 45 is clearly affected by this as the signal strength is lower than in the rest of the image. The recording also revealed that there was a very visible reduction of the lateral resolution, as well as reverberations in the area closest to the transducer. In figure 46 there is also a clear reduction of the lateral resolution. There was also static noise to the left in this example, which indicates that some of the signal that hits the ribs gets reverberated in the tissue outside of the heart before it reaches the transducer again. The mean GIC (11.92) for the first example was below the median of GIC (13.34) for the PSAX view, which can be seen as a reflection of the overall poor image quality. This was also the case for the second example as the mean GIC (14.85) was below the median (17.62) for the A2C view.

The results for blockage in the elevation direction is demonstrated in figure 42. The effects on the image quality are for this simulation a bit different from the simulation of rib blockage in the

azimuth direction. It is possible to see a signal loss in the whole harmonic image, and the focus of the transducer seems to be reduced. Like the blockage in figure 40 it is possible to see some reverberations at the top of the image sector, only for this case the reverberations are symmetric around the middle of the depicted structure. The explanation for this is that a blockage in the elevation direction will cause the ultrasound beam to be wider, which will lead to a poorer focus. This, in addition to the fact that the structure depicted is symmetric, is making it possible to see the curvature of the structure in the middle of the image sector.

Figure 47 and 48 are two examples of blockage in the elevation direction. The example in figure 47 was actually one of the traffic light plot which had the most red energy (66.34%) of all the processed recordings. It is possible to see the effects of the elevation blockage in the ultrasound image by for example the long reverberation artifact to the left. This reverberation was visible in all 64 frames, and it had side lobes, which is common when the focus of the transducer is not adequate. A degradation of the focus was a bit harder to see in this recording. The mean of GIC (13.55) was also quite a lot lower than the median of GIC (17.33) for the A4C view. The mean GIC (18.18) for the second example in figure 48 was a little bit above the median, and it is evident that there is a lot less noise in this example than in the previous one. The focus was also a bit poor here, and some reverberations in the middle of the recording. The overall quality for this example was better than the quality in the example in figure 47.

Figure 39 shows the simulation where the plastic box was placed in front of the transducer in both the azimuth and the elevation direction. The result was a combination of the typical effects for blockage in the azimuth direction and in the elevation direction. It is possible to see a reduction of both the lateral resolution and the signal strength in the harmonic image, as well as some of the curvature of the structure due to a poor focus. It does, however, seems like the degradation of image quality overall is not as significant as in for the simulation of the azimuth blockage in figure 40. The signal strength does, for example, seems to be stronger in figure 39 than in figure 40.

Two examples of blockage in both the directions are given in figure 43 and 44. The example in figure 43 was probably not the best example as the blockage in the traffic light plot is not as strict in the azimuth and elevation direction as it was in the two previous examples. The main reason for why this particular example was given was due to the fact that there was a very visible loss of signal strength in the shadow to the left in the ultrasound image. The recording revealed that the main blockage was located in the lower left corner, which can explain the occurrence of the shadow, and it was approximately constant for all 64 frames. It is evident that this shadow has major negative consequences for the image quality as parts of the heart structure are not possible to see. There was also multiple reverberation artifacts visible at the top of the image sector, which is, as stated above, typical for a rib blocking the aperture. A similar shadow is also evident in the next example in figure 44. The blockage is here located in the upper left corner, which is a more clear blockage in both directions than in figure 43. There were also a reduced lateral resolution

and focus, in addition to some reverberations at the top of the image sector. This example had a mean GIC (16.79) a bit below the median of the ALAX view (17.75). The previous example also had a mean GIC (12.55) slightly below the media of the PSAX view (13.34).

It is evident from the three different simulations of rib blockage that the traffic light plot was quite accurate. All the simulations had a significant signal reduction where the plastic box blocked the aperture. The effect one would expect from the different kinds of blockage in the traffic light plots was also visible in the ultrasound image. This argues that the traffic light plot is adequate to visualize different types of aperture blockage, as well as how severe the blockage is regarding signal loss. The method used to calculate the energy from the specific depth can therefore be said to be quite effective for detecting signal energy reduction due to blockage of the elements. The traffic light plots are, however, only visualizing the cases where the signal is not returning to the probe. As mentioned in 2.6, there are at least two other cases where the signal is interfering with the ribs, but ends up being reflected back to the probe again. These cases are therefore not as easy to identify from the visualization.

The simulations were done in a lab, which means that there were some inaccuracies from an ideal simulation of rib blockages. Firstly, the blockage was simulated by an angled plastic box instead of a real bone. Nevertheless, the box had a hard and smooth plastic surface, which does reflect signal quite efficiently. In addition, the box was thick and black, which reduced the possibility for the beams to be transmitted through it. The speed of sound were also not ideal as it was set to the speed of sound for air and not water. Since sound waves travel faster in water than in air, this could have caused some inaccuracies in the simulations. The effects the rib blockage had on the image quality was, however, successfully demonstrated, which means that the minor simulation errors were not as significant for the end result.

For all the results from the simulations it is possible to see a blockage in the right left corner. Since this blockage is visible in the simulations where none of the elements of the probe were blocked, it is evident that this is an error with the probe itself. It is possible that there are some "dead" elements in this area of the probe as the probe in general is very fragile due to the electronics inside it. This means that this area of blockage can be overlooked when discussing the results.

In summary, the findings discussed above have revealed that the new type of rib blockage demonstrated in this thesis is possible to simulate at a lab, as well as identify in echocardiograms from real patient data. A central consequence of this type of blockage is a reduced signal strength, as well as a reduced lateral resolution and degraded focus, depending on the direction of the blockage. It was also demonstrated that a blockage in only the azimuth direction degrades the image quality more than blockage in the elevation direction and in both directions. Furthermore, the traffic light plot was revealed to visualize the blockage quite accurate, which means that the method used to calculate the energy was effective for detecting a reduction in the signal strength. Lastly, it was demonstrated that three examples of quite poor image quality had a mean GIC value under the

median for that specific view.

5.3 Examples of the Different Cases

The results presented in section 4.1 are of interest because they provide examples of the five different cases described by Fatemi et. al. to generate clutter in cardiac images from real patients [2]. It shows that the cases described are indeed possible to recognize in different image views for different patients. These results also give the reader some indication of how the traffic light plot is connected to the ultrasound images, as well as how the GIC and the different energy levels are connected to the image quality.

The example of case (a) where the ultrasound energy is reflected outside the rib cage due to specular reflections are given in figure 32. Static clutter, which was typical for this case, was possible to identify to the left in the example. This was also visible at the top of the image sector. It was also, however, possible to see a reduction of the lateral resolution throughout the recording. The traffic light plot contained yellow, and some red, energy in the azimuth direction. Based on this, it can be argued that there is a rib blocking parts of the aperture. In addition, there is somewhat of a high level of clutter in the recording, which means that this example also can be an example of case (c). Lastly, the mean GIC value (13.35) was approximately the same as the median GIC value (13.34) for the PSAX view, which would indicate that the image quality is neither particularly good or bad. Since there is a lot of examples of the PSAX view with poorer image quality, it can be concluded that this make sense.

Figure 33 shows an example of case (b), which was the case where the energy is reflected inside the rib cage after hitting the ribs. The typical observations like static clutter and reverberations at the top of the image sector, as well as flickering clutter, were possible to recognize. In addition, there was also a high level of clutter throughout the ultrasound recording. This means, like explained above, that this recording can also be an example of case (c). It is also evident that the lateral resolution is not as reduced in figure 33 as it was in figure 32. This makes sense as there is a little less blockage, and the fact that the mean GIC (16.40) is above the median of GIC (15.33) for the PLAX view.

Figure 34 and 35 are better examples of case (c) than figure 32 and 33 because of the higher clutter level and the visible reverberations. There was also static clutter in the near field of the transducer, which is typical when the ultrasound energy gets reflected multiple times in soft tissue layers. The blockage is in both the azimuth and the elevation direction for both examples, where the traffic light plot is dominated by the green and the yellow energy level. The mean GIC (11.40) for the example in figure 34 was a lot lower than the median of GIC (17.33) for the A4C view. Because of this, one can argue that the main reason why there is a poor image quality in this case is because of the clutter and reverberations produced by the reflections in the soft tissue layers.

The mean GIC (18.40) for the example in figure 35 was quite a lot higher than the median (15.33) for the PLAX view. Both the resolution and the contrast are also better for this example than the previous one.

The example of case (d) was shown in figure 36. This was the case where the heart was partially covered by the lung in the azimuth direction. The air inside the lung will cause an almost complete reflection of energy, which makes it easier to identify this case in the data than the previous cases discussed. It is possible to see the lung to the left in figure 36, and in the recording this tissue moved in and out of the image sector with respiration. The mean GIC (19.20) was also higher than the median of GIC (17.62) for the A2C view. There was also little to no reduction of energy due to aperture blockage. It was also clear that there was noise throughout the whole recording. The two most likely causes of image quality degradation are therefore in this case the lung covering the heart in the azimuth direction and reflections in the soft tissue layers. Overall, the image quality was not as poor as in figure 34.

The last case described by Fatemi et. al. was the case where the heart was partially covered by the lung in the elevation direction. This was described to lead to the whole image being cluttered, as well as clutter that flickered with respiration. The easiest way to recognize this case was, however, by bands of noise in the ultrasound recording. This was the case for the example given in figure 37, where it is possible to see a band of noise in the top of the image. There were also some reverberations at the top of the image sector. The energy levels were comparable to the example given in figure 36, which means that the traffic light plot was dominated by mostly the green energy level. The overall quality was not the best compared to the previous examples, and the mean GIC (14.11) was also a little bit above the median of GIC (13.34) for the PSAX view.

In summary, the results in chapter 4.1 have proven that it is possible to identify the cases described by Fatemi et. al in the used data set. It has also showed that image quality in echocardiograms is complex, and that there are usually several explanations for why there is a degradation of the quality. All the examples given in this section did also have a small amount of signal reduction, which implies that the majority of the signal was reflected back to the transducer. The majority of the ultrasound videos processed during this thesis had artifacts that could be explained by a number of different scenarios. In addition to this, it was showed that recordings with a high mean GIC value seemed to have better image quality than those that had a low value. This strengthens the theory that the GIC can be used as a metric for cardiac image quality.

5.4   Differences Between Image Views

When studying the GIC metric and the different energy levels, it is relevant to examine whether there are some significant differences between the image views. The results presented in section 4.3 will therefore be discussed in this section, and the relevant image views are listed in table 3.

These results were box plots of both the GIC values and the three different energy levels.

The results for the GIC values for each frame for each of the 291 recordings are presented in the box plot in figure 49. It is obvious from the non-overlapping notches in the boxes that all the apical views have significantly higher medians than the parasternal views. When comparing the notches in the apical views it is clear that the medians are not significantly different from each other. The PSAX view is also significantly different from the PLAX view, where it is clear that the PLAX view has a higher median. These differences are also evident from table 15. The PLAX has the lowest maximum GIC (42.40), while the A2C view have the highest maximum (48.62).

A weakness with the GIC metric is that it is dependent on the amount of tissue in the image, which means that an image with a substantial amount of tissue would result in a higher GIC value. Since the apical views lies deeper in the body than the parasternal views, it would be logical to assume that the apical views have more tissue. It has therefore been a theory that this is the reason why there is a significant difference in the GIC between the two types of image views. This theory can, however, be disproved by the histograms in figure 50 and 51. The histogram for the apical views would have a larger amount of higher CF values if the apical views contained more tissue. It is evident from the histograms that they are quite similar, except for the parasternal views having a bit higher percent of the CF values in the larger bins 0.040-0.180. The bins 0.0009-0.004 are also higher for the apical views than for the parasternal views. Based on these observations, it can be stated that the explanation for why the apical views have significantly higher GIC than the parasternal views is not due to differences in the amount of tissue. One plausible explanation is the fact that the ultrasound waves in many cases must travel through the lungs in the parasternal views, which makes them more prone to interference with the lungs. This can possibly have a negative effect on the signal so that it is less coherent when it arrives at the transducer. As a result, the GIC value will also be lower. Since it has been argued that a lower GIC value corresponds to a poorer image quality, one can state that the apical views had better image quality than the parasternal views for the data set used in this thesis.

The first energy level that was introduced in a box plot were the green level, which is depicted in figure 52. It is obvious from both the notches in the boxes and the results in table 16 that the PLAX view has the lowest median of green for this data set. By comparing the notches for all the boxes, it is evident that the median for the PLAX view is significantly lower than all the rest except for the ALAX view. This could mean that the PLAX view has a larger signal energy reduction as a larger part of the traffic light plot must be either yellow or red. Furthermore, it is also possible to see that the PSAX view and the A2C view have the highest medians. Lastly, it is clear that all the boxes have a large distance between their 25th and 75th percentiles, which implies that there are large variations within the different views.

Figure 53 shows the resulting box plot for the yellow energy level. Even though there seems to be a little less difference between the views, it is possible to identify some significant differences.

The A2C view has significantly smaller amounts of yellow than the rest of the views. The results in table 16 also show that the A2C view has the lowest median, while the PLAX view has the highest. The PLAX view also have significantly higher medians than the rest of the views. The distance between the 25th and 75th percentiles for all the views are also quite large, which implies that there is variation around the median. It is hard to say anything concrete about a high or low level of yellow as the traffic light plot consists of a combination of the three levels, as well as the fact that this level still contains signal with over half of the signal energy left. This means that large amounts of yellow do not automatically mean that there also is a high level of the red energy.

The box plot for the red energy level is given in figure 54. An interesting observation is that all the apical views have a significant higher median that the parasternal views, as well as a larger distance between their 25th and 75th percentiles. It is evident that the PSAX view has the lowest median of the red energy level. As stated in the article from the American Society of Echocardiography, the apical views are not always available in every patient due to transmission limitations caused by the intercostal spaces [44]. This implies that an aperture blockage where there is a considerable signal loss occurs more often for the apical views, most likely due to specular reflections at the ribs. It is also possible to see these differences in table 16, where the medians for the apical views are the highest. It is also clear that all the boxes are skewed except for the ALAX view. The boxes for the PLAX view and the A2C view seem to be the most skewed.

In the PLAX view the probe is placed on the patients chest so that the azimuth direction of the transducer is parallel to the ribs, which means that it is logical that this view has a low amount of signal energy reduction due to blockage. When moving from the PLAX view to the PSAX view, the probe must be rotated clockwise 90 degrees, as explained in section 2.6. This means that the azimuth direction of the transducer is no longer parallel to the ribs, but instead is crossing the ribs. It is therefore logical to assume that the PSAX view would have a larger percent of red than the PLAX view. This is, however, not the case as the PLAX view have significantly higher median of the red level. An explanation for this is the fact that the traffic light plot is only detecting the loss of signal energy, and not the interactions with the ribs where the signal is reflected to the transducer. For both case (a) and (b) it is possible that the signal is reflected at the ribs and that the overall path back to the transducer again is longer. The electronics in the transducer will not interpret this as a signal loss even though the ribs have interfered with the signal. It is therefore possible that the aperture in the PSAX view actually is more blocked than it seems. This is reflected in the GIC values in the box plot in figure 49 where the PLAX view has significantly larger GIC than the PSAX view.

Overall, the results in this section revealed that there are differences in both the level of energy reduction due to blockage and the GIC values for the different image views. One of the most important findings was that the apical views have significantly higher median of GIC than the apical views, most likely due to the fact that the parasternal views are more prone to interference

with the lungs. This implies that the apical views have better image quality than the parasternal views. In addition, the apical views had the overall largest amount of red signal energy reduction, where the ALAX view had a significant larger median of red than all the other views. The PSAX and the PLAX view had the lowest amount of red, but the highest amount of yellow. The PLAX view also had the lowest median of the green energy level of all the views.

5.5   Comparisons Between Men and Women

This section is of high importance as it discusses the results presented in section 4.4 where the data set was separated based on gender. These results are directly related to the hypothesis stating that women have poorer cardiac image quality than men due to the probe size. The main results were the GIC values and the different energy levels, as well as the resulting p-values from the Wilcoxon rank sum tests.

The box plot in figure 55 shows the difference in the GIC values for the male and female patients examined. The conducted right-tailed Wilcoxon rank sum test resulted in a p-value of 0, which means that the median of GIC for men was significantly higher than for women. Since it was previously argued that a higher GIC corresponds to better image quality for this data set, it can be stated that it is more likely that men have better image quality than women. These results therefore support the hypothesis described in this master thesis. In relation to this, it is worth mentioning that there were approximately the same number of recordings of the parasternal and the apical views for both the male and the female patients. This means that the significant difference is not because of a predominance of the apical views in the male data set, as the apical views had significantly larger GIC values than the parasternal views.

The GIC values when distinguishing between both gender and image views are given in the box plot in figure 56. This reveals that there are variations in the GIC values for especially the apical views. It is also evident that the majority of the notches in the boxes for men and women are not overlapping, which means that there are significant differences between the image view for the genders. The median of GIC are clearly significantly higher for women for the PSAX and the A2C view. Men have significantly higher median than women for the PLAX and the ALAX view. The ALAX view has the biggest difference in the medians for men and women of all the views. For the A4C view, it is not so obvious whether there is a significant difference or not as the box for women are much longer. All of these observations are confirmed by the p-values from the Wilcoxon rank sum tests in table 18. These results mean that for a majority of the views, men have higher GIC values than women. It is therefore possible to argue that men have better image quality than women for the PLAX and the ALAX view, while women have better image quality for the PSAX and the A2C view. It is not possible to say that there is a significant difference in the A4C view other than that the p-value is a lot closer to 0.05 than to 0.95. With a larger data set it would might have been possible to obtain a significant difference where men had a higher median of GIC

for this view.

The next part of section 4.4 contained the results of the different energy levels when distinguishing between the male and the female patients. The fact that there is not a clear distance between the notches in the boxes in figure 57 indicates that there are smaller differences in the energy levels than in the GIC values. It is also possible to see that the boxes for both the genders for the red energy level are skewed, where the majority of the percentage values are above the median. The Wilcoxon rank sum tests conducted results in a p-value < 0.05 if women have significantly more of that energy level than men, which means that a p-value close to 1 indicates that men have significantly more of that energy level than women. The resulting p-values in table 20 revealed that women have significantly more of the green energy level than men, while men have significantly more red energy than women. There was not a significant difference in the yellow energy level. Since the traffic light plot is constructed in a way that visualize blockage by the amount of signal energy reduction, it is clear from the results in chapter 4.4 that men have overall more critical blockage of the aperture than women. This blockage did not seem to affect the image quality as much as men had significantly higher GIC.

The box plot in figure 58 shows the red energy level for men and women for the different image views. This was presented in order to get a better overview of the red level as this is the energy level that was defined as the most critical blockage of the aperture. It is clear from both the box plot and the p-values in table 22 that there are significant differences between the genders for all the views. Women have significantly more red energy for the A4C and the ALAX view, while men have significantly more red energy for the PLAX, the PSAX and the A2C view. It is possible to state that there are large variations within the views, especially for the A2C and the ALAX for men. This can be explained by the fact that everyone has a different body, but also the fact that the data set used might be too small. An interesting point of view is to compare the red energy for the ALAX view to the GIC box plot in figure 56. It is obvious that for this view women had significantly lower GIC values and larger percent of red energy, while it was the opposite for the men. The same observations can be seen for the PSAX and the A2C. This can either be a coincidence, or it shows a trend where a large aperture blockage is connected to a low GIC value.

Since the same cardiac probe was used for all the patients, the only thing that was different for each patient was their own body. This would mean that the amount of signal energy reduction is an indirect measure of the patients intercostal spaces. A theory was that patients with narrower intercostal spaces, more specifically women, would have a larger amount of signal loss due to blockage by the ribs. As argued above, men had more critical aperture blockage than women, which contradicts this theory. It is unlikely that the reason for this is that the probe is too big for men's intercostal spaces as they are significantly wider than for women. An explanation for this can be the same as stated in the previous section. The traffic light plot is only detecting the loss of signal energy, and not the interactions with the ribs where the signal is reflected to the transducer.

This means that it is possible that women have more interference with the ribs than men, but not more signal loss due to aperture blockage. In addition, the article that introduced the differences in the intercostal spaces did measure 466 patients, which is a lot more than the 56 patients used in this thesis. The used data set also had a predominance of male patients. There was also little to no difference in the energy levels and GIC values between the frames for each patient. Generally, a larger data set will lead to increased precision in statistics, meaning that a more correct analysis could be obtained. It is therefore relevant to test the hypothesis introduced in this thesis on a data set containing a lot more patients, as well as approximately the same number of male and female patients.

As a result, one can say that the statistics presented in section 4.4 both contradicted and supported the hypothesis that said that women have poorer image quality than men because of the probe size. It was revealed that men had significantly higher GIC than women, which implies that the cardiac image quality is better for men for the data set used in this thesis. Men did, however, have more critical blockage, or in this case red energy, than women. This implies that the probe is not too large for women's intercostal spaces. The method used in this thesis is only detecting the aperture blockage that causes a signal loss, and not when the signal is only interfering with the ribs. This means that it is possible that the ultrasound beams for women are interfering more with the ribs than what is presented. This is supported by the fact that men had significantly higher GIC than women. It would also be of interest to have a larger data set to get more conclusive results as the data set used only contained 56 patients.

5.6   Comparisons Between Different Heights and BMI

This section will discuss the results presented in section 4.5 where the GIC and the different energy levels for patients with different heights and BMI were compared. These comparisons were relevant because of the article in section 2.7 that stated that height had a positive correlation with the widths of the intercostal spaces, which meant that these are wider for taller people than for shorter people [3]. Different BMI's were also compared since the data set used to produce these results contained additional information about the patients' physique. Two different heights were chosen as a limit between tall and short patients, and a BMI of 25 was used to distinguish between high and low BMI values.

Figure 59 shows the box plot of the GIC values when distinguishing between patients taller and shorter than 178 cm, which was the mean height of the data set used. The notches in the two boxes are clearly not overlapping, which means that patients taller than 178 cm have significantly higher GIC than those shorter than 178 cm. This result did not change when the height was lowered to 170 cm, which is the reason why this box plot was not shown. It can therefore be stated that the taller patients in the data set had better image quality than the shorter patients. The article that measured intercostal spaces in section 2.7 stated that taller people had wider intercostal spaces.

Based on this, one can argue that the reason why the taller patients in the data set had significantly higher GIC, and therefore also better image quality, was because of their intercostal spaces were wide enough so that the ribs did not interfere as much with the beams.

The box plot in figure 61 and 62 shows the differences in the three energy levels for patients taller and shorter than 178 cm and 170 cm. For both plots, patients shorter than 178 cm and 170 cm had significantly more yellow energy than those who were taller. Patients taller than 170 cm had significantly more green, while there was no significant difference when the height was set to 178 cm. It is also evident in both plots that the taller patients had significantly more red energy than the shorter patients. Since taller people have wider intercostal spaces, one would assume that the shorter patients would have more of the red energy level. The differences are, however, quite small, so it is possible that this is only the case for the data set used. It is also possible that if the energy levels were defined differently that the results would change. In addition, the traffic light plots only detect one type of aperture blockage, as previously mentioned.

The box plot in figure 60 shows the resulting GIC values when distinguishing between patients with a BMI above and below 25. It is here obvious that patients with a BMI below 25 have significantly higher GIC than those with a BMI above 25. The maximum GIC is also quite a lot higher for those with a BMI below 25. Patients with a BMI between approximately 18.5-25 are in general considered to have a normal weight, while those who have a BMI above this is considered to be overweight. Since overweight people often have a higher body fat percentage, it is logical to assume that the ultrasonic beams have to travel further to reach the heart for these patients. This can result in a weaker signal, as well as more unwanted reflections in the soft tissue layers on the chest. This means that the results in figure 60 makes sense as it indicates that patients with a higher BMI, or a BMI that is classified as overweight, have poorer image quality than those with a lower or more normal BMI. It can therefore be stated that the GIC metric supported the hypothesis that it is more difficult to obtain an adequate image quality for patients with a higher BMI.

Figure 63 shows the box plot for the three energy levels for patients with a BMI above and below 25. Patients with a BMI above 25 have significantly more green and yellow energy, while patients with a BMI below this have significantly more red energy. These observations are confirmed by the p-values in table 26. This would indicate that having a higher BMI corresponds to a higher signal energy at the transducer. However, it is obvious from all the box plots in section 4.5 that there are large variations in the data set. The data set used contained only 8 women and 26 men because these were the only patients where the additional information about the height and the BMI was given. This is obviously too little data to produce precise and reliable statistics. The gender distribution is also skewed as there were over three times as many men as women in the data set. It is therefore not possible to fully trust the results given in this section, but rather use them as an indicator.

It is evident in the gender distribution in table 23 that the only patients that were taller than 178 cm were men, and that none of the male patients were shorter than 170 cm. This is not as surprising as there were only 8 women out of the 34 patients in the data set. It would have been more logical to have an even distribution of men and women for the different heights as it can give a conclusion independent of the gender. It is also a weakness that only 6 patients were shorter than 170 cm. This means that the red boxes in the box plot in figure 62 only consist of 6 women, which is too little to make the statistics reliable. Based on this, one can state that there is a need for a larger data set to say anything more conclusive.

In summary, the results in 4.5 revealed that taller patients and patients with a lower or normal BMI had significant higher GIC. This was expected as taller people have wider intercostal spaces, which makes the ribs less likely to interfere with the ultrasound beams. People with a higher BMI, or a higher body fat percentage, are also more prone to for example reflections in the fat and skin layer on the chest. This means that the GIC metric was high when it was expected to be high, and vice versa. It was, however, also revealed that the data set used was too small to say anything more conclusive. The GIC should therefore be tested on a lot more patients where both the height and the BMI are available.

5.7   Trends in the Processed Data

When studying the connection between the image quality, the level of blockage and the GIC metric, it is relevant to discuss visible trends in the processed data set. This section will therefore discuss the results presented in section 4.6 where the recordings were divided into low and high GIC, as well as small and large amounts of blockage. It is important to know that the data set only contained 22 patients, which means that the trends discovered are typical for the analyzed recordings in this thesis, and not necessarily typical for other data sets.

When the recordings with the minimum and second minimum mean GIC value for each view were looked at, it was obvious that the overall image quality was poor. A majority of the recordings had a high level of noise and clutter for all the frames, as well as a large amount of static noise in the top of the image sector. It was also evident that there was not a substantial amount of red energy for these recordings. The majority of them had a high percentage of the green energy level, in addition to some degree of yellow. The blockage that was visible was dominantly in the azimuth direction and in both directions. As a result, one can argue that if a recording has a low mean GIC value, it is likely that the overall image quality is not adequate enough to properly diagnose the patient. It is also evident that a small amount of the red energy level does not necessarily mean that the image quality is good enough to provide diagnostic value.

The recordings with the maximum and second maximum mean GIC value for each view were also scrutinized. It was clear that the image quality for these recordings were much higher than for

those with a low mean GIC value. It was a lot easier to see the heart structures, and the contrast was better. There was also a lower level of noise in the recordings, even though some of them still had some degree of static clutter at the top of the image sector. The recordings with the overall best quality were those with a GIC value well above the median for that specific view. There was also an even distribution between the apical and the parasternal views for these recordings. The amount of red and yellow blockage was approximately the same as for the recordings with a low GIC value, which would imply that a high GIC value is closer connected to a good image quality than a low amount of blockage is.

As explained in section 4.6, the recordings were also separated based on the percentage of the different energy levels. Values above the 75th percentile in table 27 were considered as a low amount of blockage for the green level, and a medium and large amount of blockage for the yellow and red level. A closer look at the recordings with a red energy level above 30% revealed that a common factor for this amount of red was a reduced lateral resolution, which is typical for a reduced active aperture. All of these recordings were also of the apical views, which would imply that the apical views are more prone to aperture blockage than the parasternal views. The image quality varied a lot, where the different types of artifacts related to the different directions the blockage was in, as described in section 5.2, were possible to identify. Shadows due to a reduced signal strength, reverberations and a poor focus were examples that were easily identified in these video. The recordings with the poorest image quality were also those with a mean GIC value below the median for the specific view. An example is the difference between figure 67 and 68. It is clear that the image quality is better for figure 67, which had a mean GIC value (17.58) just a little below the median for the ALAX view (17.75). For figure 68 the mean GIC value (13.25) was much lower than the median for the A2C view (17.62), which is almost identical to the median for the ALAX view. This strengthens the argument that a lower GIC value would correspond to a lower image quality as well. In addition, the blockage was in the azimuth direction for the example with the poorest image quality, while it was in both directions for the other example which had a better image quality.

Approximately half of the recordings with more than 41% yellow energy were of the parasternal views, which means that a large amount of yellow is not more typical for either the apical or the parasternal views. It was harder for these recordings than for the recordings with a large amount of red energy to point out any typical factors that degraded the image quality. The image quality varied a lot, and it was possible to identify several of the different cases explained in section 2.6 while analyzing these recordings. Some of the recordings had a decent image quality in regards to both contrast and resolution, while others either had artifacts or a very high level of noise which degraded the quality and reduced the diagnostic value.

It was interesting to look at the recordings with a green energy level above 67%. These recordings had overall a very small signal energy reduction as both the yellow and green energy levels were

low. Only half of these recordings had a mean GIC value above the median, even though they were the ones with the highest percentage of the green energy level. In addition, almost all the recordings had a high level of noise for all the frames. The video with the largest percentage of green (88.12%), which is depicted in figure 70, had such a high level of noise that it was challenging to see any of the structures of the heart. Since there was also a large amount of static noised at the top of the image sector, as well as some reverberations, the explanation can be that the patient has a lot of soft tissue in the area where the probe was placed. This type of degradation of image quality, more specifically explained in case (c) in section 2.6, is typical when the ultrasonic energy is reflected in layers of skin, fat and muscle. This explanation can also be applied to many of the other recordings with a green percentage value above 67%. There were, however, also some recordings with a decent image quality, where all of them had a mean GIC quite a lot above the median. It can therefore based on this be stated that a GIC value well above the median of GIC is an indicator of a decent image quality.

The power spectrum in figure 18 shows the harmonic filter that was applied to the channel data. An important observation in this spectrum is that the filter is placed a little too far to the right, which means that some of the second harmonic frequencies are filtered out, as well as some of the unwanted fundamental frequencies are left in the signal. This filtering may also have worked different for the different recordings, where for some it might have been ideal and for others not. This reveals a weakness with the harmonic filtering that can have consequences for the interpretation of the image quality in the analyzed ultrasound recordings. It is therefore possible that the fundamental signal left in the filtered data was misinterpreted as noise in the recordings. In addition, the image quality on a proper ultrasound scanner is far better than it is when using the USTB in MATLAB. This means that it is possible that some of the processed recordings with a poor image quality might have a decent image quality if they were visualized on a scanner instead.

The overall results obtained by analyzing the processed recordings, such as described in section 4.6, have revealed a number of important things. First of all, it has demonstrated that the image quality is closer connected to the mean GIC than the amount of energy loss due to aperture blockage. This is based on multiple examples with a low image quality where there was a high percentage of the green energy level, and vice versa. In addition to this, it was possible to imply that a mean GIC well above or below the median of GIC for the specific views gives a good indication whether the image quality is adequate or not. This means that a mean GIC value at the median, or with just a small deviation from the median, does not give as accurate indication of the image quality as a larger deviation does. Furthermore, it has been revealed that all the recordings with a red energy level above 30% were of the apical views, which means that the apical views have a higher level of signal energy reduction than the parasternal views in the used data set. Lastly, a larger amount of yellow blockage (above 41%) was revealed to not have any typical artifacts as the image quality varied extensively for the recordings analyzed.

5.8   Overview of the Results

The main hypothesis in this paper was that the cardiac probes used today are too large for women's intercostal spaces, which leads to a poorer image quality for women. The results in section 4.4 revealed that here is not a simple and conclusive answer to the hypothesis. The male patients in the data set used had significantly higher GIC than the female patients, which indicates that men have better cardiac image quality as the returning signal is more coherent. It was also revealed that men had significantly more of the red energy level, while women had significantly more of the green level. This means that even though men had a better image quality, they also had more aperture blockage. The method used to indicate whether the aperture is blocked or not is based on detecting signal loss, and is therefore not detecting the cases where the signal is interfering with the ribs and returned to the aperture. It is therefore possible that the reason why women had significantly lower GIC than men is because of other cases of interference with the ribs, like case (a) and (b) in section 2.6. In addition to this, it is likely that the data set is a bit too small. The article in section 2.7 measured the intercostal spaces for 466 patients, while the data set used in this thesis only contained the recordings from 56 patients. A logical assumption is therefore that it is possible to obtain a more precise and conclusive answer to the hypothesis if the data set is larger.

The article in section 2.7 did also state that taller people had wider intercostal spaces than shorter people. The results in section 4.5 revealed that the taller patients had a higher median of GIC, where the difference between the patients shorter and taller than 170 cm were significant. The theory that people with a higher BMI (> 25) had poorer image quality due to for example a higher body fat percentage was also confirmed by the GIC metric. It was, however, also revealed that patients taller than 170 cm and patient with a BMI lower than 25 had significantly more red energy. The explanation for this can be the same as previously mentioned about the traffic light plot only detecting blockage in form of signal loss at the aperture. Another explanation can be the choice of energy levels. It would have been interesting to see if for example the red energy level could be defined in a more precise way. Patient shorter than 178 cm did have significantly more of the yellow energy than the taller patients, which means that it it possible that the red energy level was set to a too deep attenuation. It is also possible that the patients with this much red energy might be special cases, and therefore not representative for that specific height. As argued above, a larger data set could give more conclusive answers to this.

A new type of rib blockage that were not introduced by Fatemi et. al. in 2019 was also demonstrated in this thesis [2]. The results revealed that a blockage in the azimuth direction was characterized by a signal loss and a reduced lateral resolution, while a degraded focus and a uniform signal loss was more typical for a blockage in the elevation direction. A blockage in both directions revealed to be a combination of these effects. A blockage strictly in the azimuth direction seemed to be the most critical for the image quality, and it was also the easiest type of blockage to demon-

strate during the simulations because of how the visible the effects were. The examples given in section 4.2 also proved that this type of blockage is possible to identify in echocardiograms of real patients.

The results from the simulations in section 4.2 also demonstrated how the traffic light plot worked. The blockage in the three different simulations was located exactly where the plastic box was placed, which indicates that the traffic light plot is quite accurate in detecting signal loss. It was also demonstrated that the traffic light plot can detect different types of blockage in different directions. This argues that the method used to calculate the energy from a specific depth can be used to visualize aperture blockage where the signal is not returning to the probe. The traffic light plot does, however, not reveal whether the ribs are interfering with the ultrasound beams if the signal is reflected back to the probe. As a result, the traffic light plot can be used as a tool for the cardiologist to visualize the aperture blockage when there is a signal loss, as well as the direction and how severe it is.

The results in this thesis also revealed that the cardiac image quality was closer connected to the GIC metric than the aperture blockage caused by the ribs. Ultrasound videos that had a GIC well below the median for that specific view had in general a quite poor image quality, while it was the opposite for videos with a GIC well above the median. A plausible explanation for this, that was also demonstrated in this thesis, is that the image quality in echocardiograms is complex. This means that for a majority of the cases there are several reasons for why the image quality is degraded. Examples of videos where there was a substantial amount of blockage, but an adequate image quality, were demonstrated. In relation to this, the recording with the most green energy had a visibly degraded image quality, which means that something other than a signal loss due to a rib must have caused this degradation. Overall, this thesis demonstrated that the mean GIC for a cardiac ultrasound video can be used as a measure for the image quality.

Comparisons of both the GIC and the different energy levels between the image views revealed substantial variations. The apical views had significantly higher GIC than the parasternal views, which was revealed to not be due to a difference in the amount of tissue. One plausible explanation for this is the fact that the lungs more easily interfere with the ultrasonic signal for the parasternal views than for the apical views. This strengthen the argument that the GIC metric is higher for the apical views because the image quality is better. The apical views had, however, significantly more red energy than the parasternal views, and the parasternal views had higher medians of green than the apical views. The ALAX view had the most amount of red, which were significantly higher than all the other views. This shows that a larger amount of blockage does not necessarily means that the image quality is poorer.

6   Conclusion

This thesis has analyzed three different energy levels to conclude whether the cardiac probes used today are too large for women's intercostal spaces due to aperture blockage by the ribs. A new objective metric called the Global Image Coherence (GIC) has also been demonstrated as a measure for in-vivo image quality. In order to see if women have poorer image quality than men, this new metric has been compared to both the image quality and the amount of aperture blockage. The data set used contained a total of 291 recordings of five different image views from 37 men and 19 women. Amplitude plots of the different levels of energy were constructed to both visualize and compare the aperture blockage.

The results revealed that the ultrasound recordings with a visually adequate image quality generally had high GIC values. The amount of blockage, however, was not necessarily small for these recordings. This means that the GIC is closer connected to the image quality than the amount of aperture blockage, which concludes that the GIC metric can be used as a measure for in-vivo image quality. The traffic light plots constructed did successfully detect the new type of aperture blockage demonstrated, but it did not detect cases where the signal is interfering with the ribs before being reflected to the probe. In addition, the apical views had the overall largest amount of red energy, but also significantly higher GIC values than the parasternal views. This was not due to a difference in the amount of tissue in the views, but most likely because of the parasternal views being more prone to interference with the lungs.

It was also revealed that people with wider intercostal spaces, like men and taller people, have significantly higher GIC, and therefore also better image quality. The patients with a BMI under 25 did also have significantly higher GIC. The results did, however, also demonstrate that both the male patients and the taller patients ($\geq$ 178 cm) had significantly more of the red energy level, which was defined as a greater signal energy attenuation than -6 dB. As previously mentioned, the method for calculating and visualizing blockage was based on detecting signal energy at the probe, which means that it is possible that both women and shorter people have more interference with the ribs than what the results demonstrated. This theory is supported by the significantly lower GIC values.

The fact that the image quality was better for men and taller people, which have wider intercostal spaces, indicates that the cardiac probes are too large for women. The results also argue the need to conduct a larger study with a method that properly detects both the aperture blockage that causes signal loss, as well as the cases where the ribs are only interfering with the ultrasound signal.

6.1   Future Work

The amplitude plots constructed turned out to be a useful tool to visualise the aperture blockage that causes signal loss. It was possible to examine both the amount and location of the blockage from these plots. It would, however, be relevant to test different energy levels to see how the results change, as the energy levels chosen in this thesis might not be the best choice. In addition, it would be helpful for the cardiologist to be able to not only see the signal loss in the amplitude plots, but also the cases where the ribs are only interfering with the signal.

The results also indicated that the data set used to demonstrate differences in the GIC values and the energy levels was too small. There was also not an even distribution between men and women in this data set. The data set used to see differences in the GIC value for different heights and BMI's was especially small. It would here have been interesting to conduct this study with for example tall women and short men to see if the taller patients still have significantly higher GIC values. In addition, it would have been relevant to test the different values of the BMI that classify whether a person is underweight, normal or overweight. This would have provided more precise and correct statistics.

Bibliography

[1] N. Edvardsdal. 'Comparisons of Aperture Blockage Caused by the Ribs for Male and Female Patients in Echocardiography'. Project report in TFE4580. NTNU, Faculty of Information Technology and Electrical Engineering, 2021.

[2] A. Fatemi, E. A. R. Berg and A. Rodriguez-Morales. 'Studying the Origin of Reverberation Clutter in Echocardiography: In Vitro Experiments and In Vivo Demonstrations'. In: *Ultrasound in Medicine and Biology* Vol. 45 (2019), pp. 1799–1813.

[3] Y. Kim, M. J. Park, H. Rhim, M. W. Lee and H. K. Lim. 'Sonographic Analysis of the Intercostal Spaces for the Application of High-Intensity Focused Ultrasound Therapy to the Liver'. In: *American Journal of Roentgenology* Vol. 203 (2014).

[4] World Health Organization. *Cardiovascular diseases.* 2021.

[5] L. Sletten. 'Coherence Based Imaging in Echocardiography Using a 2D Matrix Array Probe'. NTNU, Department of Circulation and Medical Imaging, 2020.

[6] Mayo Clinic. *Echocardiogram.* https://www.mayoclinic.org/tests-procedures/echocardiogram/about/pac-20393856. Online: Accessed 2021-10-15.

[7] Martin Christian Hemmsen et al. 'Ultrasound image quality assessment: a framework for evaluation of clinical image quality'. In: *Medical Imaging 2010: Ultrasonic Imaging, Tomography, and Therapy.* Ed. by Jan D'hooge and Stephen A. McAleavey. Vol. 7629. International Society for Optics and Photonics. SPIE, 2010, pp. 105–116. DOI: 10.1117/12.840664.

[8] O. H Rindal, T. G. Bjåstad, T. Espeland, E. R. Berg and S. Måsøy. 'Very Large Matrix Array Cardiac Channel Database (VLCD) used to Evaluate Coherence as an In-Vivo Image Quality Metric'. In: *IEE Transactions on Ultrasonics, Ferroelectrics, and Frequency Control* Vol. 1.No. 1 (2022), pp. 1–1.

[9] N. Bottenus W. Long and G. Trahey. 'Lag-One Coherence as a Metric for Ultrasonic Image Quality'. In: *IEE Transactions on Ultrasonics, Ferroelectrics, and Frequency Control* Vol. 65.No. 10 (2018), pp. 1768–1780.

[10] R. Mallart and M. Fink. 'Adaptive focusing in scattering media through sound-speed inhomogeneities: The van Cittert Zernike approach and focusing criterion'. In: *The Journal of the Acoustical Society of America* Vol. 96.No. 6 (1994), p. 3721.

[11] Pai-Chi Li and Meng-Lin Li. 'Adaptive Imaging Using the Generalized Coherence Factor'. In: *IEE Transactions on Ultrasonics, Ferroelectrics, and Frequency Control* Vol. 50.No. 2 (2003), pp. 128–141.

[12] M. Parrilla J. Camacho and C. Fritsch. 'Phase Coherence Imaging'. In: *IEE Transactions on Ultrasonics, Ferroelectrics, and Frequency Control* Vol. 56.No. 5 (2009), pp. 958–974.

[13]   L. M, Hinkelman, T. D. Mast and L. A. Metlay, et al. 'The Effect of Abdominal Wall
       Morphology on Ultrasonic Pulse Distortion. Part I. Measurements'. In: *The Journal of the
       Acoustical Society of America* Vol. 104.No. 6 (1998), pp. 3635–3549.

[14]   L. M, Hinkelman, T. L. Szabo and R. C. Waag. 'Measurements of Ultrasonic Pulse Distortion
       Produced by Human Chest Walls'. In: *The Journal of the Acoustical Society of America* Vol.
       101.No. 4 (1998), pp. 2365–2373.

[15]   The Economist. *How Medicine Discriminates Against Non-white People and Women.* 2021.

[16]   K. Moore, A. Ganesan, C. Labrosciano, W. Heddle, et al. 'Sex Differences in Acute Com-
       plications of Cardiac Implantable Electronic Devices: Implications for Patient Safety'. In:
       Journal of the American Heart Association Vol. 8.No. 2 (2019).

[17]   M. Inacio, C. Ake, E. Paxton, et al. 'Sex and Risk of Hip Implant Failure'. In: *Journal of the
       American Heart Association* Vol. 173.No. 6 (2013), pp. 435–441.

[18]   S. Geller, A. Koch, P. Roesch, A. Filut, et al. 'The More Things Change, the More They Stay
       the Same: A Study to Evaluate Compliance With Inclusion and Assessment of Women and
       Minorities in Randomized Controlled Trials'. In: *The Journal of the Association of American
       Medical Colleges* Vol. 93.No. 4 (2018), pp. 630–635.

[19]   L. Løvstakken. 'Signal processing in diagnostic ultrasound: Algorithms for real-time estima-
       tion and visualization of blood flow velocity'. NTNU, Department of Circulation and Medical
       Imaging, 2007.

[20]   Daquan Xu. *Physics of Ultrasound.* https://www.nysora.com/foundations-of-regional-
       anesthesia/equipment/physics-of-ultrasound/. Online: Accessed 2021-10-10.

[21]   D. L. Hykes W. R. Hedrick and D. E. Starchman. *Ultrasound Physics and Instrumentation.*
       4th ed. Mosby, 2004.

[22]   Johan Henrik Ræder (SINTEF). *Piezoelectric materials for sensors, actuators and ultrasound
       transducers.* https://www.sintef.no/en/expertise/sintef-industry/materials-and-nanotechnolog
       y/piezoelectric-materials-for-sensors-actuators-and-ultrasound-transducers/. Online: Accessed
       2021-09-03.

[23]   Thoracic Key. *Physical Principles of Ultrasound and Generation of Images.* https://thora
       cickey.com/physical-principles-of-ultrasound-and-generation-of-images/. Online: Accessed
       2021-09-03.

[24]   S. Mehdizadeh. 'Adaptive beamformers for ultrasound imaging of acoustically hard tissues'.
       NTNU, Department of Circulation and Medical Imaging, 2012.

[25]   V. Eder F. Tranquart N. Grenier and L. Pourcelot. 'Clinical Use of Ultrasound Tissue Har-
       monic Imaging'. In: *Ultrasound in Medicine and Biology* Vol. 25.No. 6 (1999), pp. 889–894.

[26]   F. Forsberg A. Anvari and A. E. Samir. *A Primer on the Physical Principles of Tissue
       Harmonic Imaging.* 2015.

[27]   M. Toulemonde. *New beamforming strategy for improved ultrasound imaging: application to biological tissues nonlinear imaging*. 2014.

[28]   J. Kim M. Lee and S. Park. 'Analysis of a Scan Conversion Algorithm for a RealTime Sector Scanner'. In: *IEE Transactions on Medical Imaging* Vol. 5.No. 2 (1986), pp. 96–104.

[29]   A. Ng and J. Swanevelder. 'Resolution in Ultrasound Imaging'. In: *The British Journal of Anaesthesia* Vol. 11.No. 5 (2011), pp. 186–192.

[30]   J. E. Aldrich. 'Basic physics of ultrasound imaging'. In: *The Society of Critical Care Medicine and Lippincott Williams and Wilkins* Vol. 35.No. 5 (2007), pp. 131–137.

[31]   S-E. Måsøy. 'Estimation and correction of aberration in medical ultrasound imaging'. NTNU, Department of Engineering Cybernetics, 2004.

[32]   A. Støylen. *Basic Ultrasound of Clinicians*. 2016.

[33]   Michael Baad, Zheng Feng Lu, Ingrid Resier and David Paushter. 'Clinical Significance of US Artifacts'. In: *Department of Radiology* Vol. 37 (2017), pp. 5–10.

[34]   Hideki Yoshikawa Jun Yasuda and Hiroki Tanaka. 'Phase aberration correction for focused ultrasound transmission by refraction compensation'. In: *Japanese Journal of Applied Physics* Vol. 58.No. SG (2019), SGGE22.

[35]   D-L. Liu L. M. Hinkelman and et al. R. C. Waag. 'Measurement and correction of ultrasonic pulse distortion produced by the human breast'. In: *The Journal of the Acoustical Society of America* Vol. 97.No. 3 (1998), pp. 1958–1969.

[36]   L. M. Hinkelman T. D. Mast and et al. L. A. Metlay. 'Simulation of ultrasonic pulse propagation, distortion, and attenuation in the human chest wall'. In: *The Journal of the Acoustical Society of America* Vol. 106.No. 6 (1999), pp. 3665–3677.

[37]   A. A. Arifi A. A. Mohamed and A. Omran. 'The basics of echocardiography'. In: *Journal of the Saudi Heart Association* Vol. 22 (2010), pp. 71–76.

[38]   Wikipedia. *Echocardiography*. https://en.wikipedia.org/wiki/Echocardiography. Online: Accessed 2021-12-14.

[39]   National Cancer Institute. *Structure of the Heart*. https://training.seer.cancer.gov/anatomy/cardiovascular/heart/structure.html. Online: Accessed 2021-11-03.

[40]   Cleveland Clinic. *Heart Valves*. https://my.clevelandclinic.org/health/articles/17067-heart-valves. Online: Accessed 2021-11-03.

[41]   Phoenix Heart Center. *Echocardiograms: Transthoracic (TTE) and Transesophageal (TEE)*. http://www.phoenixheartcenter.com/echocardiograms-tte-tee/. Online: Accessed 2022-02-25.

[42]   Wikipedia. *Transthoracic echocardiogram*. https://en.wikipedia.org/wiki/Transthoracic_echocardiogram. Online: Accessed 2021-10-29.

[43]   Brian Gill. *The GE 4Vc-D: An Advanced Cardiac Probe*. 2019.

[44] C. Mitchell, P. S. Rahko, L. A. Blauwet, B. Canaday, J. A. Finstuen, M. C. Foster, K. Horton, K. O. Ogunyankin, R. A. Palma and E. J. Velazquez. 'Guidelines for Performing a Comprehensive Transthoracic Echocardiographic Examination in Adults: Recommendations from the American Society of Echocardiography'. In: *American Society of Echocardiography: Guidelines and Standards* Vol. 32.No. 1 (2019), pp. 4–26.

[45] M. Roser, C. Appel and H. Ritchie. *Human Height.* https://ourworldindata.org/human-height. Online: Accessed 2022-02-25.

[46] Maria Abdli. *Nederlandske menn og latviske kvinner er høyest (2016).* https://www.vg.no/nyheter/utenriks/i/XykbE/nederlandske-menn-og-latviske-kvinner-er-hoeyest. Online: Accessed 2022-03-08.

[47] C. Simpson. 'Objective Image Quality Metrics for Ultrasound Imaging'. NTNU, Department of Electronics and Telecommunications, 2009.

[48] NTNU Medicine and Health - Blog. *Enhancing marine sonar and medical ultrasound imagery using wave coherence.* https://blog.medisin.ntnu.no/en/enhancing-marine-sonar-and-medical-ultrasound-imagery-using-wave-coherence/. Online: Accessed 2022-02-04.

[49] S. Måsøy A. Fatemi and A. Rodriguez-Molares. 'Row-Column-Based Coherence Imaging Using a 2-D Array Transducer: A Row-Based Implementation'. In: *IEE Transactions on Ultrasonics, Ferroelectrics, and Frequency Control* Vol. 67.No. 11 (2020), pp. 2303–2311.

[50] G. Pinton J. Dahl M. Jakovljevic and G. Trahey. 'Harmonic Spatial Coherence Imaging: An Ultrasonic Imaging Method Based on Backscatter Coherence'. In: *IEE Transactions on Ultrasonics, Ferroelectrics, and Frequency Control* Vol. 59.No. 4 (2012), pp. 648–659.

[51] The USTB Abstract. *The UltraSound ToolBox.* https://www.ustb.no/ius2017-abstract/. Online: Accessed 2022-01-28.

[52] Alfonso Rodriguez-Molares et al. 'The UltraSound ToolBox'. In: *2017 IEEE International Ultrasonics Symposium (IUS).* 2017, pp. 1–4. DOI: 10.1109/ULTSYM.2017.8092389.

[53] MathWorks. *boxplot.* https://se.mathworks.com/help/stats/boxplot.html. Online: Accessed 2021-10-20.

[54] MathWorks. *ranksum.* https://se.mathworks.com/help/stats/ranksum.html. Online: Accessed 2021-10-20.